

ulm university universität

uulm

Institut für Festkörperphysik

Tuning the magnetic properties of thin films by interaction with periodic nanostructures

Dissertation

Zur Erlangung des Dr. rer. nat.
der Fakultät für Naturwissenschaften der Universität Ulm

vorgelegt von
Felix Häring
aus Rottweil am Neckar

Dezember 2013

Amtierender Dekan:
Prof. Dr. Joachim Ankerhold

1. Gutachter:
Prof. Dr. Paul Ziemann

2. Gutachter:
Prof. Dr. Ulrich Herr

Tag der Promotion:
27.03.2014

Abstract

This work presents a study of the magnetic properties of nanoscaled, hexagonally ordered antidot arrays within magnetically soft thin films. The antidot arrays are prepared by colloidal lithography. The approach allows tuning of the lattice constant a (here: $100\,\mathrm{nm} \leq a \leq 500\,\mathrm{nm}$) and antidot diameter d in the range $0.1a - 0.95a$. Magnetic characterization is achieved by integral methods such as SQUID magnetometry and magnetotransport measurements as well as microscopic magnetometry methods such as magnetic force microscopy (MFM) and X-ray microscopy. All experimental methods are supported by micromagnetic computer simulations.

The presence of the antidots generally leads to a magnetic hardening effect with enhancements of the coercive fields by typically two orders of magnitude. The coercive field can be tuned by the antidot array geometry in a wide parameter range and shows a strong dependence on the saturation magnetization and exchange constant.

Periodicity of the antidot lattice reflects in the remanent magnetization, as revealed by MFM. Dependent on the ratio between antidot diameter and lattice constant (d/a-ratio), two distinct domain patterns can be identified. The pattern arising in antidot arrays with large d/a-ratio results from a minimization of the stray field energy and resembles the charge ordered state in geometrically frustrated artificial spin-ice. This analogy is further studied. The domain pattern for small d/a-ratios reduces the energy of its domain walls.

For both cases, a strong in-plane anisotropy of the magnetization reversal with respect to the antidot lattice arises. Application of integral magnetometry methods is not suitable to resolve this anisotropy, as the self-assembly approach of the sample preparation lacks long range order. This is overcome by measuring the anisotropic magnetoresistance through constrictions processed by focused ion beam milling, allowing for a well-defined orientation between magnetic field an antidot lattice. For samples with small d/a-ratio, this novel method identifies the nearest neighbor direction of the lattice as the easy axis, while a large d/a ratio is linked to an easy axis in the next nearest neighbor direction.

The respective reversal mechanisms are further studied by in-field MFM and corresponding simulations. For small d/a-ratios, the easy axis reversal is driven by nucleation of reversed mesoscopic domains, which are strongly pinned at the antidot sites. The hard axis reversal is characterized by a rotation of the magnetization over intermediate easy axis. For large d/a-ratios, narrow elongated bridges emerge in between neighboring antidots, which show a Ising-spin like behavior during the whole reversal process. The magnetic charge configuration at the vertices obey the ice-rules of honeycomb spin-ice.

Kurzfassung

In dieser Arbeit werden die magnetischen Eigenschaften von nanoskaligen, hexagonal geordneten Lochgittern in weichmagnetischen Dünnschichten untersucht. Die Probenpräparation wird mittels kolloidaler Lithographie realisiert. Der Prozess ermöglicht ein Einstellen der Gitterkonstanten a (hier: $100\,\mathrm{nm}$ - $500\,\mathrm{nm}$) und des Lochdurchmessers im Bereich $0.1a - 0.95a$. Zur magnetischen Charakterisierung kommen integrale Methoden wie SQUID-Magnetometrie und Magnetwiderstands-Messungen sowie ortsaufgelöste Magnetometrietechniken wie Magnetkraftmikroskopie (MFM) und Röntgenmikroskopie zum Einsatz. Alle experimentellen Methoden werden durch mikromagnetische Computersimulationen ergänzt.

Die Lochgitter stabilisieren die Magnetisierung der Filme. Das Koerzitivfeld erhöht sich um typischerweise zwei Größenordnungen. Sein Wert lässt sich innerhalb weiter Grenzen über die Geometrie des Lochgitters einstellen und hängt zudem stark von der Sättigungsmagnetisierung sowie der Austauschkonstanten ab.

Magnetkraftmikroskop-Aufnahmen zeigen, dass sich die Periodizität des Lochgitters in der Domänenkonfiguration widerspiegelt. Abhängig vom Verhältnis zwischen der Lochgitterkonstanten und des -durchmessers (d/a-Verhältnis) können zwei verschiedene Domänenmuster identifiziert werden. Das aus einem großen d/a-Verhältnis resultierende Muster minimiert in erster Linie die Streufeldenergie und zeigt viele Parallelen zum geordneten Ladungszustand in geometrisch frustrierten künstlichen Spin-Eis Strukturen. Diese Analogie wird anschließend weiter untersucht. Im Gegensatz dazu ist die Domänenanordnung bei einem kleinen d/a-Verhältnis günstiger im Hinblick auf die in den Domänenwänden gespeicherte Energie.

In beiden Fällen entsteht eine starke Anisotropie des Ummagnetisierungsprozesses bezüglich des Lochgitters. Diese kann mittels integraler Magnetometrie nicht aufgelöst werden, da die Nahordnung des Lochgitters durch den Selbstorganisationsprozess auf Kristallite von typischerweise $25 \times 25\,\mu\mathrm{m}^2$ beschränkt ist. Dieses Problem wird mittels einer neuen Methode gelöst, die auf der Messung des anisotropen Magnetwiderstands an mittels fokussiertem Ionenstrahl selektierten Kristalliten des Lochgitters basiert. Auf diese Weise entsteht eine lokale Sonde für die Magnetisierung mit einer definierten Orientierung zwischen Magnetfeld und Lochgitter. So können leichte und harte Achsen der Magnetisierung innerhalb der Filmebene unterschieden werden.

Die Mechanismen, die dem jeweiligen Ummagnetisierungsvorgang zu Grunde liegen, werden mikroskopisch untersucht. Im Falle eines kleinen d/a-Verhältnis findet die Ummagnetisierung entlang der leichten Richtung über die Nukleation von Domänen statt, deren Wandbewegung von den Löchern stark behindert wird, während für die schwere Richtung eine Drehung der Magnetisierung über dazwischenliegende leichte Richtungen beobachtet wird. Im Falle eines großen d/a-Verhältnis entstehen enge, lange Brücken zwischen benachbarten Löchern, die ein Ising-Spin-artiges Verhalten während des gesamten Ummagnetisierungsvorgangs zeigen. Die Konfiguration der magnetischen Ladung an den Kreuzungspunkten dieser Gitter folgt den Spin-Eis-Regeln für Kagomé Spin-Eis.

Für meine Eltern.

Contents

1 Fundamentals **5**

1.1 Ferromagnetism 5

1.1.1 Exchange Interaction 5

1.1.2 Magnetocrystalline Anisotropy 6

1.1.3 Shape Anisotropy 7

1.1.4 Zeeman Energy 8

1.1.5 Domains & Domain Walls 9

1.2 Magnetoresistive Effects 10

1.2.1 Anisotropic Magnetoresistance (AMR) 11

1.2.2 Positive Magnetoresistance 12

1.2.3 Negative Magnetoresistance 12

1.3 Artificial Spin-Ice Systems 13

1.3.1 Geometric Frustration 13

1.3.2 Spin-Ice 14

1.3.3 Artificial Spin-Ice 17

2 Preparation and structural characterization of Antidot Arrays **21**

2.1 Preparation Process 21

2.1.1 Deposition of the Polystyrene (PS) Nanospheres 23

2.1.2 Plasma Etching of the PS Spheres 25

2.1.3 Thin Film Deposition 27

2.1.4 Removal of the magnetic caps & PS spheres 27

2.2 Effect of surfactant on template formation 28

2.3 Determination of geometrical and structural parameters of the antidot arrays 30

3 Methods for Magnetic Characterization **35**

3.1 SQUID Magnetometry 35

3.2 Magnetotransport Measurements 36

3.2.1 Setup for Magnetotransport Measurement 36

3.2.2 Interpretation of AMR measurements 37

3.3 Magnetic Force Microscopy 39

3.3.1 Non-Contact Force Microscopy 39
3.3.2 Formation of Magnetic Contrast 42
3.3.3 Experimental Setup 44
3.4 X-ray Magnetic Circular Dichroism (XMCD) based microscopy techniques . 44
3.4.1 Scanning Transmission X-Ray Microscopy (STXM) 45
3.4.2 X-ray Photo Emission Electron Microscopy (X-PEEM) 46
3.5 Finite Element Micromagnetic Simulations 47

4 Magnetic Characterization of Self-Assembled Antidot Arrays 53
4.1 Integral Magnetic Properties 54
4.1.1 Interplay between magnetic material and antidot geometry 55
4.1.2 Influence of lattice parameter 62
4.1.3 Out-of-plane magnetization reversal 63
4.1.4 Temperature dependent hysteresis behavior 64
4.1.5 Summary 66
4.2 Intrinsic domain structures of hexagonal antidot arrays 68
4.2.1 Domain pattern for small d/a ratio 69
4.2.2 Domain pattern for large d/a ratio 70
4.3 Anisotropic Magnetoresistance in Antidot Arrays 75
4.3.1 Magnetotransport Measurements for Antidot Arrays with varied antidot diameter 75
4.3.2 Origin of the high-field slopes 77
4.3.3 Summary 80
4.4 Easy and Hard Axis Magnetization reversal for small d/a ratio 82
4.4.1 Modified Sample Setup 83
4.4.2 Setup of micromagnetic simulations 85
4.4.3 Resolving Anisotropy by AMR measurement in FIB-selected crystallites 86
4.4.4 Easy Axis Reversal 88
4.4.5 Hard Axis Reversal 90
4.4.6 Summary 93
4.5 Magnetization reversal for large d/a ratio 94
4.5.1 In-plane anisotropy investigated by magnetotransport measurements and micromagnetic simulations 94
4.5.2 Investigation of the magnetization reversal by MFM and X-PEEM . . 101
4.5.3 Summary 107

5 Summary 109

Bibliography **113**

Introduction

Ever since advances in lithography provided the necessary tools to create well-defined structures on a sub-micron scale, researches used these tools to build tiny magnets. Complemented by the invention of a set of magnetometry technologies which possess the sensitivity and spatial resolution to investigate such magnets, the field of *nanomagnetism* was born. One important driver hereby still is the perspective to put the findings to use in magnetic data storage applications. In today's magnetic hard disks, for example, a single bit of binary information is stored in a magnetized region merely extending $40 \times 100\,\mathrm{nm}^2$ [1].

From a more fundamental point of view, the magnetic properties alter significantly once the spatial dimensions of a magnet approach its intrinsic length scales, such as the domain wall width. Prominent examples are the distinct magnetization configurations of thin magnetic discs with sub-micron diameters, where it comes to formation of a vortex [2], or uniformly magnetized nanoparticles [3, 4] which are often considered the ultimate goal in magnetic data storage.

In the present work, the influence of a nanoscaled lattice of holes on the magnetic properties of magnetically soft thin films is investigated. The periodically arranged holes, often referred as *antidots*, introduce a periodic shape anisotropy to the otherwise isotropic behavior of the polycrystalline thin films, as found by the micromagnetic study of Manzin et al. [5]. Additionally, the antidots are supposed to act as pinning sites for magnetic domain walls, hindering their movement during the magnetization reversal process [6], although direct experimental prove for that claim is often missing. Both mechanisms should provide leverage to tailor the magnetic properties of the antidot arrays, for example by changing the geometrical properties of the antidot lattice or the intrinsic magnetic properties of the thin film.

Especially potential control over domain wall pinning is of principle interest with respect to magnetic data storage: In the course of miniaturization, the size of the isolated, highly anisotropic grains of today's recording media are approaching the so-called superparamagnetic limit, so that their magnetization is prone to thermal excitation and long time data storage is impossible. Pinning sites at defined locations within a continuous, exchange coupled film are predicted to result in clear transitions between adjacent bits and therefore are discussed as a possible approach to further increase storage density [7, 8].

More recently, antidot lattices came into focus in context with the upcoming field of magnonics, where spin waves are used to transmit and process information [9]. With their periodic arrangement, the holes shape the band structure for the spin waves, in analogy to the electron bands in a solid resulting from the periodic arrangement of nuclei. Such a magnonic crystal can then act as a band filter for the spin waves, rejecting the frequencies within its band gaps [10].

Furthermore, striking parallels between the magnetization patterns for certain antidot geometries and so-called artificial spin-ice systems have been discovered in the course of this work. The term artificial spin-ice refers to arrays of lithographically defined interacting nanomagnets, arranged in a two-dimensional, frustrated geometry. Localized excitations in such a system which, although they are not in contradiction with Maxwell's equations, exhibit many characteristics of the theoretically postulated magnetic monopole [11] have drawn a lot of research attention to the topic [12, 13, 14].

Nanosphere lithography offers itself as a tool to realize such periodic antidot arrays. The approach makes use of the forces acting between polystyrene (PS) nanospheres which drive a self-assembly process. The spheres usually arrange in a hexagonal close packed monolayer on the substrate, and the selection of the spheres' average diameter determines the periodicity of this lattice. Variability is added to the approach by the possibility to reduce the diameters of the spheres by means of reactive ion etching (RIE), ideally without changing their positions on the lattice. The resulting template can now be transferred into an antidot array by depositing the magnetic material on top, followed by a polishing step which removes the spheres. In this context, the first goal of this work was to create suitable template masks based on previous results in the Institute of Solid State Physics [15]. The focus hereby was set on the optimization of templates with a periodicity of $200\,\mathrm{nm}$. At these length scales, the magnetic properties of the investigated materials Iron, Cobalt and Permalloy turned out to be strongly altered. On the other hand, the spatial resolution of the available microscopic magnetometry techniques was sufficiently high in order to study these structures. The second and main goal of the work is then to obtain a detailed understanding of how the nanostructures affect the magnetization of the thin films.

The present thesis is divided into five chapters. **Chapter 1** briefly covers the subjects ferromagnetism and magnetoresistive effects, as the latter are used for the characterization of the antidot samples. The end of the chapter is dedicated to introduce the concept of artificial spin-ice on the basis of a literature overview.
In **Chapter 2**, a detailed description of the preparation process is given, and the benefits and limitations of the self assembly approach are discussed.
The magnetic properties of the antidot samples were investigated by Superconducting

Quantum Interference Device (SQUID) magnetometry, magnetotransport measurements, magnetic force microscopy (MFM), Scanning Transmission X-Ray Microscopy (STXM) as well as X-Ray Photo Emission Electron Microscopy (X-PEEM). These techniques are presented in **Chapter 3**. Hereby, MFM, with its rather complicated image formation is discussed in more detail. All of the applied characterization methods were complemented by micromagnetic computer simulations.

The results of the magnetic characterization of the antidot arrays are presented in **Chapter 4**. One important aspect hereby is to attribute the amplified coercive fields of antidot arrays, as compared to planar reference films, to either domain wall pinning or a shape anisotropy. This distinction is mostly ignored in literature.

The presence of the nanoscaled holes leads to characteristic magnetization patterns, which can be imaged by aforementioned microscopic magnetometry techniques. The results become comparably easy to interpret with the samples in their remanent states after saturation. In this context, the new possibility to create artificial spin-ice structures by means of colloidal lithography will be discussed.

There is a fundamental challenge in the precise characterization of the magnetic properties of self-assembled antidot arrays: the antidots only exhibit hexagonal order within crystallites extending over typically a hundred lattice constants. This lack of long range order implies that application of integral measurement methods, such as SQUID magnetometry, always results in an averaging over all present crystallite orientations, obscuring a possible in-plane anisotropy. A method based on a simple magnetotransport measurement is presented which is suitable to overcome this problem.

Finally, in **Chapter 5**, the findings of this thesis are summarized.

1 Fundamentals

As a foundation for the subsequent discussion of the magnetic properties of antidot arrays, the present chapter begins with a brief overview of the topics ferromagnetism and magnetoresistive effects. Due to the striking resemblance between the magnetization patterns occurring in such antidot arrays and the ones found in so-called artificial spin-ice systems, the last section of the chapter will introduce this topic as well.

1.1 Ferromagnetism

The term ferromagnetism is often synonymously used for the phenomenon magnetism in general. This is due to the strong interactions between ferromagnetic bodies, which exceed magnetic interactions between para- or diamagnetic materials by several orders of magnitude [16]. In a ferromagnet, as well as in a paramagnet, atoms or molecules possess a magnetic dipole moment $\vec{m}$, each of which creating a magnetic field. While in a paramagnet, the orientation of these moments is random in the absence of an external applied magnetic field, there is a strong tendency towards a parallel alignment of the magnetic moments in a ferromagnet caused by the so-called exchange interaction (see next Section). As a consequence of this collective alignment, the magnetic fields created by a ferromagnet are so strong. In this context, another important measure is defined: The magnetization $\vec{M}$ is the magnetic dipole moment per unit volume V

$$\vec{M} = \frac{\vec{m}}{V}. \tag{1.1}$$

A ferromagnet's magnetization is dependent on the temperature and the externally applied field, but also on the history of its magnetization. This gives rise to the ferromagnetic hysteresis, as is depicted in Figure 1.1.

1.1.1 Exchange Interaction

In 1926, both Heisenberg and Dirac independently reported on an interaction between quantum mechanical particles, with which it was possible to explain why the magnetic

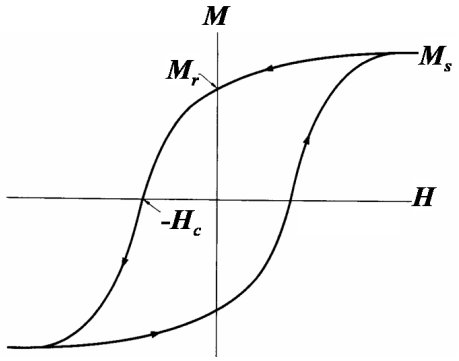

Figure 1.1: Schematic hysteresis loop of a ferromagnet. At the coercive field H_c, the magnetization is zero. At zero field, the ferromagnet exhibits its remanent magnetization M_r. The ferromagnet's magnetization never exceeds its saturation value M_s. Image from Ref. [17].

moments in ferromagnets align parallel to each other [18, 19]. This effect was named exchange interaction. Within the Heisenberg model, the exchange interaction energy between neighboring magnetic moments reads:

$$E_{ex} = -J_{ij}\vec{S}_i \cdot \vec{S}_j \tag{1.2}$$

, where $\vec{S}_i = \vec{m}_i/|\vec{m}_i|$. For a ferromagnet, the coupling constant J_{ij} is positive, so that a parallel alignment of spins results in a reduction of interaction energy, while a negative J_{ij} describes antiferromagnetic ordering. When instead of localized magnetic moments the magnetization M is regarded as a property in the sense of a continuum theory, which is especially relevant in the context of micromagnetic simulations (see Section 3.5), the exchange energy can be expressed as:

$$E_{ex} = \int_V \frac{A}{M_S}\left(\left(\frac{\partial\vec{M}}{\partial x}\right)^2 + \left(\frac{\partial\vec{M}}{\partial y}\right)^2 + \left(\frac{\partial\vec{M}}{\partial z}\right)^2\right)\mathrm{d}\,V. \tag{1.3}$$

Here, the exchange stiffness constant $A = \frac{cJS^2}{a}$ is introduced. a is the lattice constant, and the parameter c attains the values 1, 2 and 4 for sc, bcc and fcc lattice symmetry, respectively [20].

1.1.2 Magnetocrystalline Anisotropy

The energy corresponding to a given magnetization configuration of a ferromagnet depends on the relative orientation of the magnetization vector $\vec{M}$ and the crystal axes of the material. The origin of this magnetocrystalline anisotropy is the spin-orbit interaction.
The magnetization favors certain crystal directions, so that the ferromagnet is easily sat-

urated by means of an external field in these directions. Once the magnetization points in a favorable direction, rather large external fields are required to change the orientation, resulting in a square-like hysteresis loop. Such directions which minimize the energy, are called easy axes. This terminology is independent of the origin of the anisotropy. For a magnetocrystalline easy axis, however, the orbital contribution to the magnetic moment is always maximized [21]. The energetically most unfavorable orientations of the magnetization are then called the hard axis. It takes relatively large fields to force the magnetization into such a direction, and once the external field is turned off, there is a tendency for the magnetization to rotate into a neighboring easy axis. In Figure 1.2, the hysteresis loops for both cases are sketched.

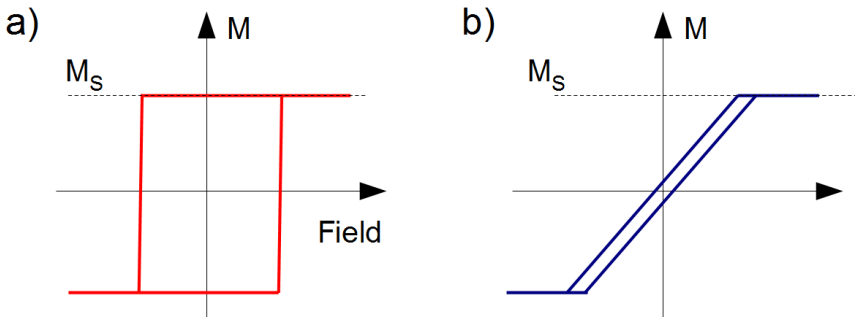

Figure 1.2: Schematic hysteresis loops for a field applied in (a) easy axis and (b) hard axis.

The characteristics of magnetocrystalline anisotropy depend on the crystal symmetry and the electronic configuration of the ferromagnet. For the antidot arrays prepared in this thesis, the shape anisotropy (see next Section) always dominates the magnetocrystalline anisotropy. This is due to the relatively small intrinsic values for the anisotropy constants of the materials used for the thin film preparation. The polycrystalline growth of these materials (see Section 2.3) further reduces the relevance of the magnetocrystalline anisotropy as compared to shape anisotropy.

1.1.3 Shape Anisotropy

Each of the atomic magnetic moments constituting the overall magnetization $\vec{M}$ of a ferromagnet creates a magnetic field $\vec{H}$:

$$\vec{H}(\vec{r}) = \frac{1}{4\pi}\frac{3\vec{r}(\vec{m}\vec{r}) - \vec{m}r^2}{r^5} \tag{1.4}$$

The magnetic moments are not only coupled to each other by the short range exchange interaction, but also by this long range dipolar interaction. However, in a homogeneously magnetized volume, the magnetic field created by a dipole is extinguished by the magnetic

fields arising from its neighbors. Only changes in magnetization are sources and sinks of a magnetic field. This so-called demagnetizing or stray field is given by [22]:

$$\vec{H}_{stray}(\vec{r}) = \int_{V_S} -\operatorname{div}\vec{M}_S(\vec{r}')\frac{\vec{R}}{|\vec{R}|^3}\,\mathrm{d}\,V' + \int_{A_S}\vec{n}\cdot\vec{M}_S(\vec{r}')\frac{\vec{R}}{|\vec{R}|^3}\,\mathrm{d}\,A' \tag{1.5}$$

, where $\vec{R} = \vec{r} - \vec{r}'$. The first integration extends over the sample volume V_S, and the latter over its surface A_S with $\vec{n}$ being the unit vector normal to it. The stray field interacts with the samples magnetization, giving rise to the stray field energy:

$$E_{stray} = -\frac{1}{2}\int_{V_S}\vec{M}\cdot\vec{H}_{stray}\,\mathrm{d}\,V' \tag{1.6}$$

As the stray field energy depends on the shape of the sample, different magnetization directions are in general not equivalent, with the exception being a spherical body. This gives rise to the expression shape anisotropy. For example, when we consider a thin film, a magnetization perpendicular to the films surface (out of plane) results in a large stray field energy. This is a consequence of equation 1.5, where the second integrand would be non-zero over the whole film surface. On the other hand, a magnetization parallel to the surface (in-plane) only yields non-zero contributions at the edges of the film. The in-plane orientation is thus favored in thin films with small magnetocrystalline anisotropy.

For uniformly magnetized bodies, the stray field can be expressed in the form:

$$\vec{H}_{stray} = N\vec{M} \tag{1.7}$$

Here, N denotes the demagnetization tensor, which for simple geometries like spheres and ellipsoids has analytical solutions, but in generally requires numerical integration techniques for more complex shapes.

With the demagnetization tensor, the stray field energy can be written as:

$$E_{stray} = \frac{\mu_0}{2}\vec{M}_S N\vec{M}_S \tag{1.8}$$

1.1.4 Zeeman Energy

The energy of the interaction of a ferromagnetic body and an external magnetic field H_{ext} is:

$$E_Z = -\int_{V_S}\vec{M}\vec{H}_{ext}\,\mathrm{d}\,V' \tag{1.9}$$

It is therefore minimized, when magnetization and magnetic field are aligned parallel to each other.

1.1.5 Domains & Domain Walls

In general, the magnetization $\vec{M}$ of a ferromagnet is not homogeneous, but it fragments into a multitude of regions in which the magnetization is uniform. These regions are called domains. Two neighboring domains are seperated by a domain wall, where the magnetization gradually reorients over a distance in the order of several hundred lattice constants.

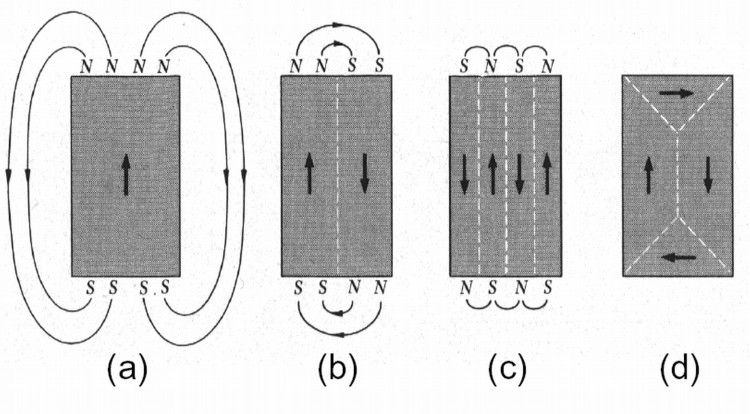

Figure 1.3: The formation of domains reduces the stray field energy. Details see text. Image from Ref. [23].

Domains form because of a competition of the different energy contributions which were discussed above. While a magnetization consisting of a single domain is favorable in terms of exchange interaction, the resulting demagnetizing fields are usually large, as sketched in Figure 1.3 a). Such a configuration is thus only possible if the stray field energy can be overcompensated by magnetocrystalline anisotropy. Splitting the sample into two domains of opposite magnetization directions reduces the stray field energy. The price for the additional domain is an increase in exchange energy due to the domain wall. A very favorable configuration is shown in Figure 1.3 d), where almost no stray field emerges at the samples edges due to a closure of the magnetic flux. Such a configuration, however, can only be attained when the magnetocrystalline anisotropy is negligible, for example in micronscaled rectangular prisms of Permalloy [24].

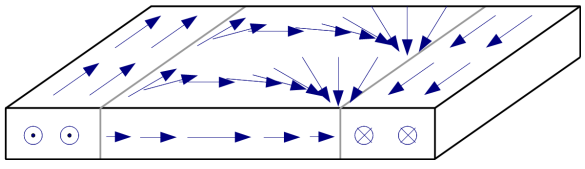

Figure 1.4: $180°$ Néel Domain Wall, as it usually occurs in soft magnetic thin films.

In bulk ferromagnets, the domain walls are usually Bloch walls. In a Bloch wall, the magnetization always stays within the domain wall plane. The term $\mathrm{div}\,\vec{M}$ in equation 1.5 is therefore zero, which minimizes the stray field energy due to the relatively small influence of the sample's shape. The width of the domain wall is hereby given by a competition between exchange interaction and the magnetocrystalline anisotropy.
In soft magnetic thin film elements, as the ones investigated in the course of the present work, the formation of Bloch walls would lead to an out of plane component of the magnetization, which is unfavorable due to shape anisotropy. Therefore, Néel walls separate neighboring domains. In such a wall, the magnetization stays within the plane of the film, as depicted in Figure 1.4.

In this context, the exchange length l_{ex} is an important property:

$$l_{ex} = \sqrt{\frac{2A}{\mu_0 M_s^2}} \tag{1.10}$$

On length scales of l_{ex}, the exchange interaction dominates dipolar interactions, and therefore has direct influence on the dimensions of domain walls. For the materials used for the preparation of the antidot arrays in this thesis, the values are $l_{ex} = 2.3\,\mathrm{nm}$ for Fe, $l_{ex} = 3.8\,\mathrm{nm}$ for Co, and $l_{ex} = 5.7\,\mathrm{nm}$ for Py [25]. The corresponding Néel wall widths in polycrystalline samples of these materials are in the range of 30 - $200\,\mathrm{nm}$ [26, 27]. In nanostructures with typical length scales of the natural domain wall width, the rigid separation between domain walls, in which the magnetization gradually rotates, and uniformly magnetized domain, often breaks down. This also holds for the present work and will be demonstrated in Section 4.2, where the magnetization in antidot arrays is investigated by magnetic force microscopy and micromagnetic simulations.

1.2 Magnetoresistive Effects

The term "magnetoresistive effects" refers to a variety of phenomena which incorporate a manipulation of the electrical resistivity by means of an externally applied magnetic field [28].
In the present work, magnetotransport measurements play a major role in the characterization of the magnetization reversal of the antidot samples. Especially the Anisotropic Magnetoresistance (AMR) is suitable for that task. However, apart from this desired effect, in every ferromagnetic sample one can principally observe the Positive and Negative Magnetoresistive Effects as well. A brief overview over the relevant phenomena shall be given in the following.

1.2.1 Anisotropic Magnetoresistance (AMR)

The anisotropic magnetoresistive effect was first reported in 1857 by W. Thomson [29]. The term refers to a dependence of the electrical resistivity $\rho(\vec{r})$ of a ferromagnet on the angle α enclosed by the magnetization $\vec{M}(\vec{r})$ and the current density $\vec{j}(\vec{r})$. It is usually the dominant magnetoresistive effect as long as the investigated sample is not saturated, while for fields above saturation the other magnetoresistive effects as briefly described at the end of the section determine the resistivity's dependence on the magnetic field.

For polycrystalline samples, i.e. when any anisotropy is lost due to orientational averaging, this dependence reads [30]:

$$\rho = \rho_{\perp} + (\rho_{\parallel} - \rho_{\perp}) \cos^2 \alpha \tag{1.11}$$

Here, $\rho_{\perp}$ and $\rho_{\parallel}$ stand for the resistivity resulting from magnetization oriented perpendicular or parallel with respect to the current density. Usually, $\rho_{\perp}$ is smaller than $\rho_{\parallel}$, although there are few exceptions [31].
The magnetoresistance ratio, defined as

$$\frac{\rho(H) - \rho(H=0)}{\rho(H=0)} = \frac{\Delta\rho}{\rho(H=0)} \tag{1.12}$$

can attain values of up to 5% in NiCo and NiFe binary alloys [32, 33]. Due to the relative ease of a resistance measurement, the AMR effect was used in many field sensing applications, including read heads for magnetic hard disk drives in the 1990s before more sensitive sensors based on Giant Magnetoresistance [34, 35] became available. More recently, changes in resistivity due to AMR of up to 50% was reported in cubic U_3As_4 [36]. A very strong spin-orbit coupling and large changes of the density of states of both spin-up and spin-down electron bands around the Fermi level are discussed as possible reasons for the high magnetoresistance ratio.
For elemental ferromagnets, this ratio is drastically reduced. For example for Fe, the material mainly used for the preparation of the antidot samples in this work, a maximum value of 0.2% at room temperature and 0.3% at a temperature of $77\,\mathrm{K}$ had been reported [30]. According to aforementioned reference, increase of the magnetoresistance ratio is caused by an increasing saturation magnetization for lower temperatures, as described by Bloch's Law [37]. Furthermore, grain size and film thickness can influence the magnetoresistance ratio [38]. Hereby, however, the ratio's numerator $\Delta\rho$ stays almost constant, while the denominator $\rho(H = 0)$ changes. In other words, the relative change in resistance due to AMR becomes smaller, the more magnetization independent scattering of the conduction electrons takes place within the sample.

The origin of the AMR effect lies within the spin-orbit interaction [28]. The spin-orbit interaction results in a non-spherical-symmetrical charge distribution of the ions cores constituting the ferromagnetic metal. Therefore, the scattering cross-section which the ions present to the conduction electrons is also not spherical. On the other hand, as a result of spin-orbit interaction, the orientation of this asymmetry is determined by the orientation of the spin. This is illustrated in Figure 1.5, where the charge distribution is depicted as a red cloud and the spin as a blue arrow.

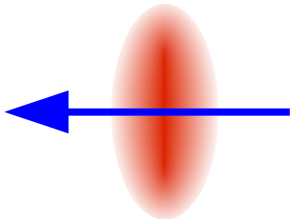

Figure 1.5: Anisotropic Magnetoresistance is caused by a non-spherical charge distribution (red cloud). The orientation of the charge cloud is coupled to the direction of the spin (blue arrow).

1.2.2 Positive Magnetoresistance

The “normal” or positive magnetoresistance results from the Lorentz force exerted by a magnetic field on the conduction electrons. It can therefore be observed in every conductor and is not restricted to ferromagnets.
The effect follows Kohler’s Rule [30]:

$$\frac{\Delta\rho}{\rho(H=0)} = f\left(\frac{B}{\rho(H=0)}\right) \tag{1.13}$$

Here, f labels a material-dependent function while B is the absolute value of the magnetic flux density. In very pure metals this effect can lead to resistivity changes of 5% at fields of $100\,\mathrm{kOe}$ and liquid helium temperature. At room temperature and in polycrystalline samples, the effect is usually obscured by anisotropic magnetoresistance or negative magnetoresistance.

1.2.3 Negative Magnetoresistance

In 3d-transition metals, the electrical current is mainly driven by the electrons of the s-band. The resistivity, on the other hand, results from scattering of these s-electrons into free states of the d-band. If the metal is a ferromagnet, the d-band splits into a majority-spin and a minority-spin sub-band. The majority-spin band’s energy can even be reduced below the Fermi level. Then, the majority-spin s-electrons cannot scatter into the d-band anymore, which reduces the overall resistivity of a ferromagnet compared to a non-magnetic counterpart [28, 39]. The energy difference between majority-spin and minority-spin band

can be amplified by an external field, which in turn further reduces the resistivity. This effect is isotropic, i.e. it does not depend on the relative orientation of current and magnetic field.

1.3 Artificial Spin-Ice Systems

In Section 4.2 it will be demonstrated that the magnetization of a hexagonal antidot array shows many similarities to the magnetization pattern observed in so-called artificial spin-ice structures. These model systems are two-dimensional, lithographically prepared ferromagnetic nanostructures, which mimic the magnetic behavior of spin-ice materials, most prominently of the Pyrochlores $Dy_2Ti_2O_7$ and $Ho_2Ti_2O_7$. Due to the larger scale of the artificial systems as compared to their natural counterparts, the former enable direct microscopic observation of many phenomena which are otherwise inaccessible or can only be measured indirectly.
These phenomena extend to the field of geometrical frustration, non-vanishing zero point entropy, and the emergence of a quasi-particle which shows many parallels to the (predicted) properties of a magnetic monopole, which thus far avoided detection despite considerable effort.
In the following, a brief overview of these phenomena and their underlying physics will be given as a foundation for subsequent discussion of the magnetic properties in the antidot arrays.

1.3.1 Geometric Frustration

In a geometrically frustrated system, it is impossible to minimize the energy of all pairwise interactions at a given lattice position [40]. The most basic example of such a system is a triangular lattice of spins, in which each lattice point is antiferromagnetically coupled to its two neighbors [41], as shown in Figure 1.6. The spins shall be Ising spins, i.e. they have two possible orientations which are anti-parallel to each other [42]. When we occupy the first lattice position with an up-spin, the second position has to be occupied by a down-spin in order to satisfy the antiferromagnetic condition. For the remaining position,

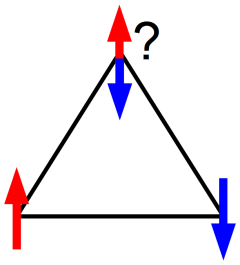

Figure 1.6: Prototypical example of geometric frustration: Triangular lattice of antiferromagnetically coupled Ising spins.

it is impossible to minimize both interactions at the same time. In this extreme example, both possible configurations result in the same total energy, i.e. the system is degenerated.

1.3.2 Spin-Ice

The spin-configuration of the materials termed “spin-ice” resembles the proton configuration in hexagonal water-ice to a large extend [43]. In the latter, each Oxygen atom is the center of a tetrahedron, whose corners also consist of Oxygen atoms, as illustrated by the empty circles in Figure 1.7 A). Many of the astonishing properties of water-ice result from the configuration of the Hydrogen atoms. A Hydrogen atom is situated in between each pair of neighboring Oxygen atoms. The protons, however, do not occupy the central positions between such a pair. Instead, each Oxygen atom forms covalent bounds with two of the protons, while it binds by hydrogen bonds to the remaining two. The former result in a shorter interatomic distance, the latter in a larger one, i.e. each Oxygen atom has two close and two far protons (see the dark circles in Figure 1.7 A). This is the famous ice-rule as postulated by L. Pauling in 1935 [44], which was later experimentally confirmed.

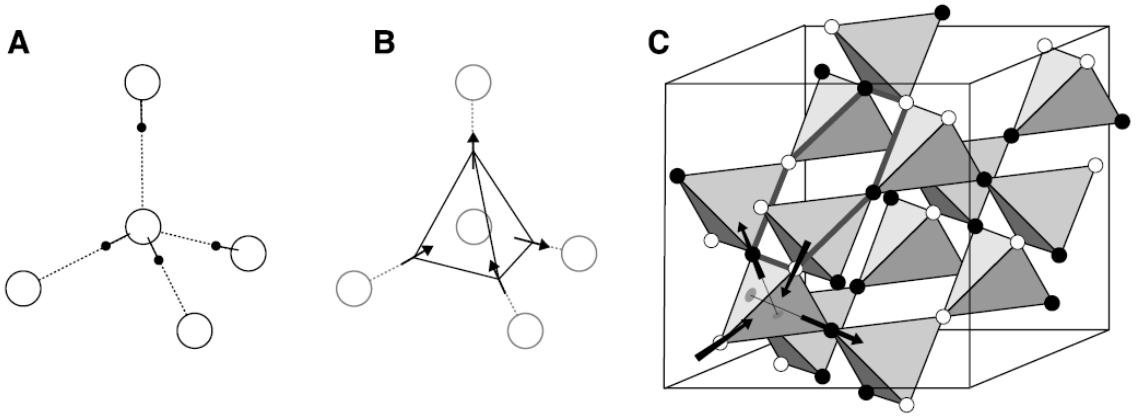

Figure 1.7: (A) shows the arrangement of atoms in water-ice around an Oxygen site (big empty circles). Each Oxygen atom has two “close” protons (small circles), which are covalently bound to it, and two “far” protons, each forming a hydrogen bound with respect to the central Oxide. In (B), the positions of the protons are indicated by a vector, which gives their displacement with respect to the center between two neighboring oxides. (C) The Pyrochlore lattice of $Ho_2Ti_2O_7$. The magnetic moments are situated on the corners of the tetrahedra and behave as Ising spins. Image from Ref. [45].

In an ice-crystal, there are many configurations which are compatible with the ice-rule, all of them are energetically equivalent, i.e. the ground state is macroscopically degenerated. Therefore, the ice-crystal does not posses a perfect order, but is merely one realization of this pool of possibilities. This directly leads to a residual entropy even close to $T = 0$ K,

which according to Ref. [44] for a crystal consisting of N molecules is:

$$\Omega = k_B N \ln \frac{3}{2} \tag{1.14}$$

, where k_B is the Boltzmann constant.

In 1997, Harris et al. found that in the Pyrochlore $Ho_2Ti_2O_7$ no long-range ferromagnetic order is formed even at very low temperatures, although the moment-carrying Ho^{3+} ions show a significant ferromagnetic coupling among each other [46]. The $Ho_2Ti_2O_7$ crystal is formed out of corner-sharing tetrahedra, as illustrated in Figure 1.7 C). The corners of these tetrahedra are occupied by the Ho^{3+} ions. Their magnetic moment of more than $\mu = 10\mu_B$ is confined by a very strong magnetocrystalline anisotropy to orient along an axis which connects the ion site with the center of the opposing triangular face [45]. Each magnetic moment can thus be approximated by an Ising spin.

As for water-ice, there is a residual entropy associated with the magnetic moments in spin-ice materials which is very well described by equation 1.14 [43]. In further analogy, the Ising-spins obey to spin-ice-rules. For spin-ice, they read “two in - two out”, meaning that two spins point towards the tetrahedron center and the other two away from it [47]. This rule, which dictates the short range spin-arrangement, minimizes the dipole-dipole interaction within a tetrahedron, which due to the large magnetic moment of the Ho^{3+} ions dominates the total interaction energy.

The situation of the interacting Ising spins in spin-ice is an outstanding example for a geometrically frustrated system. Each spin can achieve the favorable “head-to-tail” configuration with two of its three neighbors within a tetrahedron. In order not to lose this, the interaction with the remaining neighbor has to be sacrificed by taking a head-to-head orientation.

Castelnovo et al. suggested an alternative description of the physics in spin-ice systems [47], which becomes especially convenient when it comes to violations of the ice-rule. They introduced the magnetic charges $\pm q$, which reside at the end of a dumbbell of length a_t, with a_t being the distance between the centers of two neighboring tetrahedra, as illustrated in Figure 1.8. The charges are connected to the magnetic moment μ by the relation $\pm q = \mu / a_t$. In this picture, the ice-rule for the α-th tetrahedron simply becomes $q_\alpha = 0$.

The ice-rule does not always apply. For example, by offsetting the dipole-dipole interaction by means of an external field, it is possible to create local violations of the ice-rule. If one takes a spin configuration as a starting point in which all tetrahedra are oriented according to the ice-rule, flipping of a single magnetic moment creates charges $\pm q$ in its two adjacent

tetrahedra. This situation is depicted in Figure 1.8 d).

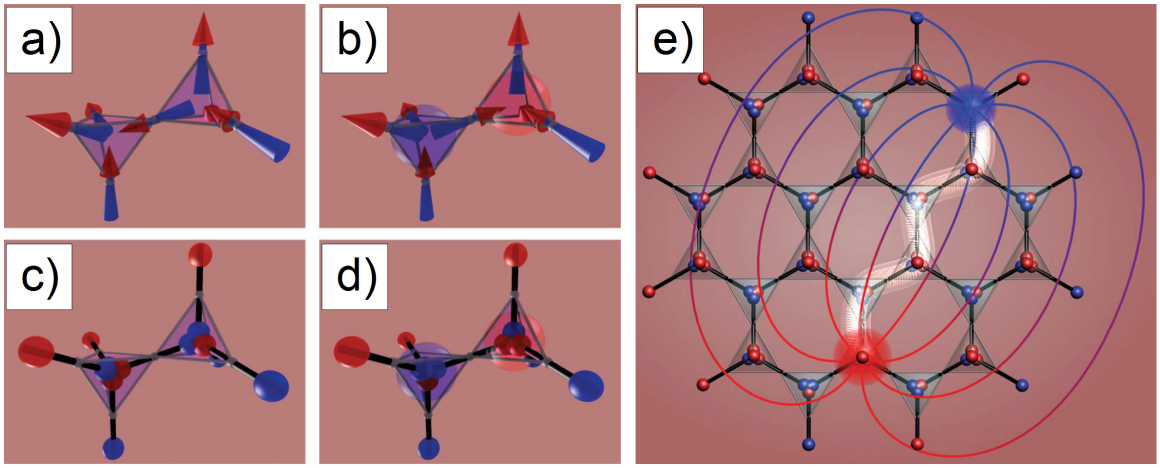

Figure 1.8: (a) Magnetic moments of the Ho ions within two tetrahedra in a configuration which obeys the “two-in two-out” ice rule. In (b), one of the moments flipped, so that the ice-rules don’t apply anymore. (c) and (d) show the same situation as in (a) and (b), respectively. However, the dipole moment μ is modeled as a dumbbell of length a_d with charges $\pm q$ on its ends. In (d) it becomes obvious, that flipping of a single moment leads to a spin-rule violation with a charge of $\pm q$ rising in the two neighboring tetrahedra. (e) shows a projection of the pyrochlore lattice on a (111) plane, where the tetrahedra form a so-called Kagomé lattice. A situation is depicted, in which two ice-rule violations, i.e. an antimonopole-monopole pair, are spatially seperated from each other. Along the line emphasized in white, the spins have flipped. Images from Ref. [47].

Such type of ice-rule violation, often simply labeled as “defect”, shows interesting properties which resemble the postulated properties of a magnetic monopole. As illustrated in Figure 1.8 e), the two opposite charges, often referred to as monopole $(+q)$ and antimonopole $(-q)$, resulting from the reversal of a single moment can be spatially seperated from each other without causing any additional violation. This can be achieved by inverting spins along a chain, which connects the two charges (see white line in Figure 1.8 e). In analogy to the 1-dimensional physical object that feeds magnetic flux into the volume elements of where magnet monopoles reside as postulated in 1931 by Paul Dirac [11], these paths are often referred to as Dirac Strings. Once created, the interaction energy between two charges at positions α and β can be described by following equation [47]:

$$E_{dip,\alpha\beta} = \frac{\mu_0}{4\pi} \frac{q_\alpha q_\beta}{r_{\alpha\beta}} \tag{1.15}$$

With its r^{-1} distance dependence, the equation shows remarkable resemblance with the Coulomb interaction between two electrical charges. While this result is expected due to the above definition of the magnetic charges $\pm q$, the important aspect at this point is that

the interaction between the two charges is *exclusively* given by equation 1.15. This implies that for very large distances, the interaction between the monopole anti-monopole pair vanishes, i.e. these quasi particles can travel freely in the pyrochlore lattice.
In any ferromagnet, a magnetic charge can be defined as div$\vec{M}$. These charges also interact via “magnetic Coulomb interaction”. However, there will always be other contributions in their interaction, too. For example, when one inverts the magnetization along a 1-dimensional path within a previously saturated ferromagnet, one would create charges of opposite sign at each end of the path. But these charges can never be fully seperated from each other, as the domain wall energy scales linearly with the length of the path.

1.3.3 Artificial Spin-Ice

The term artificial spin-ice refers to lithographically defined arrays of ferromagnetic nanostructures, arranged in a geometrically frustrated geometry. Typical length scales range from several $100\,\mathrm{nm}$ up to the micron regime. The nanostructures assembling the array are generally elongated magnetic islands or wires, which constitute the analog of the Ising spins in bulk spin-ice. Due to the small size and strong shape anisotropy, their magnetization attains a single domain configuration, preferentially aligned along their long axis. Therefore, they are often referred to as “macrospins”.

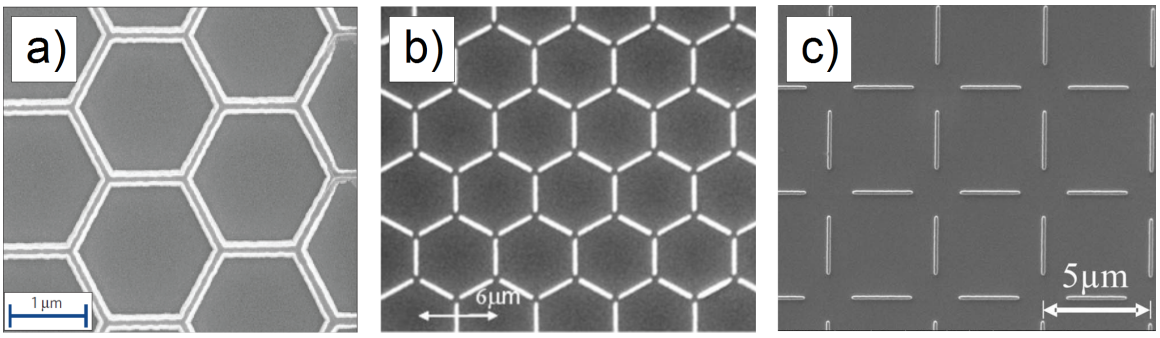

Figure 1.9: SEM images of various artificial spin-ice geometries: (a) continuous honeycomb [48], (b) isolated honeycomb [49], (c) isolated square [50].

Several geometrical arrangements of these macrospins have been investigated. Apart from square lattices, most publications are dedicated to honeycomb lattices. For both cases, the nanostructures can either be isolated from each other, i.e. form islands, or assemble a interconnected lattice. While in the former case, interaction between macrospins is strictly dipole-dipole, connected nanostructures are additionally exchange coupled. In the latter case, domain wall pinning on the kinks between two wires ensures that they can still be described as macrospin. Figure 1.9 presents Scanning Electron Microscope (SEM) images of some typical geometries.

In the following the focus shall be set on the honeycomb lattice, due to the analogy with the hexagonal antidot lattice which will later be discussed in more detail. Arranging the macrospins in a honeycomb lattice resembles the bulk spin-ice geometry projected on the (111)-plane (c.f. Figure 1.8 e)). In both square- and honeycomb lattice, vertices arise, where either three (honeycomb) or four (square) macrospins meet. These vertices are the analog to the tetrahedra in bulk spin-ice. In the honeycomb lattice, all pairwise interactions are equivalent. In a square lattice, a macrospin has two near and one far neighbor at a vertex, which for example influences the degree of the degeneracy of the system [51].

Each macrospin has a magnetic moment of

$$\vec{\mu} = \int_V \vec{M} \, \mathrm{d}\, V \tag{1.16}$$

From the perspective of vertex, a given macrospin's moment points either into, or out of it. This results in 2^3 possible vertex-configurations (3 in, 3 out, $3\times$ 2 in - 1 out, $3\times$ 1 in - 2 out) in the honeycomb lattice. Again, it's practical to describe the spin-arrangements in terms of magnetic charge: At each end of the magnetic wire / island of length a, a charge of $\pm q = \mu/a$ arises. In bulk spin-ice, the ice-rule could be expressed as a minimization of the charge at each vertex: $q_{tot} = 0$. Due to the odd number of macrospins per vertex, this translates to $q_{tot} = \sum_{i=1}^{3} q_i = \pm q$ in honeycomb spin-ice.

A very distinct magnetization state in honeycomb spin-ice is achieved in remanence after saturation along one of the long axis of the macrospins, as depicted in Figure 1.10 a). This is the so-called charge ordered state, where the ice-rule apply for every vertex, and each charge $\pm q$ is surrounded by three charges of opposite sign. Switching of a single bar changes the sign of the adjacent vertices by $\pm 2q$. In Figure 1.10 b), two different switching events are shown. The switching of a non-vertical macrospin does not lead to a ice-rule violation, but simply inverts the sign of its vertices. When a vertical macrospin switches, the ice rules do not hold anymore and it comes to formation of a pair of $\pm 3q$ charges. Whether such violations occur in a given artificial spin-ice structure depends on the exact geometry. The closer the distances between macrospins on a vertex are, the larger the energy penalty for an ice-rule violation becomes [51]. But even in the case of exchange coupled wires, where the three charges of a vertex are only seperated by narrow domain walls, observations of the violation have been reported. In that context, Ladak et al. found that the wider the distribution in the macrospin coercive fields is, the more probably the ice-rule violations become [52].

What is now the analog to the monopole- anti monopole pair, as it appears in bulk spin-ice? Mengotti et al. suggest that one takes the charge ordered state as a reference point

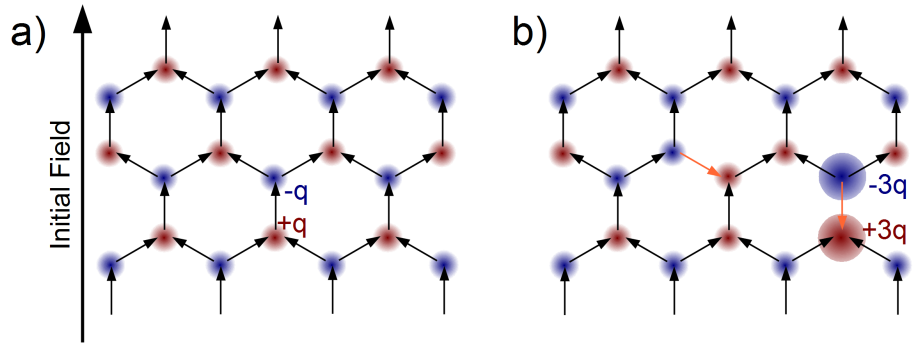

Figure 1.10: a) Remanent state after saturation along the indicated direction. At every vertex, the ice-rules apply and every negative charge has three neighboring positive charges. (b) Two switching scenarios: Reversing a spin parallel to the saturating field leads to charges $\pm 3q$, while switching of a spin of any other direction does just changes the sign of its adjacent vertex charges.

[12]. When now a reversal field is applied, single macrospins start to switch and change the charge of their vertices by $\pm 2q$, as described above. It is now these charge differences relative to the charge ordered state that can be seperated from each other by increasing the magnetic field, i.e. the $\Delta q = +2q$ charge difference travels parallel to the field vector and the $\Delta q = -2q$ vector in the opposite direction. Both charge differences are connected by a path of reversed macrospins, again called the Dirac String. One way to image these strings is Photo Emission Electron Microscopy (PEEM), where the reversed spins appear black, while the ones with original orientation are white (see Figure 1.11). In contrast to bulk spin-ice, however, the Dirac Strings here do not necessarily terminate in a ice-rule violations.

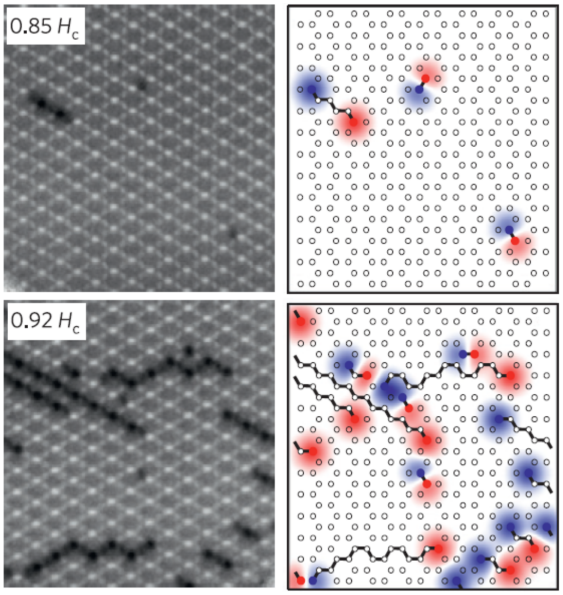

Figure 1.11: left column: PEEM images of honeycomb spin-ice at different fields. Macrospins pointing in the original saturation direction are white, reversed ones are black. Right column: Schematics of the magnetization states, together with the charges $\pm\Delta 2q$ at the beginning and end of a chain of reversed spins. From Ref. [12].

2 Preparation and structural characterization of Antidot Arrays

Preparation of the antidot samples plays a critical role for the present work. Only with precise control over the structural parameters of the samples, it is possible to investigate the interplay of geometry and magnetic properties. And only if the created nanostructures are sufficiently periodic, this periodicity will also reflect in the magnetization.
Antidot arrays have been realized by several lithographic techniques such as optical and deep-ultraviolet lithography [13, 53, 54], electron beam lithography [55, 56, 57] or focused ion beam (FIB) milling [58, 59]. While the optical approaches have a resolution limit due to the light's wavelength, the latter two approaches write their structures sequentially and are thus time consuming and expensive.
In contrast to aforementioned techniques, periodic nanostructures can be realized by bottom-up approaches based on the self-assembly of nanoparticles. The resolution of such a technique is then primarily given by the size of the particles, and self-assembled monolayers can be created on a time scale of minutes even on a centimeter length scale. For the sample preparation of this work, polystyrene (PS) nanosphere lithography was chosen, as suggested by Zhukov et al. [60]. Monodisperse PS nanosphere suspensions are nowadays commercially available with a wide range of sphere diameters. A critical accomplishment in the field is the possibility to vary the spheres' diameters after the self-assembly took place [15]. However, control of the environment of the self-assembly process to realize optimal results is challenging up to this day.

2.1 Preparation Process

In order to prepare large scale antidot arrays with geometrical parameters in the sub $200\,\mathrm{nm}$ regime, a modified variant of colloidal lithography based on previous works [61, 62] in the Institute of Solid State Physics at Ulm University is applied, exhibiting remarkable flexibility as well as the possibility to pattern substrates on a centimeter scale. The process consists of four steps (see Figure 2.1) and yields antidot arrays of hexagonal order with variable antidot lattice parameter a and hole diameter d. It does not pose any restrictions on the

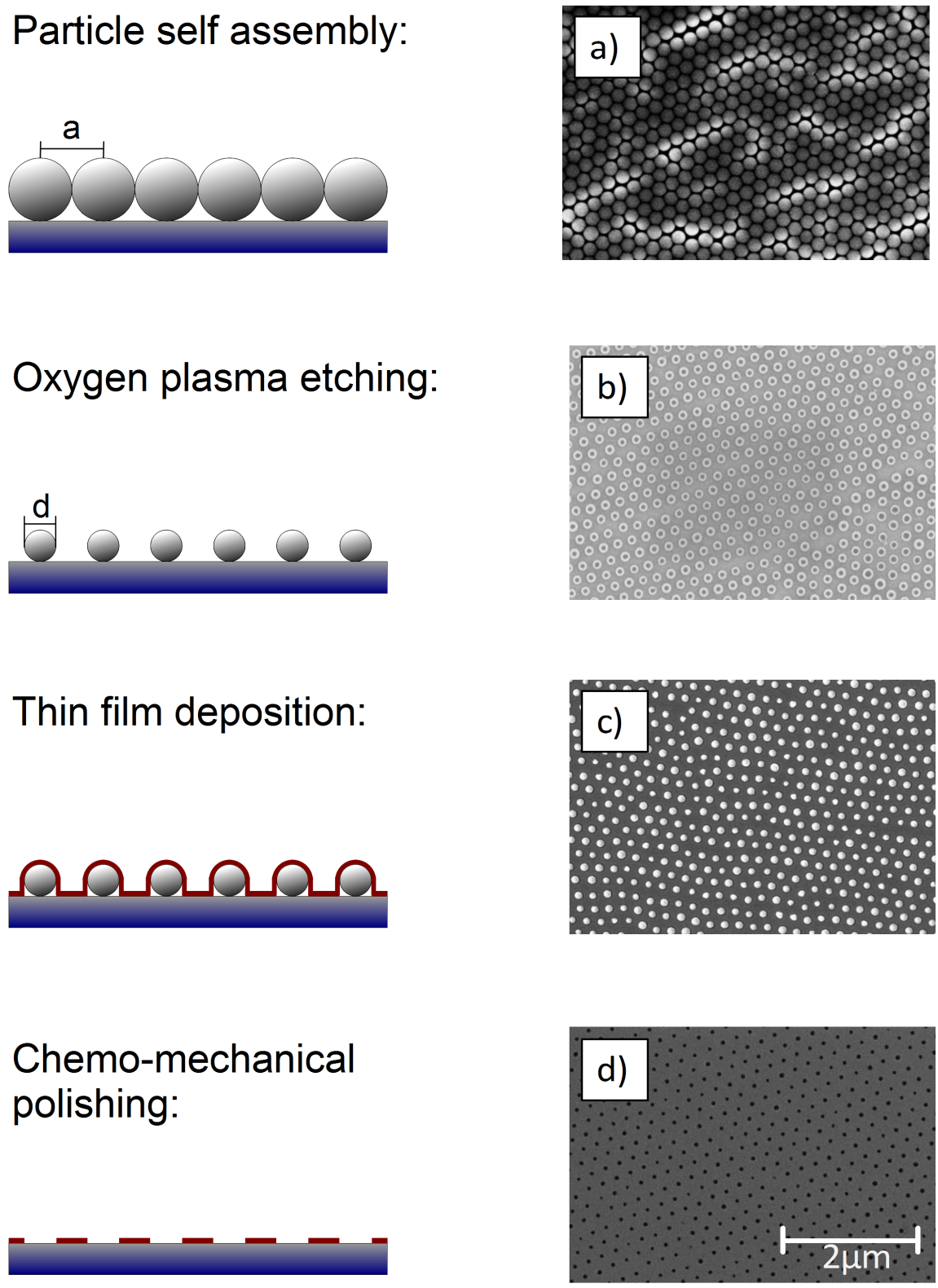

Figure 2.1: Schematics of the antidot preparation process (left column) and corresponding SEM micrographs taken after each step. a) Self-assembled, close-packed monolayer of PS spheres ($a = 200\,\mathrm{nm}$), b) after oxygen plasma etching ($100\,\mathrm{s}$), c) after deposition of a Fe film ($t = 20\,\mathrm{nm}$) and a Pt layer ($2\,\mathrm{nm}$) preventing oxidation, and d) after removal of residual PS spheres and their magnetic caps.

thin film material and allows variation of the film thickness t in a wide parameter range. In the following, the preparation steps are described in more detail:

2.1.1 Deposition of the Polystyrene (PS) Nanospheres

The first step of the pattern formation is the self-assembly of PS nanospheres on the substrate surface. The goal of this process is to achieve a hexagonally close packed monolayer of the polystyrene nanospheres. The nanospheres are commercially available [63] and are dispersed in water with a concentration of usually 8% (w/v). Mostly for economic reasons, this concentration is reduced to 1% (w/v) prior to deposition. PS sphere solutions with average nominal sphere diameters of 100, 200 and $500\,\mathrm{nm}$ are provided by Life Technologies Ltd. [63]. The choice of the initial sphere diameter determines the lattice constant a of the antidot array. All used nanosphere dispersions are labeled as “surfactant free latex” by the manufacturer. While the absence of a surfactant for particle stabilization can result in a variety of benefits [64], it turned out that addition of the surfactant sodium dodecyl sulfate (SDS) had a positive effect on the self-assembly [61] as well as on the subsequent plasma etching step. This is described in more detail at the end of this chapter.
Dependent on the purpose of the respective sample, either Silicon (if a conductive substrate was desired, for example for PEEM experiments) or a stack of a $300\,\mathrm{nm}$ thick, thermally grown Silicon Oxide layer on top of Silicon was used as a substrate (for the magnetotransport experiments, see Section 4.3). For X-Ray microscopy experiments, the process was carried out on Silicon Nitride substrates containing a $0.5 \times 0.5\,\mathrm{mm}^2$ large membrane windows from Silson Ltd. [65]. The membrane window’s thickness was $500\,\mathrm{nm}$.
For all substrate materials it has been necessary to increase the hydrophilicity for successful deposition of PS spheres. This is achieved by exposing the substrates to an Oxygen Plasma [66] (DC Bias $= -80\,\mathrm{V}$ for 5 minutes). Prior to the plasma treatment, the Si- and $300\,\mathrm{nm}$ SiO / Si Wafers were cut into pieces of a typical size of $15 \times 5\,\mathrm{mm}^2$, of which during the subsequent deposition process approximately $5\,\mathrm{mm}$ are covered by a clamp. The remaining $10 \times 5\,\mathrm{mm}^2$ of the substrate which become actually covered with spheres fit exactly to the sample holder of the Hitachi S-5200 Scanning Electron Microscope used for the structural characterization.

The deposition then took place by means of a dip-coating process: One end of the substrate is clamped to the so-called dip-coater - a computer-controlled device which comprises a precise motor for linear actuation of the substrate. The substrate is then dipped into the PS sphere dispersion and subsequently pulled out slowly (more details in next paragraph). The self-assembly is hereby driven by attractive capillary forces between the spheres and by the convective flow during solvent evaporation [67, 68]. According to [62],

best results in terms of size of the monolayer as well as the short range order of the nanospheres are achieved, when the angle between substrate and the surface of the dispersion encloses $60°$. This setting is therefore adopted.

The extraction velocity is the most critical parameter for the process. If it is chosen too slow, instead of the desired monolayer a multilayer of PS spheres is formed on the substrate, while when it is too fast the monolayer is not hexagonally close packed. The optimal extraction velocity depends on the diameter of the PS nanospheres (smaller diameters allow faster dipping velocities), their concentration (the higher the concentration, the faster the extraction velocity) as well as the temperature and the air humidity, as these determine the evaporation rate of the water. Therefore, the extraction velocity was optimized prior to the preparation of a series of samples, starting from a value of $10\,\frac{\mu\mathrm{m}}{\mathrm{s}}$. A typical result of the dip-coating process of PS nanospheres with an average diameter of $200\,\mathrm{nm}$ can be seen in the SEM-micrograph in Figure 2.1 a). For optimal extraction velocities, the monolayer extends to an area of approximately $5 \times 10\,\mathrm{mm}^2$, i.e. is restricted by the size of the substrate.

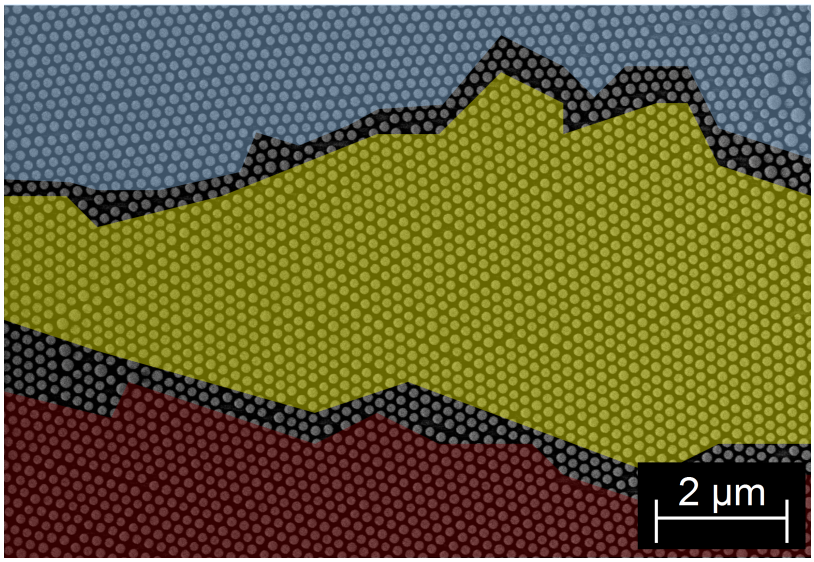

Figure 2.2: Etched Polystyrene spheres on SiO_2 substrate. The self organization process yields crystallites of constant lattice orientation, which are separated by grain boundaries. Each color corresponds to a different orientation of the template lattice.

However, the hexagonal order is not maintained over the whole monolayer. Very similar to a polycrystalline solid, it comes to formation of crystallites, in which the orientation of the hexagonal lattice is constant. These crystallites are seperated from each other by grain boundaries extending over typically $1 - 5$ lattice constants. This is illustrated in the SEM-Image of a monolayer of (already etched) $200\,\mathrm{nm}$ PS spheres in Figure 2.2, in which each crystallite is color coded. The dimensions of the crystallites roughly scale with the

sphere diameter. For PS spheres with a diameter of $200\,\mathrm{nm}$, they can cover areas of up to $25 \times 25\,\mu\mathrm{m}^2$. One has to be aware of that, especially when applying integral measurement methods like SQUID magnetometry: As will be shown later, the magnetic properties of the antidots exhibit a strong in-plane anisotropy which is coupled to the hexagonal antidot lattice orientation. The crystallites, however, are randomly oriented towards each other. In a SQUID experiment, in which samples of an area of usually $5 \times 3\,\mathrm{mm}^2$ are examined, the measured signal will always be comprised of contributions from all possible crystal orientations, i.e. it comes to an orientational averaging.

By the end of the experimental work of this thesis, a promising alternative approach for the self-assembly process became available in the course of the Bachelor Thesis of M. Hartmann [69], based on the work of Ho et al. [70]. The self-organization hereby takes place on a large scale (several $10\,\mathrm{cm}^2$) air water interface. By addition of a small amount of Polyethylene Oxide, the formed monolayer can be stabilized due to Polymer bridging effect between neighboring spheres. At this stage, the monolayer can be transferred onto substrates of suitable size, simply by pulling them through the monolayer with a set of tweezers. For PS spheres with a diameter of $200\,\mathrm{nm}$, this technique yielded crystallites larger than $50 \times 50\,\mu\mathrm{m}^2$. However, the PS dispersion used for these experiments was purchased from a different manufacturer, so that direct comparison is not possible at this point. The biggest advantage in comparison to the dip coating approach is the time efficiency. The large floating monolayer is sufficient to completely coat more than ten $5 \times 10\,\mathrm{mm}^2$ large substrates.

2.1.2 Plasma Etching of the PS Spheres

The flexibility of colloidal lithography has been greatly enhanced by the possibility to modify the diameter of the spheres after their deposition onto the substrate. While originally only close packed mono- or doublelayers could be prepared by colloidal lithography [71, 72], it is nowadays possible to create non-close-packed hexagonally ordered arrays by applying reactive ion etching (RIE) to the polystyrene spheres [15, 73]. The second step in the course of the preparation of the antidot arrays is the diameter reduction and therefore the transition to a non-close-packed structure which will serve as a template for the subsequent deposition of a magnetic thin film.

For the present work with its focus on periodic structures, an etching process was required which, apart from precise control over the sphere diameter, ensures that the positions of the centers of the spheres is maintained. Therefore, instead of the isotropic Oxygen plasma etching approach proposed in Ref. [15], where the spheres tend to change their

location if their diameter is reduced below 65% of its initial value, Oxygen plasma etching with a strong anisotropic component is applied. Together with the stabilizing effect of an increased concentration of the surfactant SDS (see end of this chapter), this allows for a reduction of the sphere diameter way below aforementioned limit without sacrificing hexagonal order.

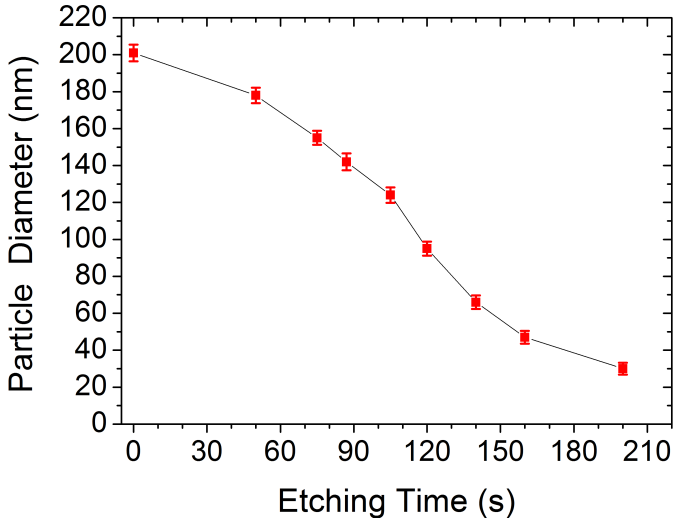

Figure 2.3: Polystyrene sphere diameter as a function of etching time in an Oxygen plasma with a DC bias voltage of $-80\,\mathrm{V}$. The initial sphere diameter is $201 \pm 4\,\mathrm{nm}$. The error bars represent the width of the Gaussian size distribution which stays almost constant during etching.

For the plasma etching, an Oxford Plasma Technology Type 80Plus combined RIE (Reactive Ion Etching) and ICP (inductively coupled plasma) source was used, which is described in more detail in [74]. The size reduction of the PS spheres was achieved in an Oxygen plasma with a 25W RIE component and $100\,\mathrm{W}$ ICP component at a DC bias voltage of $-80\,\mathrm{V}$. For PS spheres with a initial diameter of $200\,\mathrm{nm}$, the achieved diameter versus etching duration is plotted in Figure 2.3. While initially the etching rate is rather slow with approximately $0.4\,\frac{\mathrm{nm}}{\mathrm{s}}$, it accelerates to $1.2\,\frac{\mathrm{nm}}{\mathrm{s}}$ for diameters around 50% of the initial value. For longer etching times, the rate reduces again. This etching procedure fulfills all of the above requirements and allows a reasonably precise control of the sphere diameter. Due to the anisotropic component of the applied plasma, the polystyrene particles are no longer spherical, but become oblate. This, however, does not affect their usefulness as templates for a subsequent film deposition, as viewed from atop (see SEM micrograph in Figure 2.1 b)), the particles still appear circular.

2.1.3 Thin Film Deposition

Onto the etched Polystyrene particles the magnetic thin films are deposited by pulsed laser deposition (PLD). For the present work, antidot arrays within thin films of either Fe, Co or Permalloy ($Ni_{80}Fe_{20}$) were prepared. All of these materials possess only a small magnetocrystalline anisotropy and thus a low intrinsic coercivity (below $20\,\mathrm{Oe}$ at room temperature), as well as an preferred in-plane orientation of their magnetization due to shape anisotropy. Therefore, a strong change in the films' magnetic properties can be expected due to the incorporation of the nanostructures. On top of the magnetic films a 2 nm thick platinum cover layer is deposited to prevent oxidation.

The PLD setup uses a commercial COMPex 201 Excimer Laser from Lambda Physik (nowadays: Coherent) to vaporize the respective target material(s). The laser is capable of creating light pulses of a fixed wavelength of $\lambda = 193\,\mathrm{nm}$ with a pulse length of $20\,\mathrm{ns}$, pulse energies between 300 and $450\,\mathrm{mJ}$ and frequencies between 1 and $10\,\mathrm{Hz}$. These energies correspond to energy densities between 7 and $10.5\,\mathrm{J/cm^2} \pm 15\%$ on the target material, easily surpassing the ablation threshold, which is approximately $2\,\mathrm{J/cm^2}$ for the above metals [75].
For the deposition process, the pre-templated substrates and the target materials are placed in an UHV chamber with a base pressure of $5 \times 10^{-10}\,\mathrm{mbar}$. The targets are mounted on a computer controlled revolver, which allows to change the material during deposition and thus enables preparation of alloys. Their stoichiometry is determined by the ratio of pulses given on the respective materials and their deposition rates. Typical deposition rates for the materials used for the energies given above are between 0.5 and $1.2\,\frac{\mathrm{nm}}{\mathrm{min}}$. Hereby, the distance between target and substrate was set to approximately $5\,\mathrm{cm}$. More details on the setup can be found in [76, 77].

2.1.4 Removal of the magnetic caps & PS spheres

Deposition of the magnetic thin films on the pre-templated substrates results not only in film growth on the substrate, but also forms magnetic caps on top of the PS spheres (see Figure 2.1 c)). This kind of sample geometry was object of multiple investigations [78, 79]. It was found that the magnetic caps influence the magnetization in the planar part of the thin film. For well-defined samples it is therefore necessary to remove the caps. This can be easily achieved by manually rubbing the nanostructured surface under application of a small force (just enough to be able to move the sample) on an Aceton soaked stash of lens cleaning paper for a minute. The result can be seen in Figure 2.1 d). While the thin film survives the treatment without damages, the caps and spheres are reliably removed

on the whole sample. It is worth mentioning that this procedure can even be applied on Si_3Ni_4 membranes. This is shown in Figure 2.4: While the bright contrast in this image corresponds to an $20\,\mathrm{nm}$ thick Fe antidot array with $a = 200\,\mathrm{nm}$ and $d = 125\,\mathrm{nm}$ on a bulk Si_3Ni_4 substrate, the dark contrast corresponds to the antidot array on a only $500\,\mathrm{nm}$ thick membrane window. Even on the membrane, almost every magnetic cap together with the PS particles has been removed out of the Fe film.
An alternative method to remove caps and particles is the application of an ultra sonic bath with the sample surrounded by Acetone. However, this is only possible for massive substrates - the Si_3Ni_4 membranes break during this treatment.

Principally, the removal step opens the door for oxidation of the films. In practice, this issue turned out to be negligible. Neither the magnetic moment of the samples nor their coercivity changed significantly over time scales of several months.

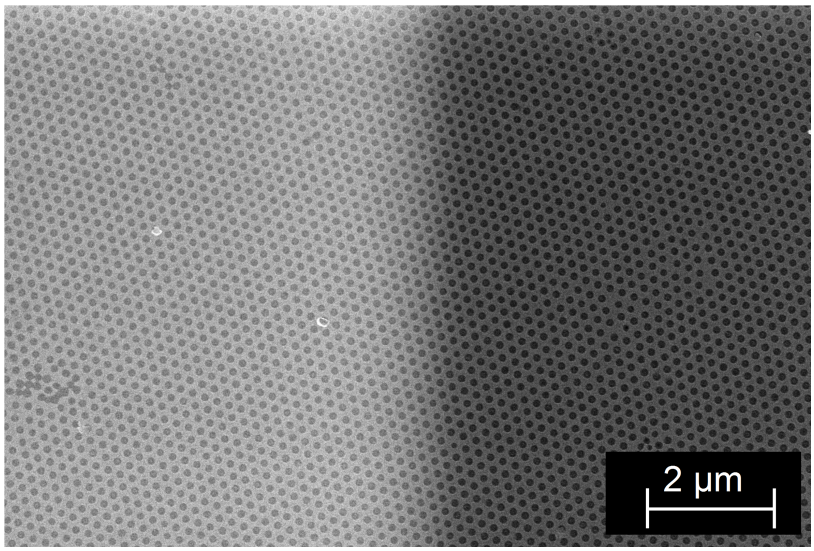

Figure 2.4: SEM-Image of an $t = 20\,\mathrm{nm}$ thick Fe antidot array with $a = 200\,\mathrm{nm}$ and $d = 125\,\mathrm{nm}$. The halve of the image exhibiting the darker contrast shows the antidot array on a $500\,\mathrm{nm}$ thick membrane window. Remarkably, these windows survive the mechanical polishing procedure. The image was recorded with an acceleration voltage of $30\,\mathrm{kV}$.

2.2 Effect of surfactant on template formation

The addition of the surfactant sodium dodecyl sulfate (SDS, $CH_3 - (CH_2)_{11} - SO_3O - Na^+$) to the originally surfactant-free PS dispersion positively affects the quality of the self-assembly of the nanospheres on the SiO surface. Equally important, it turned out that the etching properties of the nanospheres can also be altered in this way. After optimization of the surfactant concentration, a significant improvement of the short range order can be

observed and at the same time the problem of the changing particle positions for long etching durations can be overcome.

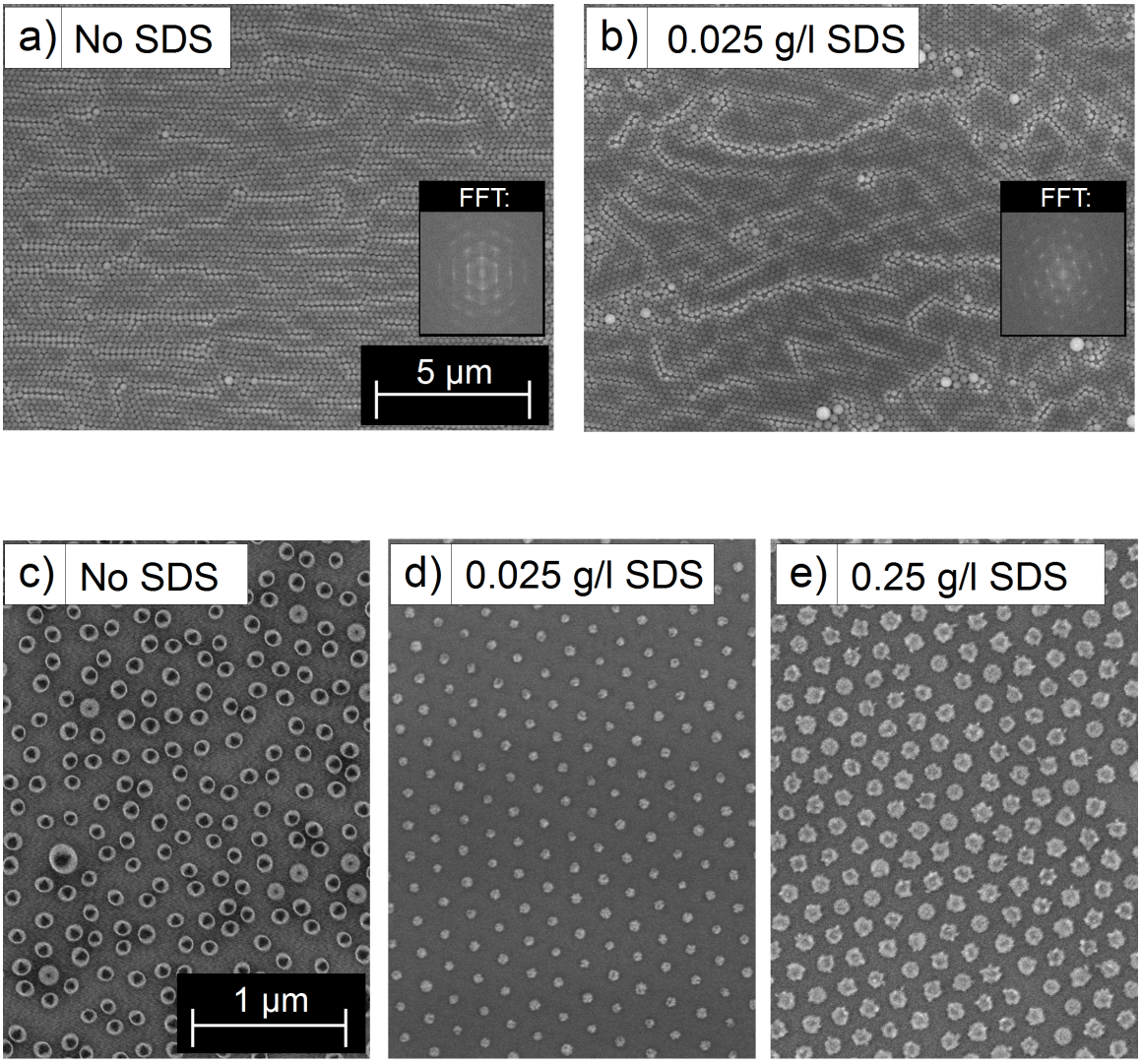

Figure 2.5: Effect of additional SDS on the template formation. (a) large scale image of a PS sphere monolayer (average diameter = $201\,\mathrm{nm}$; PS concentration 1% (w/v)) without additional SDS. For the monolayer shown in (b), the SDS concentration was $0.025\,\mathrm{g/l}$. SDS increases the short range order, but promotes the formation of smaller crystallites. (c) - (e): comparison of etching behavior. (c) no additional SDS, (d) SDS concentration $0.025\,\mathrm{g/l}$, (e) SDS concentration $0.25\,\mathrm{g/l}$. The added SDS stabilizes the positions of the PS spheres during the etching process, but for higher concentrations the spherical shape is lost.

In the top row of Figure 2.5, the self assembly properties of a PS nanosphere dispersion with a sphere diameter of $200\,\mathrm{nm}$ prior (a) and after (b) the addition of SDS to a concentration of $0.025\,\mathrm{g/l}$ can be compared. While the section of the monolayer depicted in (a) basically consists of a single crystallite, there are a lot of defects which disturb the short range order. This changes with the addition of SDS. The corresponding SEM-image shows that the crystallites are smaller and clearly seperated from each other. Within each crystal-

lite, however, the short range order is improved. This becomes clearer in the insets, which show the Fourier transforms from $2 \times 2\,\mu\mathrm{m}^2$ large, single crystallite areas of the respective figures. Compared to the sharp spots in the inset of (b), these spots are more smeared out due to the inferior short range order of the surfactant-free solution.
According to Yan et al., [80], the surfactant SDS dissociates in aqueous solution under formation of a negatively charged head group. After the SDS molecules attach to the PS spheres, their negative charge density is increased. On the equally negatively charged SiO_2 surface, the added SDS leads then to an increase in electrostatic repulsion between substrate and spheres during the self-organization. In turn, the mobility of the spheres is increased before they reach their final positions, which is likely to be the reason for the enhanced short range order.

In the bottom row of figure 2.5, the etching behavior of the same PS nanospheres for different concentrations of SDS is depicted. In image (c), which shows the result of application of the Oxygen plasma for $100\,\mathrm{s}$ for a PS solution without additional SDS, a hexagonal order is hardly recognized. Moreover, the majority of the particles does not appear spherical anymore. The loss of the hexagonal order is caused by a change in particle positions during etching. In Ref [15] it is shown that the spheres "roll" by approximately 25% of their circumference once their diameter is reduced to less than 65% of its original value. This movement reveals the oblate shape of the particles, which is a result from the application of an anisotropic plasma, even in a top-view SEM image.
In contrast to that, hexagonal order and circular shape of the template is maintained for an SDS concentration of $0.025\,\mathrm{g/l}$ (see image (d)), even for an etching time of $200\,\mathrm{s}$, resulting in an average particle diameter of $35\,\mathrm{nm}$. The reason for this stabilizing effect could be formation of a socket due to an accumulation of SDS molecules between substrate and particle, however this was not further investigated. An increase in SDS concentration to $0.25\,\mathrm{g/l}$ leads to a significant amount of residual SDS on the particle surface, which distorts their circular shape, as seen in image (e). The SDS concentration of $0.025\,\mathrm{g/l}$ is therefore considered the best compromise between long- and short range order for the $200\,\mathrm{nm}$ spheres and a mass concentration of 1% (w/v), and leads to the best results in terms of etching.

2.3 Determination of geometrical and structural parameters of the antidot arrays

The magnetic properties of antidot arrays strongly depend on the geometrical parameters of the array, namely the lattice parameter a and the antidot diameter d as well as their

respective size distributions. An efficient way to determine these parameters uses an top view SEM image of the antidot array of interest, as presented in figure 2.6 a), as a starting point for the subsequent analysis.

In order to determine the hole diameters, the freely available software *ImageJ* [81] is used. This software provides a routine which is able to identify the holes in the SEM micrograph ("Analyze Particles"). The threshold of the gray value which associates a pixel to either thin film or hole can be adjusted. However, due to the clear contrast, this setting has only a very minor influence on the results over a wide range of parameters, which makes the method very reliable. The software then delivers a illustration of the recognized holes (see Figure 2.6 b)) for control purposes and, more importantly, the area of each recognized hole. With that information, the corresponding diameters are easily calculated. Figure 2.6 c) displays the size distribution of the calculated hole diameters, which is well described by a Gaussian function.

For the determination of the antidot array's lattice parameter, the software WSXM [82] is used to calculate the self-correlation of the SEM image. The result is shown in figure 2.6 d). The good long range order of the antidot array results in a slow decay of the self-correlation. In the next step, a profile of the self-correlation along the blue line in (d) is plotted, which is shown in (e). Gaussian fits to the peaks reveals their positions. The distance between them is a good measure for the average distance between two neighboring hole centers, and thus for the lattice parameter of the antidot lattice.

Another critical property is the crystallographic structure of the deposited ferromagnetic thin films. Preferences in the crystallographic growth directions would lead to a competition between the shape anisotropy introduced by the antidots on the one hand (this topic will be addressed in more detail in Section 4.2) and the magnetocrystalline anisotropy on the other hand.

However, for none of the materials (Fe, Co and Permalloy) used for the preparation of antidot arrays in the course of this thesis such preference could be detected. Figure 2.7 exemplary shows the x-ray diffractogram from a Ω-2θ-scan of a $20\,\mathrm{nm}$ thick Fe reference film grown by pulsed laser deposition on a SiO_2 $(300\,\mathrm{nm})$ / Si substrate. The Fe film has a $2\,\mathrm{nm}$ thick Pt capping layer. The wavelength of the X-rays was $\lambda = 1.5405\mathring{A}$ (Cu-K_α). Apart from the very intense peak of the substrate at $2\Theta = 69.12°$, there are two peaks rising from the Fe film, corresponding to (110) and (310) orientations. The occurrence of multiple orientations gives rise to a polycrystalline character of the thin films. Moreover, by incorporating the Scherrer-Formula, from the width of the peaks the average grain size could be estimated to be in the range of $10 \pm 5\,\mathrm{nm}$.
This finding further reduces the relevance of the already small magnetocrystalline anisotropy

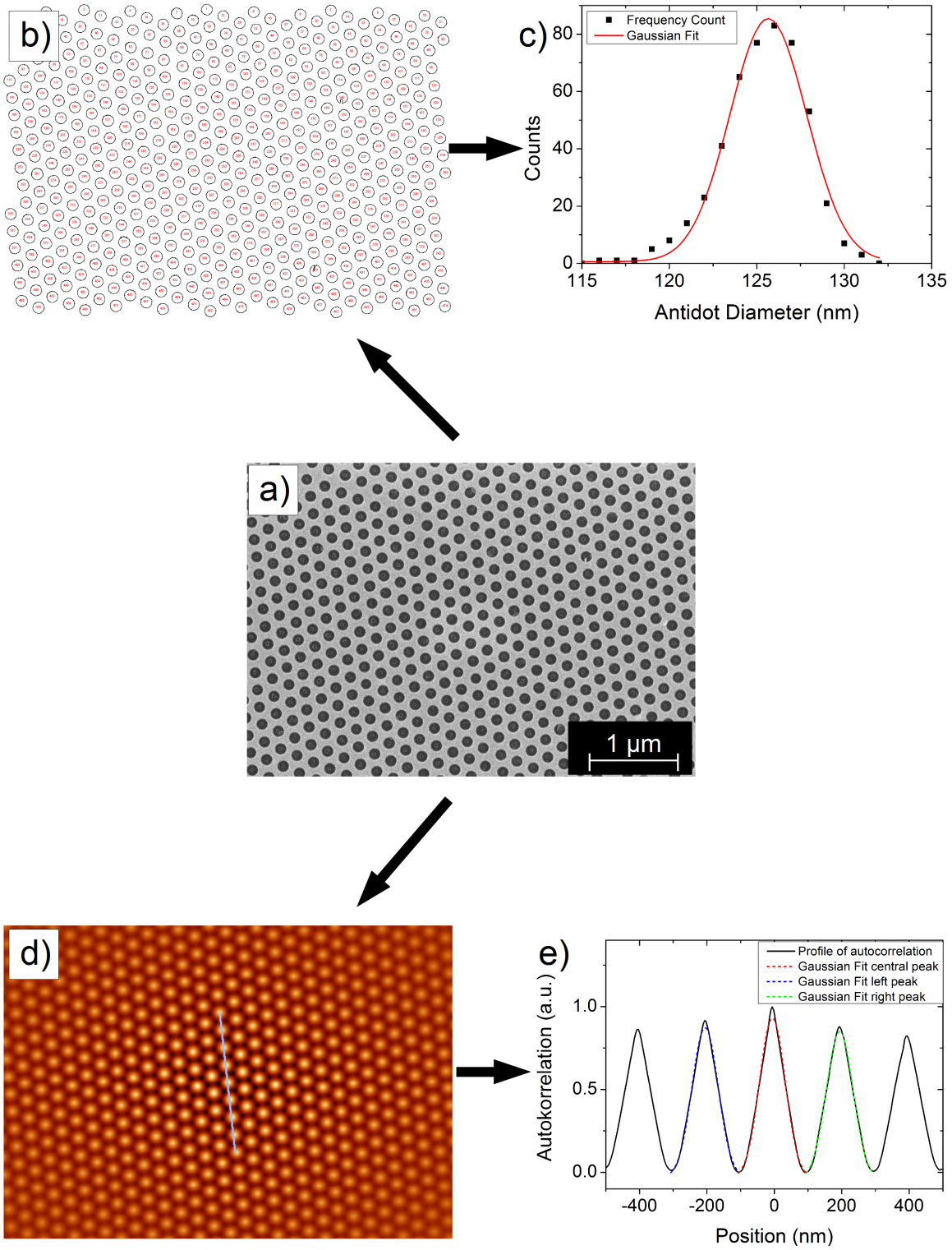

Figure 2.6: Characterization of the antidot lattice: Starting from a SEM micrograph of the antidot array (a), the holes can be recognized and analyzed by the software *ImageJ*. (b) shows the result of the software recognition. (c) shows the histogram of the measured antidot diameters, as well as a Gaussian fit: the mean diameter is $d = 125 \pm 4\,\mathrm{nm}$. (d) presents the self-correlation of the SEM micrograph in (a), and (e) shows a profile plot of the self-correlation along the blue line in (c). The distance between the peaks is a good measure for the average nearest neighbor distance in the antidot lattice, which in the example is $201 \pm 4\,\mathrm{nm}$.

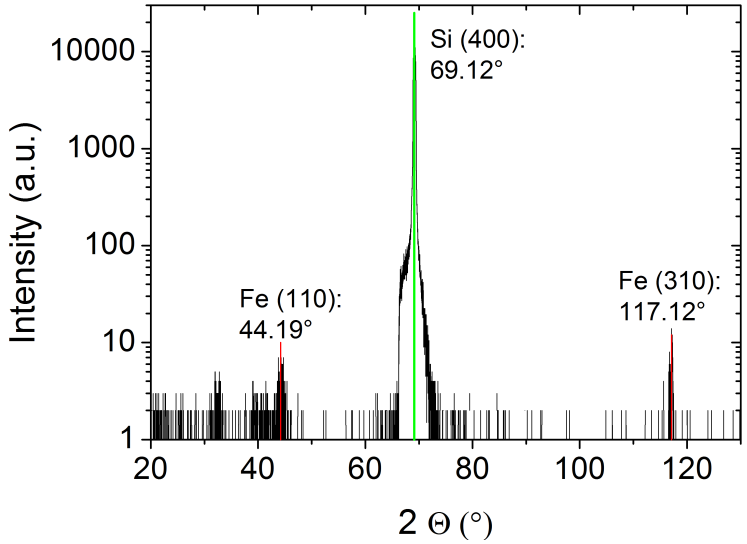

Figure 2.7: Typical X-Ray Diffractogram of an $2\,\mathrm{nm}$ Pt / $20\,\mathrm{nm}$ Fe / $300\,\mathrm{nm}$ SiO_2 / Si (100) reference sample. Apart from the intense peak rising from the Si substrate ($69.12°$), two peaks from the Fe thin film could be identified, corresponding to (110) and (310) orientations of the film. Thus, there is no hint for textural growth of the films. The average grain size could be estimated to be in the range of $10 \pm 5\,\mathrm{nm}$

in the studied antidot arrays. In Section 4.1, it will be shown that the coercivity of an antidot array can exceed the one of the respective reference film by more than one order of magnitude. Therefore, and for practical reasons, magnetocrystalline anisotropy will be neglected in most of the micromagnetic simulations. The exception to that are the simulations conducted by Kristof Lebecki, which are presented in Section 4.4.

3 Methods for Magnetic Characterization

This chapter gives an overview on the methods which were used to determine the magnetic properties of the antidot arrays. While integral measurement methods like SQUID magnetometry or magnetotransport measurements proved to be important tools for the characterization of the antidot arrays, a deeper understanding of the processes in the antidot arrays could only be achieved by means of microscopy techniques like Magnetic Force Microscopy and X-ray Microscopy. Nowadays, a well established tool in nanomagnetism are micromagnetic simulations. Careful correlation of simulated and measured data provides a thorough picture of the magnetism in the system under investigation.

3.1 SQUID Magnetometry

Most of the hysteresis loops presented in this thesis were measured with a Quantum Design MPMS Superconducting Quantum Interference Device (SQUID) magnetometer. The device is equipped with the so called Reciprocating Sample Option (RSO). This technique makes use of a servo motor to oscillate the sample through the device's pick up coils and can measure the sample's magnetic moment with a intrinsic sensitivity of $5 \times 10^{-12}\,\mathrm{Am}^2$ [83]. The samples investigated in this work had a magnetic moment in the order of $10^{-7}\,\mathrm{Am}^2$ in saturation, which could be measured with a standard deviation smaller than 1.5%.

Furthermore, magnetic fields up to $50\,\mathrm{kOe}$ can be applied to the sample by means of a superconductive solenoid, while the field can be changed in steps of $\Delta H = 0.1\,\mathrm{Oe}$. The field is determined by the calibrated current provided by the power supply unit. In interplay with the flux pinning of the superconductive coils, this can lead to problems when operating the device at small fields, i.e. fields below $100\,\mathrm{Oe}$: the flux pinning causes a remnant field created by the coils of which the device is not aware of. This remnant field can be up to $40\,\mathrm{Oe}$ and depends on the field's history [84]. Especially when characterizing soft magnetic samples like the non-structured reference films in this thesis, one should be aware of this issue. It can be circumvented by quenching the coils and avoid the application of very large fields prior to investigating soft magnetic samples. A very comprehensive work on the device can be found in reference [85].

Another important feature of the SQUID magnetometer is its liquid helium based temperature regulation system which achieves stable sample temperatures between 2 and $400\,\mathrm{K}$. For this work, especially the possibility to measure at very low temperatures was of interest, as it allows to mimic the conditions in the micromagnetic simulations which in general neglect any temperature effects, i.e. models the physics at $T = 0\,\mathrm{K}$.

3.2 Magnetotransport Measurements

The anisotropic magnetoresistive (AMR) effect allows to probe a ferromagnet's magnetization by a simple resistance measurement (see equation 1.11). Similar to techniques like SQUID magnetometry, the magnetic field is swept along a defined direction in a magnetotransport experiment. Then, after each change of the magnetic field, the electrical resistance $R(H)$ of the sample is measured.

3.2.1 Setup for Magnetotransport Measurement

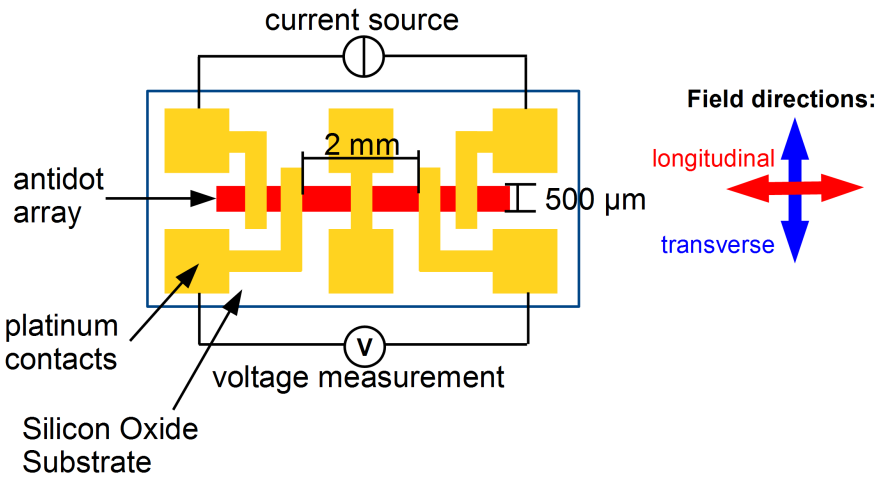

Figure 3.1: Sample layout for AMR measurements: The actual antidot array extends only to the $6 \times 0.5\,\mathrm{mm}^2$ large, red colored region in the center of the sample chip. The $50\,\mathrm{nm}$ thick Platinum contacts are connected in a 4-point measurement geometry. The two contacts in the center of the sample are not connected at this stage, but will play a role in Section 4.4. The cross defines the two distinguished field orientations in AMR measurements: "longitudinal" with the field applied parallel to the net current direction, and transverse, with the field perpendicular (but still in-plane) to the net current direction.

Magneto-resistance measurements were carried out using the sample setup depicted in Figure 3.1: For resistance measurements the substrate needs to be electrically insulating,

thus $SiO_2(300\,\mathrm{nm})$/Si(001) was chosen. The whole sample chip has a length of $5 \times 10\,\mathrm{mm}^2$ to fit into the sample holder of the measurement setup.
After colloidal self-assembly the samples are exposed to an oxygen plasma for a suitable amount of time to achieve the desired sphere diameter (see Section 2.1 for more details). On top of these templates $20\,\mathrm{nm}$ thick Fe films together with a $2\,\mathrm{nm}$ Pt capping layer were grown through a rectangular mask by pulsed laser deposition. Subsequently, PS spheres together with their magnetic caps were removed by chemo-mechanical polishing. The self assembly is very critical: if the polystyrene spheres form a multilayer in the area on which the film is deposited, the film would be interrupted, making a transport measurement pointless. The resulting antidot sample has a length of $6\,\mathrm{mm}$ and a width of $0.5\,\mathrm{mm}$ (red bar in Figure 3.1). Finally, additional Pt contacts ($50\,\mathrm{nm}$) are deposited by PLD for transport measurements (yellow pads in the Figure).

Magneto-resistance measurements were then performed using a Keithley 6221 as a DC current source, applying a maximum probing current of $10\,\mu\mathrm{A}$, and a Keithley 2000 digital multimeter as sketched in Figure 3.1 for voltage measurement in a 4-point measurement geometry. Temperature stability is provided by using a liquid nitrogen bath cryostat ($T = 77\,\mathrm{K}$). This is necessary as the AMR effect in the Fe antidot arrays is small ($\Delta R/R_0 = 0.1\%$), thus even minor changes in temperature would obscure the desired signal. The setup is capable of magnetic fields up to $5000\,\mathrm{Oe}$ applied in any direction with respect to the sample. The magnetic field is provided by a Bruker Type B-E 10 electromagnet. A Labview program has been written to automatize the whole measurement process and data acquisition.

3.2.2 Interpretation of AMR measurements

Typically, one distinguishes between two measurement geometries: In the longitudinal setup, field and current are (anti-)parallel to each other, while in the transverse case they are oriented perpendicular to each other, as illustrated in Figure 3.2. Each geometry leads to a characteristic curve. This is illustrated in Figure 3.2 a) for the example of a $20\,\mathrm{nm}$ thick, polycrystalline Fe film on a Silicon Oxide substrate, measured with the setup as described above. In Section 4.3 it will be discussed how the presence of the antidots alters the magnetotransport behavior.

Saturating the sample in longitudinal geometry (state L1) results in a maximum resistance configuration, as all magnetic moments are aligned with the current direction (see Figure 3.2 b)). Upon reducing the field, the resistance starts to decrease and eventually reaches

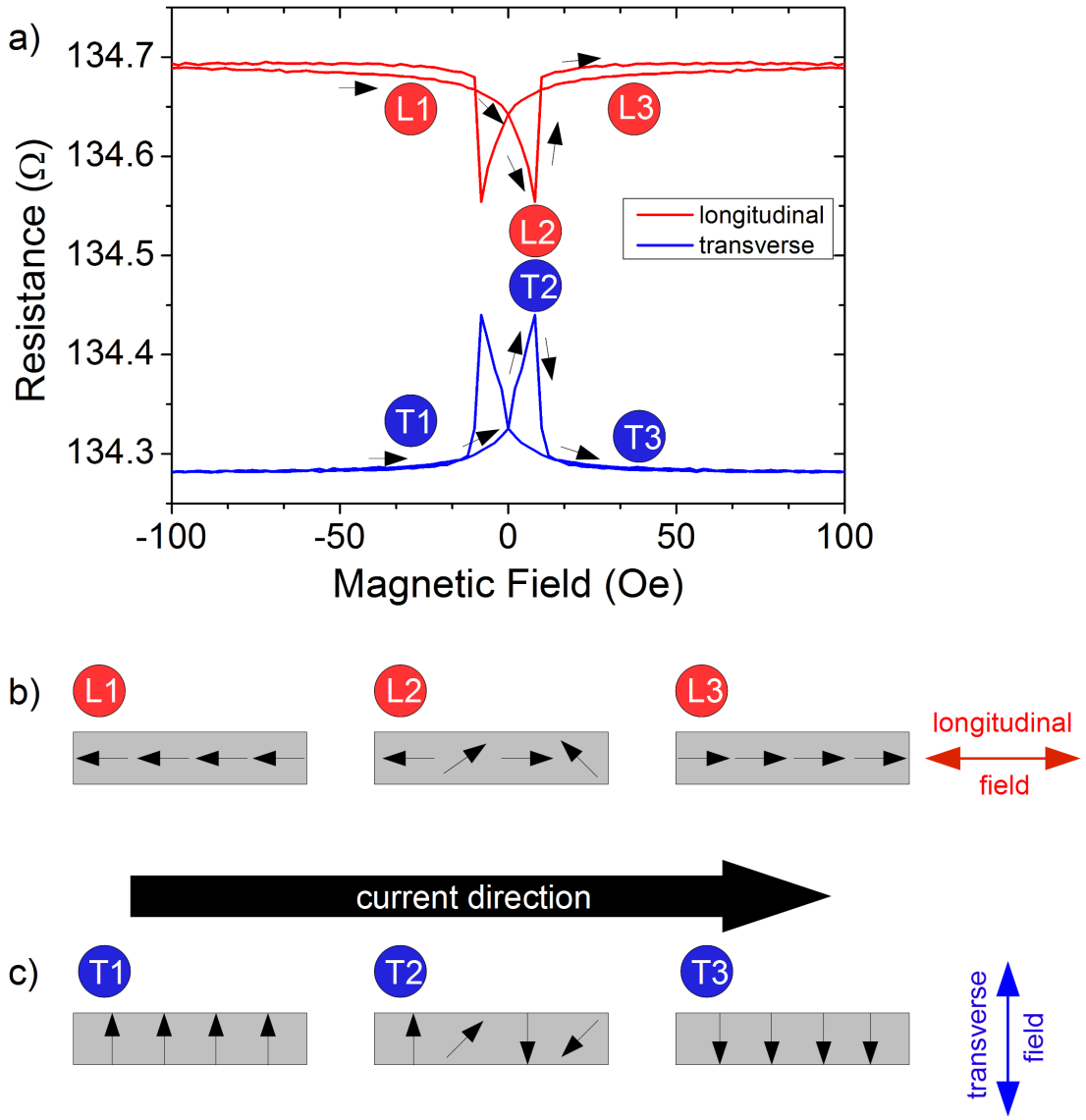

Figure 3.2: a) Magnetotransport curves measured on a $20\,\mathrm{nm}$ thick Fe film, in both longitudinal and transverse field configuration. b) and c) show schematics of possible domain configurations within the film (black arrows in gray rectangle) for negative saturation (L1, T1), at the coercivity (L2, T2) and at positive saturation (L3, T3) for longitudinal and transverse geometry, respectively.

a minimum. This drop in resistance can be attributed to the formation of domains with a magnetization which is not aligned with the field (and thus, current) anymore. At the coercive field, where the overall magnetization's projection on the field axis is zero, the average angle between field and magnetization is maximized (state L2). Therefore, the minimum in the longitudinal AMR signal is a good measure for the coercive field [86, 87, 88]. Further increase of the counter field finalizes the magnetization reversal. Due to the $\cos^2\alpha$ dependence of AMR, the same resistance is attained for both directions of the saturation. This is also the reason for the symmetry of the plot with respect to $H = 0$, when

the field is swept back to its original direction, i.e. after the sample has undergone a full hysteresis loop.

In the transverse case, the sample's magnetization is saturated perpendicular to the current direction for high magnetic fields (state T1). Therefore, the resistance acquires its absolute minimum. At the coercive field (L2), in analogy to the longitudinal case, the average angle between the magnetization and the magnetic field is maximized. In turn, this results in a minimal angle between magnetization and current, and, thus in an increase in resistance as compared to transverse saturation.

From the fact that there is a difference in resistance at the coercive field for longitudinal and transverse geometry (L2 vs. T2), it can be deduced that the magnetization is not completely random even in the polycrystalline Fe film, but has memory of the direction of the saturating field. However, the polycrystalline nature of the film reflects in the maximum values of $\Delta\rho/\rho(H=0)$, which for both longitudinal and transverse case is 0.12%.

3.3 Magnetic Force Microscopy

Magnetic Force Microscopy (MFM) is a well established technique for imaging of magnetic fields on the nanoscale. In turn, knowledge of the sample's magnetic stray field allows to draw conclusions of the sample's magnetization configuration $\vec{M}(\vec{r})$. After the development of the Atomic Force Microscope (AFM) [89] the step towards Magnetic Force Microscopy was straight forward. Atomic Force Microscopes use a sharp Silicon tip which is mounted on a so-called cantilever to raster-scan the sample's surface by means of extremely precise Piezo actuation. The sharp tip enables the microscope to map the surface topography of the sample with a resolution of typically a few nanometers laterally and way below one nanometer vertically. Therefore, the forces acting between surface and tip are detected. In MFM, the diamagnetic Silicon tip is replaced by a tip with a ferromagnetic thin film coating which results in a considerable magnetostatic interaction with the stray field $\vec{H}_{stray}(\vec{r})$ of the sample [90]. In this chapter, the fundamentals of MFM will be presented, with a focus on the formation of the detected magnetic signal and image interpretation.

3.3.1 Non-Contact Force Microscopy

A main goal in Magnetic Force Microscopy is to exclusively record the magnetostatic interaction between tip and sample. This cannot be achieved when the tip is in mechanical contact with the sample, mainly due to the very strong repulsive interaction caused by Pauli's exclusion principle, but also by the Van-der-Waals interaction and capillary forces when the

measurement is conducted under ambient conditions. However, all the above mentioned forces decay very rapidly with increasing distance, while the magnetostatic dipole-dipole interaction ranges further [91]. These facts dictate that the tip is to be withdrawn from the surface by a distance of typically several $10\,\mathrm{nm}$. The distance control is hereby achieved by use of the plane-fit mode: In a first scan, the sample's topography is recorded. A plane is then fitted to the topography. The tip is then retracted from the sample surface by a certain distance, the so-called lift height, and scans the sample within a plane parallel to the calculated one. The scan routine is depicted in Figure 3.3.
Such non-contact force measurements are usually performed in the so called dynamic operation mode, in which the cantilever is excited to oscillate with its resonance frequency ω_0 and forces, or, more precisely: force gradients, are detected by changes in this resonance frequency. This stands in contrast to the conventional AFM operation mode, in which the much stronger forces which occur when the tip and sample are in mechanical contact are detected by measuring the deflection of the cantilever.

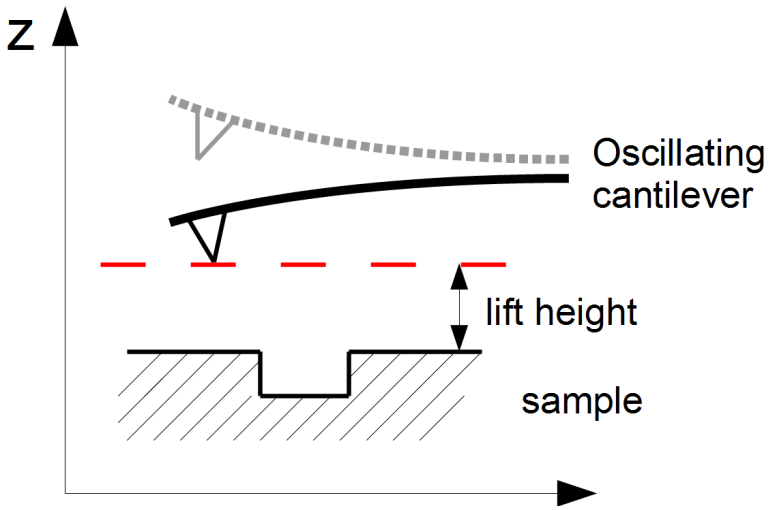

Figure 3.3: Plane-Fit-Mode in MFM: A plane is fitted to the topography of the sample surface, which is measured in an initial scan. For a second scan of the same sample section, in which the long range forces are measured, the tip is retracted by the lift height and follows a plane parallel to the previously calculated one (dashed red line).

The cantilever can be regarded as a harmonic oscillator, as its oscillation amplitude is usually kept small (in the order of 10 - $20\,\mathrm{nm}$) compared to its length (approximately $200\,\mu\mathrm{m}$. Its eigenfrequency is then given by:

$$\omega_0 = \sqrt{\frac{k_c}{m_{eff}}} \tag{3.1}$$

Here, k_c is the spring constant of the cantilever and m_{eff} is its effective mass. Typical eigenfrequencies are in the range of $100\,\mathrm{kHz}$. As mentioned, in non-contact mode the cantilever is excited to oscillate. This is usually realized by means of an extra Piezo actuator at the clamped side of the cantilever. If this actuator oscillates sinusoidally with amplitude z_a and angular frequency ω, the tip on the other side of the cantilever will follow with a certain amplitude z_{tip} and a phase shift Φ, both depend on the damping constant γ of the cantilever's oscillation. In non-contact force-microscopy, the influence of the external forces on this driven and damped oscillation are detected. Let z be the distance between tip and sample and z_0 the equilibrium distance, then the equation of motion reads [92]:

$$\frac{\partial^2 z}{\partial t^2} + \frac{\omega_0}{Q}\frac{\partial z}{\partial t} + \omega_0^2(z - z_0) = z_a\omega_0 \cos\omega t \tag{3.2}$$

, where the quality factor Q is given by

$$Q = \frac{m_{eff}\omega_0}{2\gamma}. \tag{3.3}$$

The equation of motion 3.2 has the solution

$$z(t) = z_0 + z_{tip}\cos(\omega t + \Phi) \tag{3.4}$$

, while the amplitude z_{tip} is determined by

$$z_{tip}(\omega) = \frac{z_a\omega_0^2}{\sqrt{(\omega_0^2 - \omega^2)^2 + 4\gamma^2\omega^2}} \tag{3.5}$$

and the phase shift reads

$$\phi = \arctan\frac{2\gamma\omega}{\omega^2 - \omega_0^2}. \tag{3.6}$$

So far, no tip-sample interaction had been considered. Adding a force $F(z)$, which shall exclusively act in the z-direction, the equation of motion 3.2 becomes:

$$\frac{F(z)}{m} + \frac{\partial^2 z}{\partial t^2} + \frac{\omega_0}{Q}\frac{\partial z}{\partial t} + \omega_0^2(z - z_0) = z_a\omega_0 \cos\omega t \tag{3.7}$$

In order to determine the response of the cantilever to the external force $F(z)$, this force is usually approximated by a first order Taylor series expansion, which delivers accurate results whenever the derivative of the force $\frac{\partial F}{\partial z}$ does not change significantly over the whole range of the cantilever's oscillation $2z_{tip}$. In this case the external force' gradient is simply subtracted from the cantilever's spring constant, resulting in a new effective spring

constant:

$$k_{eff} = k_C - \frac{\partial F}{\partial z} \tag{3.8}$$

The new resonant frequency of the cantilever is then:

$$\omega_F = \omega_0 \sqrt{1 - \frac{1}{k_C}\frac{\partial F}{\partial z}} \tag{3.9}$$

Or, in terms of a frequency shift for $\frac{\partial F}{\partial z} << k_C$:

$$\Delta\omega = \omega_F - \omega_0 = -\omega_0 \frac{1}{2k_C}\frac{\partial F}{\partial z} \tag{3.10}$$

The frequency shift $\Delta\omega$ can be directly measured if a phase locked loop (PLL) is used for the actuation of the cantilever [93]. This approach is also used for the magnetic force microscope employed for the investigation of the antidot samples. In the MFM images, each pixel is assigned a gray value according to the frequency shift measured at the respective sample coordinate. Pixels with a increased resonant frequency, i.e. a positive frequency shift, appear bright while a dark pixel stands for a lowered resonant frequency. Under the assumption that the magnitude of the force between tip and sample $|F(z)|$ decreases with increasing tip-sample distance, it is possible to distinguish between attractive and repulsive forces. While for the former the gradient $\frac{\partial F}{\partial z}$ is negative and corresponding sample positions appear bright, the opposite is true for attractive forces.

3.3.2 Formation of Magnetic Contrast

The magnetic tip interacts with the sample via dipole-dipole interaction. The magnetic stray field, which a ferromagnetic sample produces, is according to Ref. [22] connected to the sample magnetization $\vec{M}_{Sa}$ by:

$$\vec{H}_{stray} = \int\limits_{V_S} -\operatorname{div} \vec{M}_{Sa}(\vec{r}')\frac{\vec{R}}{|\vec{R}|^3}\,\mathrm{d}\,V' + \int\limits_{A_S} \vec{n}\cdot\vec{M}_{Sa}(\vec{r}')\frac{\vec{R}}{|\vec{R}|^3}\,\mathrm{d}\,A' \tag{3.11}$$

The first integration extends over the sample volume, the second over its surface with $\vec{n}$ being the corresponding normal vector and $\vec{R} = \vec{r} - \vec{r}'$. With their R^{-2} distance dependencies, the two integrands resemble Coulombs law. The parallels to electrical charge become especially clear when one defines the magnetic volume charge density

$$\rho_V(\vec{r}) = -\operatorname{div} \vec{M}_{Sa}(\vec{r}) \tag{3.12}$$

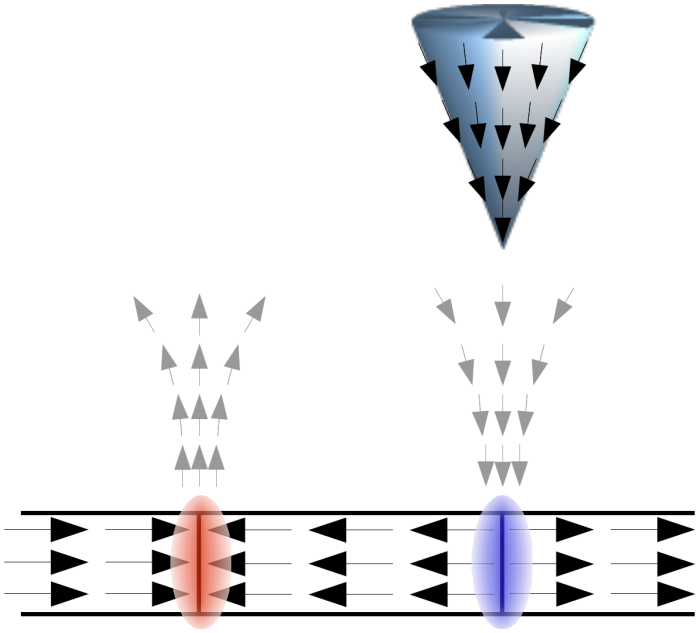

Figure 3.4: Magnetic volume charges arise on the transitions between adjacent domains. These charges are the sources of the stray field. Dependent on the magnetization direction of the tip, the tip-sample interaction is attractive or repulsive.

and the surface charge density

$$\rho_S(\vec{r}) = \vec{n} \cdot \vec{M}_{Sa}(\vec{r}'). \tag{3.13}$$

These charges are the sources of the stray field. The formation of volume charges in an in-plane magnetized sample is illustrated in Figure 3.4: wherever the direction of the magnetization changes, i.e. div$\vec{M} \neq 0$, charges arise. The sign of the charge attributed to a volume element is determined by whether more magnetic moments on its surface point into or out of it, symbolized by the blue and red charge clouds in the Figure.

The MFM tip has a ferromagnetic thin film coating. Due to shape anisotropy, the magnetization aligns within the plane of this film, as sketched in Figure 3.4. The z-component of the force, which the sample's stray field exerts on the tip, is

$$F_z = \int V_T \frac{\partial}{\partial z} \vec{M}_T(\vec{r}') \cdot \vec{H}_{stray}(\vec{r}') \, \mathrm{d}\, V' \tag{3.14}$$

, which yields for the shift of the resonance frequency of the cantilever (see equation 3.10):

$$\Delta\omega = -\omega_0 \frac{1}{2k_C} \int V_T \frac{\partial^2}{\partial z^2} \vec{M}_T(\vec{r}') \cdot \vec{H}_{stray}(\vec{r}') \, \mathrm{d}\, V' \tag{3.15}$$

As the exact magnetization $\vec{M}_T$ of a MFM tip is unknown, assumptions have to be made. A very popular model [94] is to combine the whole magnetization into a single dipole moment

$\vec{m}$, which is situated somewhere in the tip and oriented along the z-axis, i.e. normal to the sample surface. The formula for the frequency shift then reduces to:

$$\Delta\omega = -\omega_0 \frac{1}{2k_C} m_z \frac{\partial^2 H_{stray,z}}{\partial z^2} \tag{3.16}$$

However, the model is quantitatively only applicable when the lateral dimensions of the investigated structures are of the same order of magnitude as the length of the tip [95, 96], which is some microns.

More sophisticated models use extended, but idealized charge distributions. Very good quantitative results have recently been achieved by modeling the tip as a cone whose surface is populated with magnetic moments pointing towards it the tips apex [97].

3.3.3 Experimental Setup

The MFM images in this thesis were recorded with a custom made MFM, which is initially designed by Rainer Kümmel [98] and Berndt Koslowski and improved in the course of many thesis works [99, 100] by Hartmut Straub, Thomas Haebele and myself. The microscope uses a PLL to actuate the cantilever and to detect the resonance frequency shift. Recently, Steffen Nothelfer designed an electro magnet which is capable of in-plane fields of up to $1000\,\mathrm{Oe}$ at a yoke size of $2\,\mathrm{mm}$ [101]. Commercial Bruker MESP tips were used for all the presented images.

3.4 X-ray Magnetic Circular Dichroism (XMCD) based microscopy techniques

The absorption of X-rays in matter is governed Lambert-Beer's Law:

$$I(x) = I_0 e^{-\alpha(E)\cdot x} \tag{3.17}$$

, where $\alpha(E)$ is the energy dependent absorption coefficient. For the absorption of circularly polarized x-rays in a ferromagnet, the so called X-Ray Magnetic Circular Dichroism (XMCD) causes an additional dependence of the absorption coefficient on the angle between a samples magnetization $\vec{M}$ and the helicity of these x-rays. When we define the absorption coefficients for left and right circular polarized light as α^+ and α^-, respectively,

the relative absorption contrast $c(E)$ due to XMCD reads:

$$c(E) = \frac{\alpha^+ - \alpha^-}{\frac{1}{2}(\alpha^+ + \alpha^-)}(E) \tag{3.18}$$

The contrast $c(E)$ depends on the magnetization as follows:

$$c(E) \propto \frac{\vec{M} \cdot \vec{e}}{|\vec{M}|} P_C \tag{3.19}$$

, where $\vec{e} = \frac{\vec{k}}{|\vec{k}|}$ is the normalized wave vector of the light and P_C its degree of polarization [102]. This directional dependence can be used by x-ray microscopy methods to image the magnetization.

For a XMCD based analysis of transition metals, usually X-ray energies in the range from $700\,\mathrm{eV} - 950\,\mathrm{eV}$ are used, corresponding to electron transitions from $2p_{1/2}$ and $2p_{3/2}$ core states into unfilled states in the $3d$ band. The resonant absorption at these so-called L_2- and L_3-edges yields the strongest XMCD contrast. The helicity of the light determines the angular momentum of the photons, which can attain values of $\pm\hbar$. This angular momentum is transferred to the $2p$ electron, resulting in photo electrons of opposite spin for the two cases. Spin flips are forbidden in electric dipole transitions, so that spin-up (spin-down) photoelectrons from the p state can only be excited into unoccupied spin-up (spin-down) states [103]. On the other hand, the density of states around the Fermi level, and therefore the amount of unoccupied states, is spin dependent in a ferromagnet. It is this asymmetry which is reflected in the XMCD contrast between left and right circular polarized light: the more unoccupied states are compatible with the excitation of the photoelectron, the larger the absorption for a given helicity.

3.4.1 Scanning Transmission X-Ray Microscopy (STXM)

Scanning Transmission X-Ray Microscopy locally probes the absorption of a sample by means of a focused, monochromatic light beam. This is achieved by transmitting the beam through the sample and measure the intensity of the transmitted light. Apart from many other applications, the technique can make use of the XMCD effect and thus image the magnetization with a lateral resolution of $25\,\mathrm{nm}$. In order for the samples to be sufficiently transparent to the soft x-ray light, they have to be thin. The antidot samples thus have been prepared on commercial Silicon Nitride nanomemberane windows with a thickness of $500\,\mathrm{nm}$ (see Chapter 2 for more details).
According to formula 3.19, the XMCD contrast is proportional to the projection of the magnetization on the wave-vector of the light. This implies that for in-plane magnetized sam-

ples one can only observe XMCD when the incidence of the light is not perpendicular to the sample surface. In practice, the sample is therefore tilted by 30° with respect to the normal incidence.
The images presented in Section 4.1 were recorded at the MAXYMUS X-ray Microscopy, which is attached to the UE46-PGM2 beam line of the BESSY II synchrotron light source in Berlin. The instrument allows application of magnetic fields of up to $2400\,\mathrm{Oe}$. A more detailed description of the setup can be found in References [104, 105].

3.4.2 X-ray Photo Emission Electron Microscopy (X-PEEM)

Each photo electron which is excited due to the absorption of the soft x-rays leaves an empty state in the atomic cores. As this vacancy is filled by electrons from energetically higher states, secondary electrons are created, for example due to the Auger effect or inelastic electron scattering. Some of these electrons can escape from the sample. Their number is proportional to the amount of absorbed photons which in turn can depend on the XMCD effect.

A photo emission electron microscope images the spatial distribution of these electrons. In contrast to STXM, PEEM is a full field technique: the sample region of interest is illuminated by monochromatic X-rays, and an electron optic is used to magnify their distribution on a detector screen. In order to provide a sufficiently long mean free path for the emitted electrons, such experiments have to be conducted under UHV conditions. A significant advantage over transmission based techniques is that there is no restriction on the sample thickness. On the other hand, as a result of the small mean free path of the secondary electrons within the emitting material, the technique is very surface sensitive with an information depth of only several nanometers [106]. Therefore, any protection layer of the sample should be as thin as possible. A more comprehensive description of the technique can be found in Reference [107].

The microscope used for the experiments presented in Section 4.5 is a commercial SPECS P90 AC LEEM/PEEM, using light from the UE49-PGM beam line at the BESSY II synchrotron in Berlin. The sample was mounted on a sample holder which includes an electromagnet capable of in-plane fields up to $500\,\mathrm{Oe}$. However, imaging with applied fields reduces the resolution as the electrons get deflected by the Lorentz force. The presented images were therefore recorded in remanent state after the respective field was applied. In order to isolate the XMCD-contrast from topographic contrast, after each field step an image with each left- and right circularly polarized light is recorded. Subsequently, there intensity values were divided by each other, giving rise to so-called XMCD images.

3.5 Finite Element Micromagnetic Simulations

Micromagnetic simulations provide detailed insight into the magnetization behavior of a system. There are several software solutions freely available. They have a common physical foundation, which is the Landau-Lifshitz-Gilbert equation [108, 109]:

$$\frac{d\vec{M}}{dt} = -|\gamma|\vec{M} \times \vec{H}_{eff} - \frac{|\gamma|\alpha}{M_S}\vec{M} \times \frac{d\vec{M}}{dt} \tag{3.20}$$

, with $\gamma = 1.76 \cdot 10^{11}\,\mathrm{Hz/T}$ being the gyromagnetic ratio and α the material specific, dimensionless Gilbert-damping parameter. By integration of this differential equation, the time evolution of the local magnetization vector can be calculated. The first term of equation 3.20 expresses the torque which the effective field $\vec{H}_{eff}$ exerts on the magnetization $\vec{M}$, resulting in a precession of $\vec{M}$. The precession does not continue indefinitely, but is damped by interaction of the magnetization with the crystal lattice. This is summarized in the second term.

This micromagnetic approach, which models the magnet material as a continuum, yields a very good description of the magnetization as long as the characteristic length scales of the modeled geometry are large compared to interatomic distances.

Complexity and necessity for computational power arise from the extended geometry of the simulated system, which reflects in the calculation of the effective field. This field comprises not only the actual magnetic fields, i.e. the externally applied field $\vec{H}_{ext}$ and the demagnetization field $\vec{H}_{demag}$, but also includes contributions from exchange interaction and magnetocrystalline anisotropy, which are also modeled in terms of the magnetic fields $\vec{H}_{exch}$ and $\vec{H}_{aniso}$. The latter three fields all depend on the exact magnetization configuration of the whole simulated geometry. Therefore, the differential equation for a given position $\vec{r}_i$ is coupled to the equations for every other position within the geometry.

In order to calculate aforementioned contributions to the effective field, the simulation software requires input of material specific parameters. These are the saturation magnetization M_s, the exchange constant A, the damping constant α and uni-axial or cubic anisotropy constants. Due to the combination of the polycrystalline character of the thin films (see Section 2.3) and their comparatively small magnetocrystalline anisotropy, the anisotropy constants have been set to 0.
Realistic values of the damping parameter α, for example for polycrystalline Fe films, are in the order of 0.0075 [110]. With these small values, the calculation of a stable magnetization state takes extremely long. To reduce simulation time, a value of $\alpha = 0.5$ was used, which

is a common practice.
The values for M_S and A for the relevant materials can be found in table 4.1.

For the numerical time integration of the coupled differential equations, the simulated geometry has to be discretized. There are two principal approaches: The finite difference (FD) method which is used by the widely-used *OOMMF* simulation package [112], and the finite element method (FE) which is used for example by the packages *NMag* [113] and *Magpar* [114]. FD segments a given geometry into rectangular prisms of equal size. The differential equation is only solved for the centers of the prisms, while the values for the rest of the sample are interpolated. FE on the other hand discretizes the sample into a mesh of tetrahedra and solves the differential equation for the nodes of this mesh.

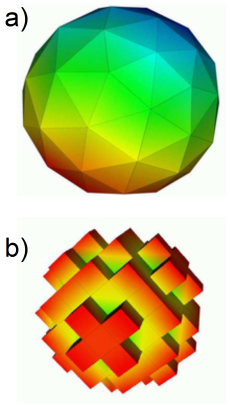

Figure 3.5: A sphere discretized into (a) tetrahedra and (b) prisms [111].

The FE approach has one significant advantage over FD: Geometries involving a curvature can be modeled more efficiently. This is illustrated in Figure 3.5, where the discretization of a sphere based on FE and FD is compared. Both structures consist of approximately the same amount of elements. Usage of the FD method results in a much coarser surface, which then would lead to a strong alteration of the demagnetizing field. This could only be circumvented by using a much finer discretization, which in turn increases the computational time.
For this reason, most of the simulations presented in this thesis were carried out using the FE-based software package *NMag*. This allowed accurate simulations without constant access to larger computer clusters. The only exception to that are the *OOMMF*-based simulations from Prof. Nowak's group which are presented in Section 4.4.

A typical antidot geometry as used for the *NMag* simulations is shown in Figure 3.6. It includes 33 complete holes, the antidot lattice constant is $a = 200\,\mathrm{nm}$ and the Gaussian distributed hole diameter $d = 170 \pm 4\,\mathrm{nm}$. Compared to the experiments of chapter 4, where the film thickness was $20\,\mathrm{nm}$ in most cases, this was reduced $t = 5\,\mathrm{nm}$ for almost all simulations in order to reduce computational time. The effect of this reduction will be discussed towards the end of this section.
It is important to choose a sufficiently large geometry, as otherwise the strong demagnetizing fields at the sharp edges influence the magnetization reversal [115] to a disproportionally high degree. The depicted geometry was created using the freely available software *Netgen* [116]. In the next step, the geometry is discretized into tetrahedra, which

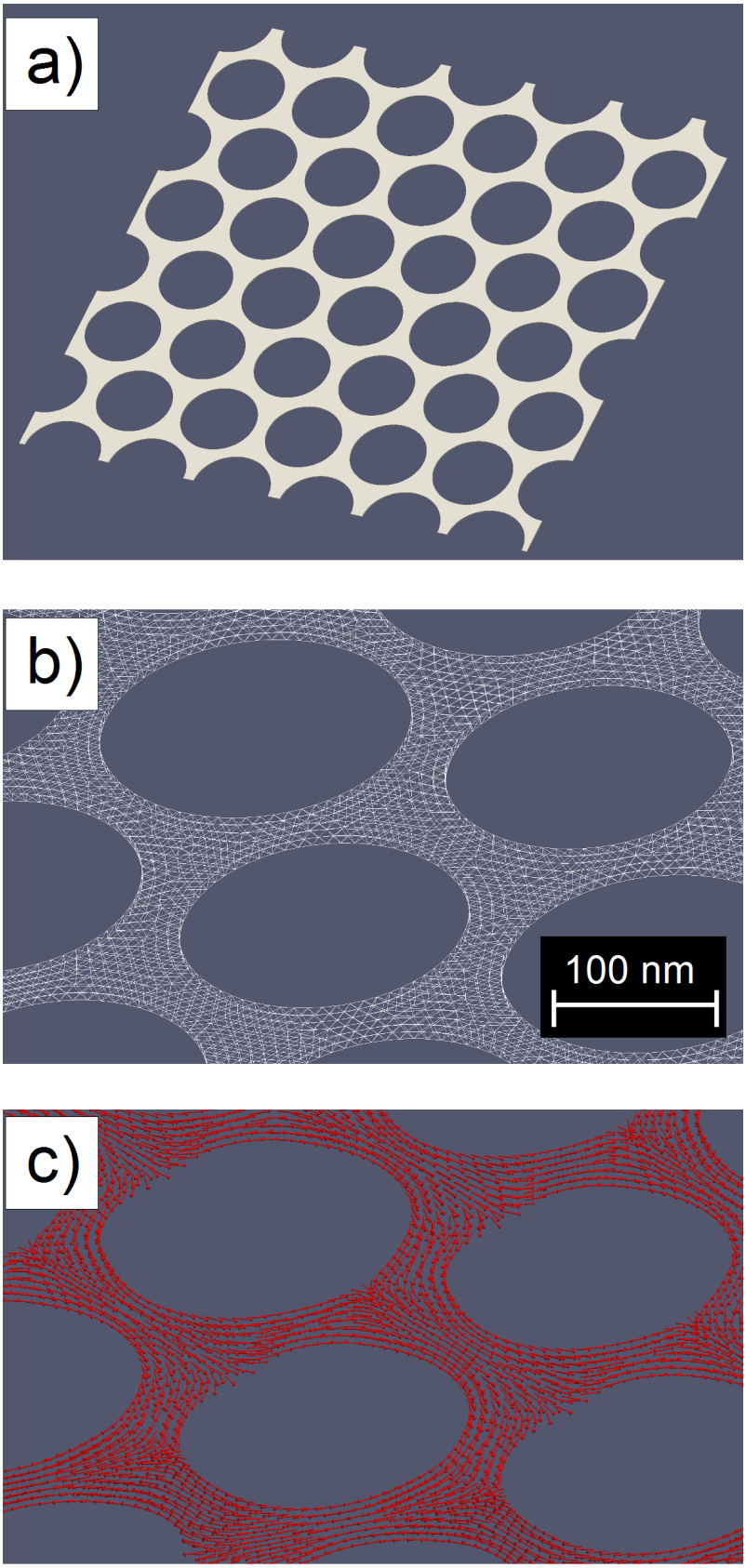

Figure 3.6: Micromagnetic simulations: (a) Example of a simulation geometry, consisting of 33 complete holes. (b) Mesh of tetrahedra which the software *Netgen* generated from the geometry. (c) The simulation software *Nmag* populates every node of the mesh with a magnetization vector.

is also performed using *Netgen*. The result is shown in Figure 3.6 b). With the whole mesh consisting of 51000 tetrahedra, it is fine enough to conserve the curvature of the holes.

The mesh is then imported into *NMag*. The simulation software calculates the time evolution for a given initial magnetization configuration and external field until the time derivative of the magnetization $|\frac{d\vec{M}}{dt}|$ is below a certain threshold, i.e. until the magnetization is stable. During simulation of a hysteresis loop, this step is repeated for each applied field, with the last stable condition being the starting point for the new relaxation.

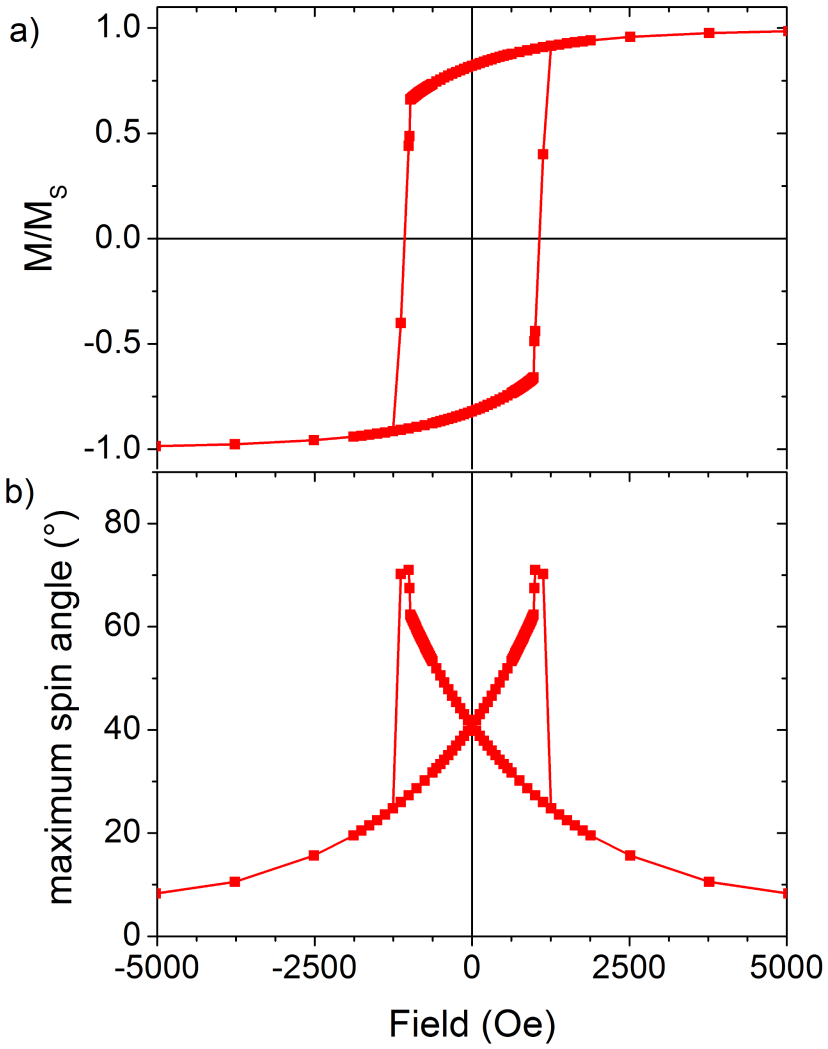

Figure 3.7: (a) simulated in-plane hysteresis loop for the antidot geometry shown in Figure 3.6. (b) Corresponding plot of the spin angle, which stays below the critical value of $90°$ during the whole magnetization reversal.

In Figure 3.7 a), such a simulated hysteresis loop is shown for aforementioned antidot geometry with the material parameters for Fe (see Table 4.1). Calculation of this loop takes roughly 20 hours on a Intel Core i5 microprocessor with $4 \times 3.6\,\mathrm{GHz}$ and $8\,\mathrm{Gigabyte}$ of RAM.

A very critical measurement for the quality of the simulated results is the so-called "'spin angle"'. This term refers to the maximum angle enclosed by any pair of neighboring spins in a given magnetization state. If the mesh is too coarse, there is a tendency to very large spin-angles up to $180°$. In such cases, the gradual rotation of the magnetization within domain walls is not resolved anymore, which leads to a severe miscalculation of all domain wall related properties [25]. Therefore, only results with a spin angle not exceeding the critical value of $90°$ were accepted [111]. In Figure 3.7 b) it is shown that this requirement is well fulfilled for the presented hysteresis loop.

The goal of a small spin angle, however, always stands in competition with the requirement of a sufficiently large sample geometry and a reasonable computation time. It turned out impossible to achieve all these requirements on the available computers. Thus, as a compromise, the film thickness of the simulated geometries was restricted to $5\,\mathrm{nm}$, although experimentally it was $20\,\mathrm{nm}$ in most cases. As shown in Figure 3.6 b), the reduced thickness results in a discretization with only one layer of tetrahedra, while usage of the realistic film thickness would quadruple this number. Apart from the computational time, memory requirements then become a bottleneck.
The smaller film thickness increases the shape anisotropy which aligns the magnetization parallel to the film plane. On small test meshes, just large enough so that the characteristic remanent domain patterns (see Section 4.2) of the antidot arrays arise, the effect of the different film thicknesses could be investigated without sacrificing the spin-angle criteria. Qualitatively, a change of thickness from $20\,\mathrm{nm}$ to $5\,\mathrm{nm}$ did not yield a difference in the magnetization patterns. However, the larger film thickness results in a larger maximum out-of-plane magnetization component. While for $t = 5\,\mathrm{nm}$ the maximum angle which the magnetization encloses with the film plane is less than $3°$, this value increases to $7°$ for $t = 20\,\mathrm{nm}$. The result implies that the torque which an in-plane field exerts on the magnetic moments is larger in the case of thicker films, which in turn could facilitate the magnetization reversal. Nevertheless, the approach is justified by the qualitative agreement of the resulting magnetization patterns for both tested thicknesses. Furthermore, as will be shown in Chapter 4, experimental and simulated data fit well together.

4 Magnetic Characterization of Self-Assembled Antidot Arrays

This chapter aims to deliver a detailed understanding of how the presence of the antidots alters the magnetic properties of soft magnetic Iron, Cobalt or Permalloy thin films. The antidots are often suspected to act as domain wall pinning sites, strongly altering the magnetization reversal of the films [117, 118]. This aspect will be investigated at the beginning of the chapter by means of SQUID magnetometry. The efficient self-assembly approach for the sample preparation hereby allows to systematically investigate a large amount of samples with varied geometric parameters, which allows further insights into the underlying mechanisms.

The nanoscaled holes are reported to greatly alter the shape anisotropy of the thin films and force the magnetization to align accordingly [5]. Magnetic Force Microscopy (MFM) proved to be an ideal tool to investigate these intrinsic domain patterns. The results are presented in section 4.2 of this chapter. Based on the results from the geometry dependent, integral characterization, it will be investigated to which degree these domain patterns can be influenced. In this context, an analogy to artificial spin-ice systems [12, 14, 119] is discussed. Furthermore, the observed domain patterns give a first hint towards the emergence of an in-plane anisotropy with respect to the hexagonal antidot lattice.

As an alternative characterization method, magnetotransport measurements on antidot arrays with various geometric parameters were performed. The dominant effect during the magnetization reversal of ferromagnetic thin films is anisotropic magnetoresistance (AMR). It was of interest on how the nanostructures influence AMR responses, as not only the magnetization is altered by their presence, but also the current density distribution becomes inhomogeneous. These aspects are discussed in section 4.3.

A drawback in the self-assembly approach is the lack of a long range order over a whole substrate with a size of several square millimeters. In a SQUID magnetometry- or magnetotransport experiment, the measured response is thus always an average over many antidot lattice directions. In section 4.4, alterations to the previously integral magnetotransport technique are presented, which allow to study the anisotropy of the magnetization reversal quantitatively. Correlation of the magnetotransport signal with MFM measurements and micromagnetic simulations provides deep insight into the processes occurring during the

reversal in both easy- and hard-axis. These results are presented in the Sections 4.4 and 4.5 for two outstanding antidot geometries.

4.1 Integral Magnetic Properties

This section discusses results obtained mainly by SQUID magnetometry and focuses on how the presence of antidots influences the hysteresis behavior of ferromagnetic thin films. It serves as a starting point for the subsequent discussion of microscopic phenomena and mechanisms in the antidot arrays in the following sections.

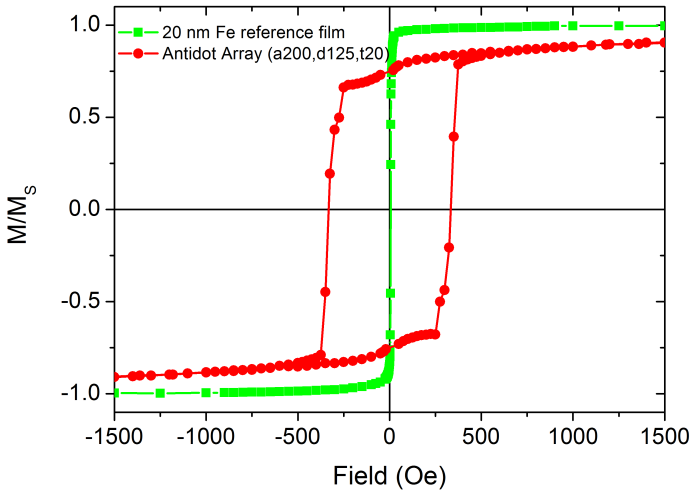

Figure 4.1: In-plane hysteresis loops of a $20\,\mathrm{nm}$ thick planar Fe reference film (green curve) and of a Fe antidot array (red curve) with antidot periodicity $a = 200\,\mathrm{nm}$, $d = 125\,\mathrm{nm}$ and film thickness $t = 20\,\mathrm{nm}$ measured at $T = 300\,\mathrm{K}$.

Figure 4.1 compares the in-plane hysteresis of a Fe antidot array (lattice parameter $a = 200\,\mathrm{nm}$, hole diameter $d = 125\,\mathrm{nm}$, film thickness $t = 20\,\mathrm{nm}$) and a planar Fe reference film, both measured at $T = 300\,\mathrm{K}$. Film deposition of both reference and antidot array sample was performed simultaneously in the PLD chamber to ensure identical conditions during film growth. Thus, any difference in the magnetic behavior can be expected to arise only due to the nanostructuring. The high remanent magnetizations for both the reference film ($M_R/M_S = 0.76$) and the antidot array ($M_R/M_S = 0.78$) indicates that their easy axes are oriented parallel to the film plane. By the end of this section, out-of-plane measurements will be presented which confirm this claim. The most obvious difference between both samples is the change in coercivity: While the Fe reference film is magnetically very soft with a coercive field of $H_C = 8\,\mathrm{Oe}$ (not resolved in Figure 4.1), the coercivity of the antidot sample is strongly enhanced to $H_C = 325\,\mathrm{Oe}$.

This gives a first hint to how the antidots act on the sample's magnetization: a higher coercivity is either caused by an increase in magnetic anisotropy or by restricting the movement of the magnetic domain walls, i.e. domain wall pinning or a combination of both effects [120]. The antidot array's hysteresis loop in Figure 4.1 could be interpreted in a way that upon applying a small counter field, an additional anisotropy caused by the nanostructures keeps the magnetization in the original direction and only a small slope in the magnetization curve is observed, indicating a reversible process. Once this anisotropy has been overcome at a field of -275 Oe, the slope drastically increases, indicating that the reversal is now driven by nucleation and movement of reversed magnetic domains, i.e. irreversible processes. This movement is hindered by domain wall pinning, as the reversal is not complete until a further increase of the counter field to $-500\,\mathrm{Oe}$.
Furthermore, the antidot sample is harder to saturate by the in-plane field as it is the case for the reference film. Changes in the antidot sample's magnetization can still be observed up to fields of $8000\,\mathrm{Oe}$, while the reference film saturates at a field of $45\,\mathrm{Oe}$. This can be regarded as further support for the hypothesis that shape anisotropy plays a significant role in the alteration of the magnetic properties: it requires rather large fields to force the magnetization to point into the holes.

These aspects will be studied in more detail in the sections 4.2 and 4.4, where microscopic techniques are applied. Furthermore, experimental evidence on the differentiation between reversible and irreversible processes will be presented. However, prior to that, the interplay of the antidot arrays' geometry and the ferromagnetic material will be investigated with regard to its influence on the hysteresis behavior. Although the easy axis of all studied antidot samples lies within the film plane, the out-of-plane magnetization is also affected by the holes. The results are presented in paragraph 4.1.3. Finally, the last paragraph of the section is dedicated to inspect the temperature dependent magnetic properties. This is critical in order to allow for comparison with micromagnetic simulations, as these in general neglect the effect of a finite temperature.

4.1.1 Interplay between magnetic material and antidot geometry

Figure 4.2 shows in-plane hysteresis loops of Fe antidot arrays which differ only in their antidot diameter, while all of them share a lattice parameter of $a = 200\,\mathrm{nm}$ and a film thickness of $t = 20\,\mathrm{nm}$. The most prominent feature here is the monotonous increase in coercivity as a function of antidot size. This finding is in agreement with previously published results for antidots arranged in square lattices prepared by conventional lithographic techniques [121, 122] and underlines the suitability of the self-assembly method used for the preparation of the samples in this work.

Geometry dependent coercivity is also discussed in the work of Symth et al. [123]. There, coercivity is tuned by the aspect ratio of ferromagnetic nano-bars. They found a monotonous increase in coercivity with the bar's aspect ratio due to increasing shape anisotropy. As will be shown in section 4.2 by means of magnetic force microscopy, the remaining ferromagnetic material between two neighboring holes can (under certain circumstances) be treated as a single domain bar magnet, and a higher hole diameter increases the aspect ratio of these bars. This suggests that shape anisotropy is an important driver for the augmented coercivity in the antidot arrays.

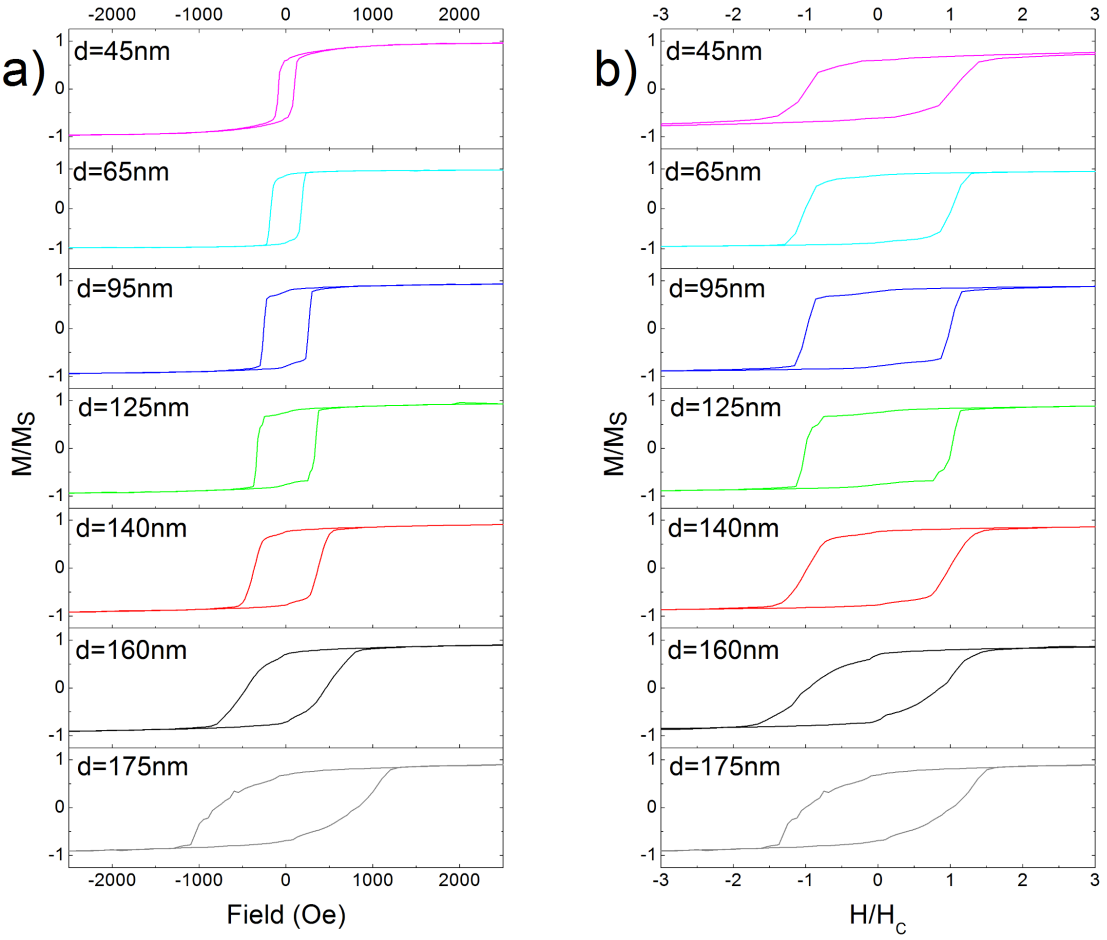

Figure 4.2: In-plane hysteresis loops of $20\,\mathrm{nm}$ thick Fe antidot arrays with constant period of $a = 200\,\mathrm{nm}$ nm and varied antidot diameter d measured at $T = 300\,\mathrm{K}$. In a) the field is scaled in absolute units and a monotonous increase in coercivity with increasing antidot diameter can be observed. In b) the field is normalized with respect to the coercive field. The hysteresis loops change from a square-like behavior for smaller hole diameters towards a more convex shape with a much wider switching field distribution for larger diameters.

In Figure 4.2 b) the diameter dependent hysteresis loops are plotted on a field axis which is normalized to the coercive field. While for diameters below $d = 140\,\mathrm{nm}$ the loops are more square-like, above this diameter the loops become more and more distorted towards a

convex shape with a much broader switching field distribution. This finding gives a first hint towards a change in reversal mechanism when the antidot diameter is increased above this threshold and will be discussed later in more detail.

A closer look at the hysteresis loops' shape reveals more differences originating from the changing antidot diameter: The sample with $d = 45\,\mathrm{nm}$ exhibits the smallest relative remanent magnetization of all the tested samples with a value of $M_R = 0.62 M_S$. This becomes more evident in Figure 4.4 a), where the remanent magnetization is plotted against the antidot diameter.
In fact, the X-ray microscopic examination presented in Figure 4.3 revealed that for such small antidot diameters the holes not only act as pinning sites for domain walls, but also facilitate the nucleation of reversed domains even in the remanent state. While the saturating field is applied (Figure 4.3 a)), the absorption is homogenous with only the holes resulting in bright spots due to the absence of absorbing material. The bright lines which start from the holes and are roughly parallel to the diagonal of the image can be attributed to an astigmatism of the X-ray lens system. In Figure 4.3 b), which shows the remanent state, reversed domains can be identified which appear darker as the XMCD-absorption is increased for this magnetization direction. Remarkably, the domain walls are all aligned with rows of antidots following the nearest neighbor direction of the lattice closest to the direction of the saturating field. Some of the domains are trapped exactly between two neighboring antidot rows and have a width of exactly one lattice constant $a = 200\,\mathrm{nm}$. This strong correlation between magnetic domains and antidot lattice is convincing evidence for domain wall pinning.

In order to explore the interplay between the antidot arrays' geometry and intrinsic properties of the ferromagnetic film, a set of samples was prepared within which for each chosen antidot diameter d a sample with a film of $t = 20\,\mathrm{nm}$ of either Fe, Co or Permalloy ($Ni_{80}Fe_{20}$) was deposited. The lattice parameter was held constant at $a = 200\,\mathrm{nm}$. All these materials can be considered as magnetically soft and show a polycrystalline growth, implying that the magnetization prefers in-plane orientation. In Figure 4.4 a) and b) the results for remanent magnetization M_R/M_S and the coercivities H_C are summarized for all three materials as a function of antidot diameter.

For the remanence, no significant material specific trends could be identified. All tested ferromagnets exhibit a minimum in remanence at diameters of either $d = 45\,\mathrm{nm}$ or $d = 65\,\mathrm{nm}$, followed by a maximum in remanence at the next larger diameter. From this point on, the remanence decreases monotonously with increasing diameter.

As an almost material independent property, the remanence of the antidot array is mainly determined by the sample shape. This finding is supported by micromagnetic simulations,

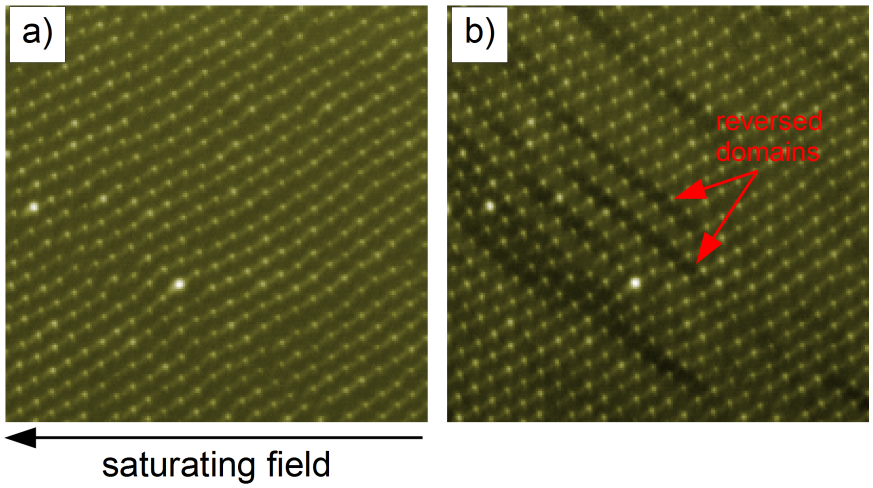

Figure 4.3: Scanning Transmission X-ray Microscopy (STXM) Images recorded with circularly polarized light ($h\nu = 708\,\mathrm{eV}$, Fe L_3 resonance position) at ambient temperature, showing an Fe antidot array with $a = 200\,\mathrm{nm}$, $d = 45\,\mathrm{nm}$, $t = 20\,\mathrm{nm}$. The brighter a pixel appears, the lower the corresponding absorption. a) shows the sample in a saturating field of $H = 2400$ Oe. b) shows the remanent state, in which reversed domains already nucleated and grew.

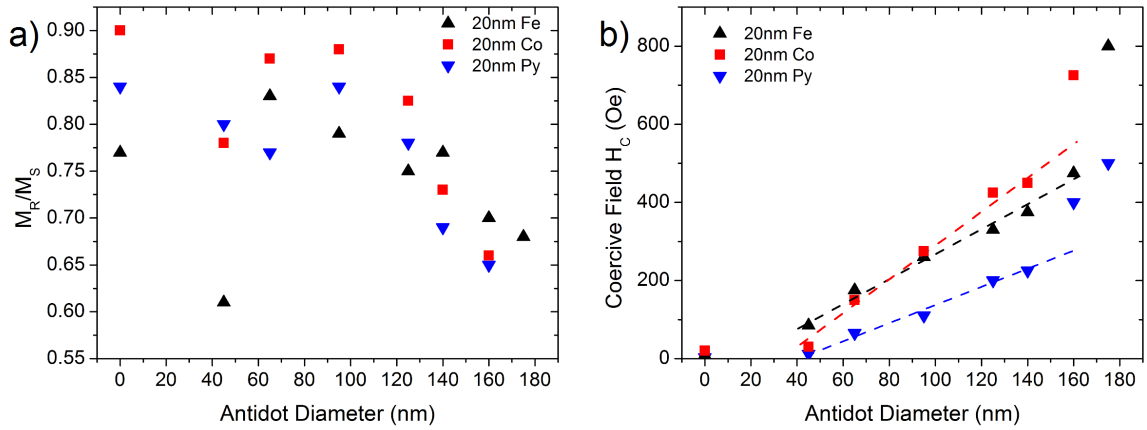

Figure 4.4: Summary of in-plane magnetic properties of various antidot samples. a) shows the remanent magnetization M_R/M_S and b) the coercive field H_C for Fe, Co and Permalloy as a function of the antidot diameter at fixed film thickness $t = 20\,\mathrm{nm}$ and antidot period $a = 200\,\mathrm{nm}$. All values correspond to $T = 300\,\mathrm{K}$.

where the domain pattern in remanence resulting from a given antidot geometry is the same for all three materials. This aspect will be discussed in Section 4.2. The reduced remanence for small antidot diameters can be attributed to their role as nucleation sites for reversed domains as shown in Figure 4.3.

The finding of the decreasing remanence with increasing diameter is consistent with above interpretation that the shape anisotropy is amplified by larger hole diameters. Returning to the model of single domain "'bar magnets"' which emerge in between two neighboring

holes, and considering the 6-fold symmetry of the hexagonal antidot lattice, it is evident that not all of these bar magnets can have their easy axis oriented parallel to the externally applied field. Within this model, a reduced remanence can be explained by the relaxation of the magnetization into their respective off-field easy axes. Additionally, this effect increases with increasing shape anisotropy. Thus, the observed downward trend in M_R for larger antidot diameters can be made plausible.

For the coercivity (see Figure 4.4 b)), Cobalt and Permalloy antidot arrays show very similar trends as previously discussed for Iron: The larger the antidot diameter, the higher the resulting coercive field. For all materials, the behavior for antidot diameters until $140\,\mathrm{nm}$ or 160 nm is described well by a linear fit, followed by a disproportionately strong increase of the coercivity for even larger diameters. Along with the previously discussed broadening in the switching field distribution, this gives another hint for a change in reversal mechanism within this diameter regime. In the microscopic study presented in Section 4.2, the origin of this transition will be investigated.

It is noticeable that Permalloy exhibits the smallest coercive fields for all antidot diameters, while the coercive fields for Iron and Cobalt are approximately on the same level for antidot diameters below $d = 95\,\mathrm{nm}$. For larger antidots, the coercivity of the Cobalt antidot arrays exceeds the values obtained for Iron.

At this point, the question arises as to which material parameter influences the magnetization reversal in what way. According to table 4.1, the materials differ in their saturation magnetization M_S, with Iron displaying the highest value followed by Cobalt and then Permalloy. On the other hand, Cobalt's exchange constant A is more than twice the one of Permalloy, while the one for Iron situated in between the other two.

A closer look at the $M(H)$ curves of the magnetization reversal for the three different materials helps answering the question above. Figure 4.5 a) shows the measured curves for $d = 125\,\mathrm{nm}$. For this diameter, Cobalt has the highest H_C at $425\,\mathrm{Oe}$, closely followed by Iron ($H_C = 325\,\mathrm{Oe}$) and eventually Permalloy ($H_C = 200\,\mathrm{Oe}$). More importantly, for Iron and Permalloy once again a kink in the $M(H)$ curves is visible. As will be discussed in Section 4.4, this kink indicates a transition from magnetization rotation (reversible; small slope) towards nucleation and movement of magnetic domains (irreversible; large slope). These transitions are marked by colored arrows in the Figure and occur at $H = 250\,\mathrm{Oe}$ for Iron and $H = 75\,\mathrm{Oe}$ for Permalloy. In the curve for the Cobalt antidot array, this feature is smeared out and cannot be identified clearly. However, in the respective simulated curve (Figure 4.5 b)) the feature appears.

Simulations were carried out using the material parameters presented in table 4.1, while any magnetocrystalline anisotropy was neglected. This is justified by the large enhance-

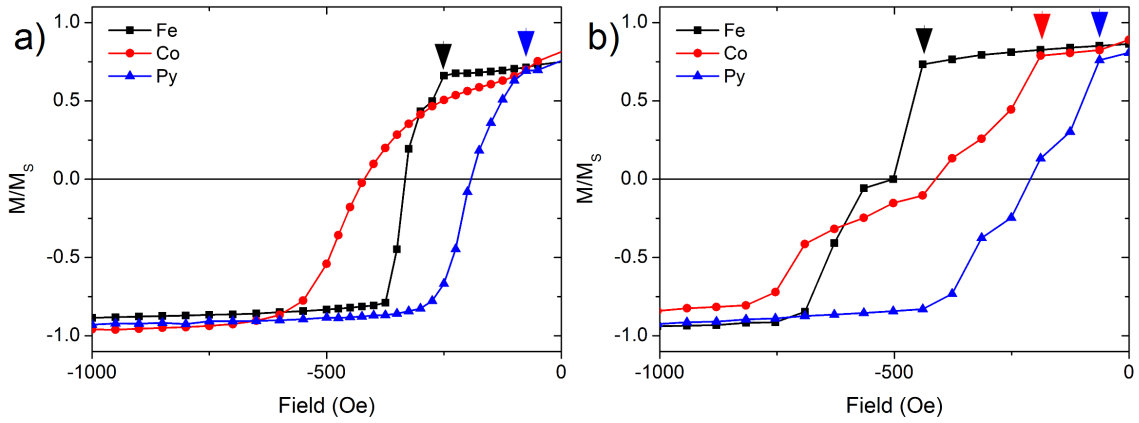

Figure 4.5: $M(H)$ curves of the magnetization reversal for antidot arrays with $a = 200\,\mathrm{nm}$ and $d = 125\,\mathrm{nm}$ for film materials Fe, Co and $Ni_{80}Fe_{20}$. a) shows the measured ($T = 300\,\mathrm{K}$) and b) the simulated set of curves. While the thickness in the experiment was $20\,\mathrm{nm}$, the simulations used the reduced thickness of $5\,\mathrm{nm}$ (see Section 3.5). The colored arrows indicate the respective transitions from reversible magnetization rotation towards nucleation, movement and (de-)pinning of reversed domains.

ment of coercive fields in the antidot arrays when compared to their planar reference films, which shows that magnetocrystalline anisotropy only plays a minor role compared to the shape anisotropy induced by the holes. The requirements of a reasonable computation time (see Section 3.5) forced reduction of the modeled section to dimensions of $1000 \times 866 \times 5\,\mathrm{nm}^3$, incorporating 28 holes. It is not surprising that such a reduced sample geometry will not succeed in exactly reproducing the experimentally determined coercive fields due to large demagnetizing fields originating at the sharp edges of the modeled section. Nevertheless, the overall shape of the simulated curves mimic the measured ones convincingly.

Table 4.1: Relevant magnetic material parameters (bulk) for Iron, Cobalt and Permalloy [124, 125, 126].

	Fe	Co	$Ni_{80}Fe_{20}$
M_S (kA/m)	1700	1430	800
A (pJ/m)	21	30	13

The fact that any difference among the three simulated curves originates exclusively from a variance in saturation magnetization and exchange constant allows to carefully draw conclusions on the effect of both material parameters on the magnetization reversal. It is noticeable that aforementioned transitions are shifted towards higher counter fields for larger values of the saturation magnetization of the respective material: these transitions are observed at $440\,\mathrm{Oe}$, $190\,\mathrm{Oe}$ and $65\,\mathrm{Oe}$ for Iron, Cobalt and Permalloy respectively. This

is a reasonable result: As mentioned earlier in this section, the kink can be interpreted as that the shape anisotropy introduced by the antidots is overcome by the Zeeman energy generated by the external field, and upon further increase of the field the reversal happens via domain wall movement. On the other hand, this shape anisotropy is based on interaction of the sample's stray field (generated by its magnetization) with its own magnetization $\vec{M}(\vec{r})$ (cf. Equation 1.7), thus the resulting anisotropy energy should increase with increasing M_S. However, this effect is offset by the growing interaction of the external field with a higher saturation magnetization and depends on the exact sample magnetization $\vec{M}(\vec{r})$. Thus, the problem is too complex to provide an analytical solution for the field at which this transition sets in.

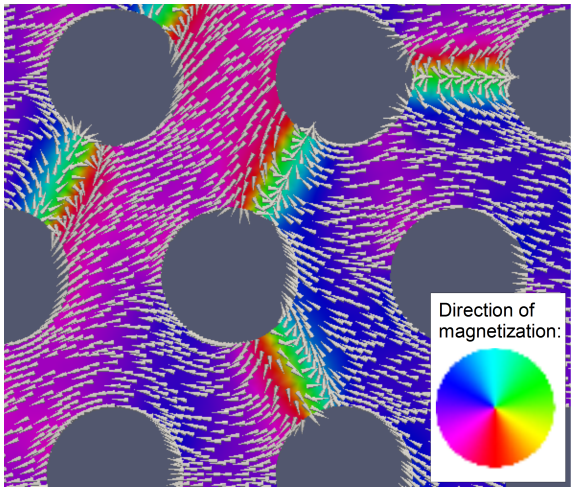

Figure 4.6: Snapshot of the micromagnetic configuration during the simulated magnetization reversal ($H_{Ext} = -628\,\mathrm{Oe}$) of a cobalt antidot array with $a = 200\,\mathrm{nm}$, $d = 125\,\mathrm{nm}$ and $t = 5\,\mathrm{nm}$. The color represents the local in-plane magnetization direction. Domain walls, noticeable by a strong contrast in color, are pinned between two neighboring holes.

How do the samples behave for counter-fields beyond the transition? Cobalt, the material with the largest exchange constant (see Table 4.1), shows the flattest curve (i.e. has the broadest switching field distribution) after the kink in both experiment and in the simulation (Figure 4.5). The relatively small slope in this regime of the $M(H)$ curve points towards a strong domain wall pinning effect. According to D.I. Paul [127], the energy of a domain wall is proportional to its spatial dimensions and the exchange constant A of the magnetic material, as well as to the anisotropy constant K. For Cobalt, the domain wall energy should thus be the highest of all three materials. The STXM micrographs for the Fe antidot array in Figure 4.3 and the snapshot from the micromagnetic simulation of the Cobalt antidot array's magnetization reversal in Figure 4.6 show that the domain walls follow the nearest neighbor direction of the antidot lattice. In a very basic model, one can attribute the pinning effect simply to the fact that a domain wall which incorporates a non-magnetic hole

reduces its energy because in that way it minimizes its volume, in analogy to the domain wall pinning in a ferromagnetic nano-wire containing a notch [128]. In turn, this pinning becomes more effective the more energy is saved by incorporating the non-magnetic defect into the domain wall, i.e. it scales with the domain wall energy. Thus, the high de-pinning fields which are necessary to complete the magnetization reversal for the Cobalt antidot array can be explained qualitatively.

4.1.2 Influence of lattice parameter

Furthermore, it was of interest how the magnetic properties of antidot arrays change upon further reduction of the antidot periodicity. While plenty of publications can be found for $a > 200\,\mathrm{nm}$ [129, 130], the regime towards smaller periodicity is not easily accessible. Relevant publications mostly made use of anodic aluminum oxide (AAO) membranes as templates for deposition of the magnetic thin film, which results in highly ordered hexagonal antidot arrays, however with disadvantages in control of antidot size and a loss in their spherical shape [131, 132, 133].

In Figure 4.7 a) a comparison of coercive fields for the previously discussed set of Fe antidot arrays with $a = 200\,\mathrm{nm}$ and a set of Fe antidot arrays with $a = 100\,\mathrm{nm}$ as a function of d/a-ratio is shown. The film thickness of all samples is $t = 20\,\mathrm{nm}$. For all but the smallest diameters, reduction of periodicity increases coercivity. This effect would probably be even larger, if the same degree of order could be achieved for $a = 100\,\mathrm{nm}$ as for $a = 200\,\mathrm{nm}$, which is unfortunately not the case as seen in the SEM micrograph of Figure 4.7 b). The lattice shown contains many dislocations, as the forces driving the self-assembly weaken for smaller sphere diameters.

The tendency towards higher H_C for smaller periodicity might be caused by an increase in antidot “perimeter areal density”, i.e. the length of the antidots’ perimeter per area of the antidot array’s surface:
The area of a primitive unit cell within a hexagonal lattice is $A = \sqrt{3}a^2$. This unit cell contains one entire antidot with a total perimeter of $U = \pi d$. Aforementioned perimeter areal density R is then given by

$$R = \frac{U}{A} = \frac{\pi}{\sqrt{3}} \frac{1}{a} \frac{d}{a} \tag{4.1}$$

Thus, R scales reciprocally with the periodicity of the antidot lattice for a given d/a ratio. Since shape anisotropy originates from the antidots’ edges, an increase in H_C with shorter lattice constant is expected. This is consistent with values reported for Permalloy antidot arrays with very large lattice parameters of $a = 3\,\mu\mathrm{m}$ and d/a ratio of 0.5, where the enhancement in coercivity is reduced to merely a factor of 3 with respect to the reference

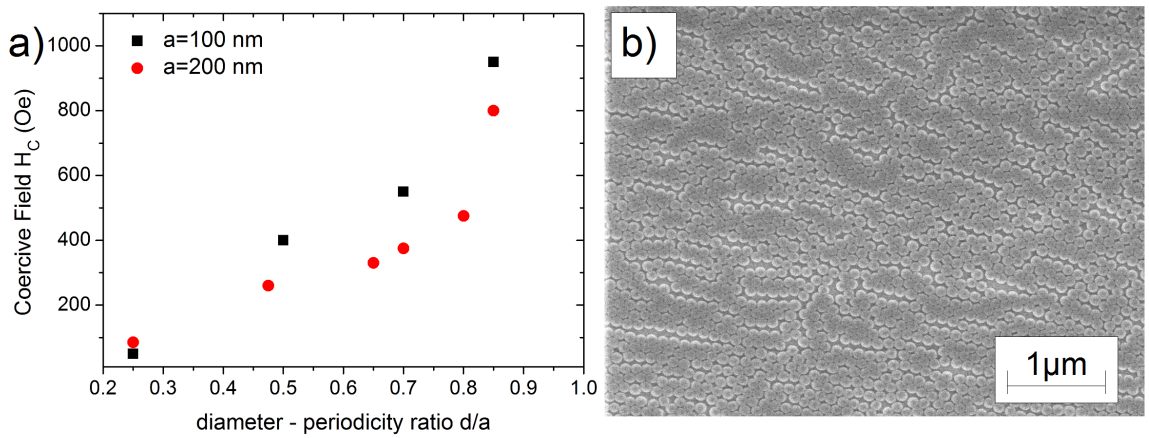

Figure 4.7: a) H_C vs. d/a ratio for $a = 100\,\mathrm{nm}$ (black) and $a = 200\,\mathrm{nm}$ (red). Film thickness in both cases is $t = 20\,\mathrm{nm}$. All values correspond to $T = 300\,\mathrm{K}$. b) SEM micrograph of the self assembled polystyrene monolayer, which eventually served as the template for antidot arrays with $a = 100\,\mathrm{nm}$. For this smaller periodicity, the amount of defects in the hexagonal lattice is significantly increased.

film [134]. In that case, the magnetocrystalline anisotropy of the magnetic thin film is of the same magnitude as the shape anisotropy of the holes.

Both depicted $H_C(d/a)$ plots, however, show again the same trends: an increase in diameter leads to higher coercive fields. Especially a strong increase in coercivity is observed between a d/a ratio of 0.7 and 0.87. This finding suggests that the d/a ratio is the critical parameter for the transition in magnetization reversal behavior which already has been discussed for the materials Fe, Co and $Ni_{80}Fe_{20}$ in the previous section. The microscopic origin of this transition will be discussed in section 4.2 by means of magnetic force microscopy.

4.1.3 Out-of-plane magnetization reversal

The presence of the antidots not only alters the in-plane magnetic properties of the thin films, but also affects the out-of-plane behavior. This can be seen in Figure 4.8, where out-of-plane hysteresis loops are shown for $t = 20\,\mathrm{nm}$ thick Fe antidot arrays with $a = 200\,\mathrm{nm}$ and diameters $d = 175\,\mathrm{nm}$, $d = 45\,\mathrm{nm}$ as well as for an planar reference film. The out-of-plane remanent magnetization M_R/M_S is smaller than 0.1 for all of the samples, clearly indicating that in-plane magnetization is favored.
While the reference film (black curve) does not saturate until a field of $H = 30\,\mathrm{kOe}$, this reduces to $H = 22\,\mathrm{kOe}$ for the antidot array with $d = 175\,\mathrm{nm}$ (red curve). In that respect, the antidot array with $d = 45\,\mathrm{nm}$ behaves very similar as the reference film, saturating this sample is only marginally easier. This observation can be made plausible with the shape

anisotropy of the respective samples: For the antidot array with the largest hole diameter, the distance in between neighboring holes reduces to $25\,\mathrm{nm}$. This, however, is close to the thickness of the thin film ($20\,\mathrm{nm}$) and in turn reduces the relative energy penalty for an out-of-plane magnetization. This effect is much smaller for the sample with $d = 45\,\mathrm{nm}$, with a hole-to-hole distance of $155\,\mathrm{nm}$ which still exceeds the film thickness by a factor of more than 7.

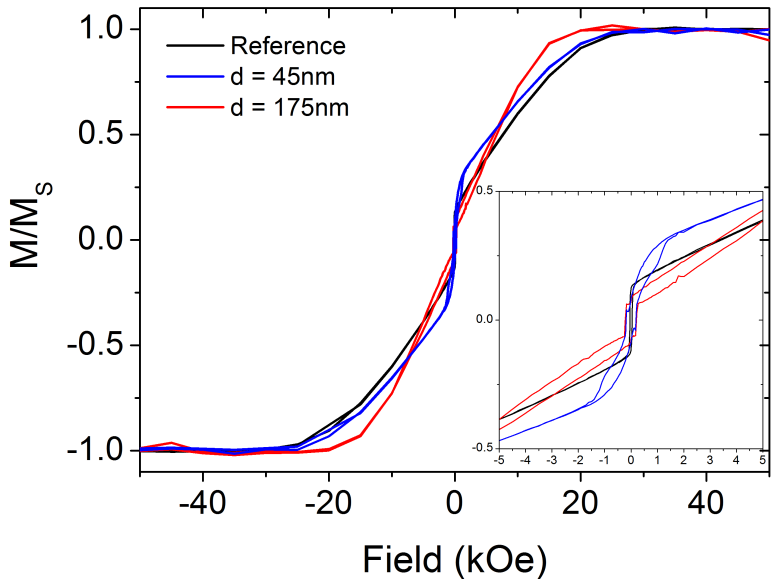

Figure 4.8: Out-of-plane hysteresis loops for $20\,\mathrm{nm}$ thick Fe antidot arrays with a lattice parameter of $a = 200\,\mathrm{nm}$ and varied diameter and a corresponding planar reference film measured at $T = 300\,\mathrm{K}$. The inset shows a magnification of the region around $H_{ext} = 0$.

On the other hand, even the $45\,\mathrm{nm}$ large holes influence the magnetization reversal behavior, especially for smaller fields around $H = 0$, as shown in the inset of Figure 4.8. Compared to the reference film, both antidot arrays have broadened hysteresis loops, although the effect is by far not as strong as in the in-plane direction. This can be regarded as an indicator for domain wall pinning even in the out-of-plane direction, or as another consequence of the decreased energy difference between a magnetization pointing out of the film plane and a magnetization within the film plane..

4.1.4 Temperature dependent hysteresis behavior

Temperature dependent magnetization reversal measurements are motivated by the fact that the micromagnetic simulation packages used for the modeling of the antidot arrays neglect any temperature effect. In order to allow for a better comparison between experimental data, which is mostly obtained at either room temperature, or, in the case of the

magnetotransport measurements presented in section 4.3 at $T = 77\,\mathrm{K}$, and simulated data, the evolution of magnetization reversal with changing temperature was investigated. Figure 4.9 exemplary shows in-plane hysteresis loops of an Fe antidot array with film thickness $t = 20\,\mathrm{nm}$, lattice parameter $a = 200\,\mathrm{nm}$ and antidot diameter $d = 160\,\mathrm{nm}$ for temperatures $10\,\mathrm{K}$, $77\,\mathrm{K}$ and $300\,\mathrm{K}$.

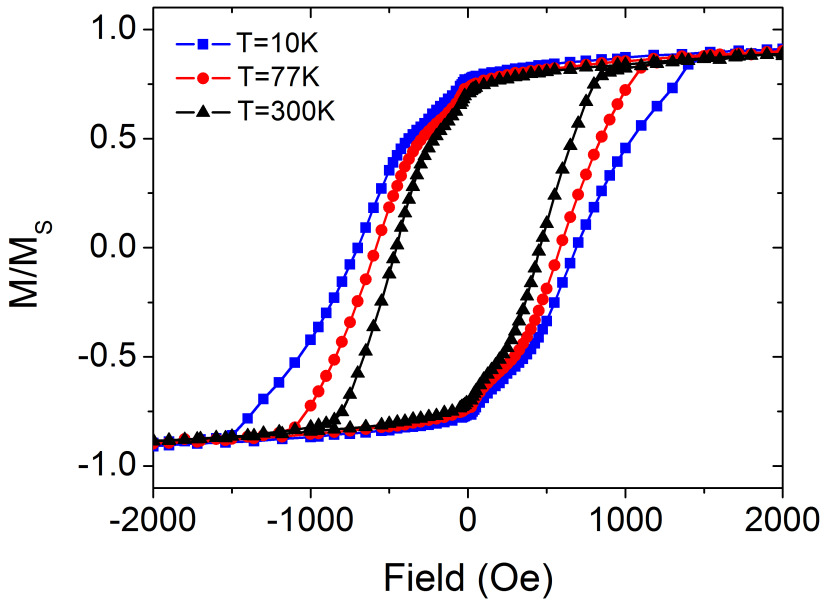

Figure 4.9: In-plane hysteresis loops of an $t = 20\,\mathrm{nm}$ thick antidot array with $a = 200\,\mathrm{nm}$, $d = 160\,\mathrm{nm}$ for the temperatures $10\,\mathrm{K}$, $77\,\mathrm{K}$ and $300\,\mathrm{K}$.

One can observe the expected tendency, as for example presented in reference [135] for the case of cobalt antidot arrays: the lower the temperature, the broader the hysteresis becomes. While for a temperature of $T = 300\,\mathrm{K}$, the sample shows a coercivity of $H_C = 450\,\mathrm{Oe}$, this increases to $575\,\mathrm{Oe}$ and $700\,\mathrm{Oe}$ for $T = 77\,\mathrm{K}$ and $T = 10\,\mathrm{K}$, respectively. These values correspond to an increase of 28% and 55% with respect to the coercivity at room temperature. These values fit very well to the observed difference between the coercivity of an Fe antidot array determined by magnetotransport ($T = 77\,\mathrm{K}$) and the corresponding simulation ($T = 0\,\mathrm{K}$) presented in Section 4.4.

The behavior can be explained by reduction of thermally induced magnetization flipping at lower temperatures. Additionally, the saturation magnetization grows towards lower temperatures which in turn increases the shape anisotropy. In fact, a change in the sample's saturation moment was observed: From $\mu_S = 2.42 \times 10^{-7} Am^2$ at room temperature, the moment increases to $2.5 \times 10^{-7}\,\mathrm{Am}^2$ for $T = 77\,\mathrm{K}$ and $2.52 \times 10^{-7}\,\mathrm{Am}^2$ at $10\,\mathrm{K}$. These effects might be amplified by an increase in the Iron's magnetocrystalline anisotropy with decreasing temperature [136], although due to the dominance of the shape anisotropy this contribution is expected to be small.

4.1.5 Summary

In this section, it was investigated how the presence of the holes alters the integral magnetization behavior of $t = 20\,\mathrm{nm}$ thick films of either Fe, Co or Py. Based on a sample series with a common lattice parameter of $a = 200\,\mathrm{nm}$, the coercive field is found to increase monotonously with increasing antidot diameter d for all the tested materials. For antidot diameters in the range from $45\,\mathrm{nm}$ to $140\,\mathrm{nm}$, the coercive field can be described as a linear function of the diameter. For even larger hole diameters, the coercive field grows by a disproportionally large margin. This is accompanied by a change in the hysteresis loops' shape from square-like for diameters of $140\,\mathrm{nm}$ and below, to a more convex shape with a broader switching field distribution. These findings indicate a transition in the principal magnetization behavior in this diameter regime.
A reduction of the lattice parameter from $200\,\mathrm{nm}$ to $100\,\mathrm{nm}$ leads to a further increase of the observed coercive fields for a given diameter-to-lattice parameter (d/a) ratio. For this smaller periodicity, the disproportionally large increase in coercivity sets in at diameters between $70\,\mathrm{nm}$ and $85\,\mathrm{nm}$. In combination with the results for antidot arrays with a lattice parameter of $a = 200\,\mathrm{nm}$, one can identify the d/a ratio as the main driver for the transition in the magnetization behavior. The critical d/a ratio is in the range between 0.7 and 0.89. This will be investigated on a microscopic scale in the next section.

The enhanced coercivity in antidot arrays was attributed to a combination of domain wall pinning at the antidot sites and a strong in-plane shape anisotropy arising from the holes. When for a given geometry only the magnetic material differs, Permalloy antidot arrays always exhibit the smallest coercive field. It is suggested that this is due to the relatively small saturation magnetization of this material ($M_S = 800\,\mathrm{kA/m}$), which reduces the shape anisotropy effect (cf. Equation 1.7). For all materials, the antidot arrays' in-plane hysteresis loop shows a kink at a sample-specific field, which separates reversible rotation of the magnetization from irreversible nucleation and growth of reversed domains. This aspect will be investigated in more detail in Section 4.4. The kink is interpreted as the field at which the Zeeman energy of the external field overcomes the shape anisotropy of the holes. For Fe antidot arrays (bulk value of saturation magnetization: $M_S = 1700\,\mathrm{kA/m}$), this kink occurs at larger reversal fields as compared to Co samples ($M_S = 1440\,\mathrm{kA/m}$), which gives further support for above shape anisotropy argument.

Domain wall pinning could be directly observed by means of Scanning Transmission X-ray microscopy. The domain walls of an Fe antidot array ($a = 200\,\mathrm{nm}$, $d = 45\,\mathrm{nm}$, $t = 20\,\mathrm{nm}$) tend to connect neighboring holes. This finding is also reproduced in micromagnetic simulations. The exchange constant of Cobalt is the largest in the set of investigated materials, and the hysteresis loops for Co antidot arrays show the broadest switching field

distribution for fields beyond the kink, i.e. in the regime where the growth of reversed domains is the dominant process. A large exchange constant leads to a large domain wall energy, which seems to make the domain wall pinning more effective.

In order to determine the effect of temperature on the magnetization reversal, hysteresis loops were measured at temperatures $10\,\mathrm{K}$, $77\,\mathrm{K}$ and $300\,\mathrm{K}$. This is motivated to allow for comparability between measurement and simulation. The latter do not include a modeling of the temperature, i.e. mimic the behavior at $T = 0\,\mathrm{K}$. The hysteresis loops show the expected broadening with decreasing temperature. With respect to room temperature, the coercivity at $T = 77\,\mathrm{K}$ is increased by 28%, and at $T = 0\,\mathrm{K}$ by 55%.

Although the antidot arrays clearly favor an in-plane magnetization, the out-of-plane reversal is altered by the nanoscaled holes. Especially antidot samples with a large d/a ratio, where film thickness and the distance between two neighboring holes is almost equal, are significantly easier to saturate in the out-of-plane direction than the respective reference film.

4.2 Intrinsic domain structures of hexagonal antidot arrays

Reducing a ferromagnet's geometrical dimensions to its intrinsic length scales such as the domain wall width, will always affect the domain structure. Prominent examples are the vortex states which arises in micron scaled soft magnetic discs [2, 137, 138], or the ensemble of macrospins of artificial spin-ice [12, 51]. In the present work, the undisturbed domain wall width in the polycrystalline thin films is in the range of 30 - $200\,\mathrm{nm}$ [26, 27]. Hence, it can be expected that nanostructures with a periodicity in the order of $200\,\mathrm{nm}$ should reflect on the magnetization patterns.

In the previous section, a broadening of the switching field distribution and a drastic increase in coercivity above a d/a-ratio of around 0.75 indicated a change of the mechanism of the magnetization reversal. However, no explanation of the nature of this change has been given so far. With the help of magnetic force microscopy (MFM) and subsequent correlation with micromagnetic simulations, it is possible to get detailed information about the domain configuration of the antidot samples. In this way, it is found that the "intrinsic" domain structure, resulting from the shape anisotropy of the antidot pattern, changes around the same d/a ratio in which integral measurement data suggests a transition. Parts of the present section have been published in *Nanotechnology* [139], and are reproduced here with permission of IOP publishing.

To test for above mentioned transition, $t = 20\,\mathrm{nm}$ thick Fe antidot arrays with diameters $d = 110\,\mathrm{nm}$ and $d = 170\,\mathrm{nm}$ were investigated. With a lattice constant of $a = 205\,\mathrm{nm}$, this corresponds to d/a ratios of 0.54 and 0.83, respectively. Thus, they represent geometries well below and above the critical value of 0.75. In order to have the samples in a well defined state, they were saturated by an in-plane field of $H_{ext} = 10\,\mathrm{kOe}$ prior to MFM analysis. The measurements then took place with the samples in their remanent states.

Indeed, MFM reveals very different remanent domain configurations for both cases as demonstrated in Figure 4.10 a) and Figure 4.11 a). The color coding represents maximum attractive (repulsive) tip-sample-interaction for dark (bright) contrast, respectively. Note that the direction of the initial saturation field is indicated on the right margin of the Figures. In order to allow correlation between magnetization and sample geometry, the positions and perimeters of the antidots as revealed by tapping mode atomic force microscopy and software recognition are overlaid on the magnified MFM images (closed black circles) in panels b) of Figures 4.10 and 4.11. The sharp edges at antidot perimeters are artifacts produced by software, AFM images reveal circular antidots (not shown). Furthermore, the primitive lattice unit cells (dashed lines) of the antidot lattice are included.

4.2.1 Domain pattern for small d/a ratio

For the small antidot diameter $d = 110\,\mathrm{nm}$ (Figure 4.10 a)), the remanent state appears in MFM as a hexagonal arrangement of rhombi, each consisting of a bright and a dark half. Interruptions of this periodic arrangement are caused by defects within the antidot lattice, for example in the upper right corner of the MFM image. In Figure 4.10 b) it becomes evident, that each rhombus can be assigned to a primitive unit cell of the hexagonal antidot lattice. Here, the nearest neighbor direction which encloses the smallest angle with the initially applied saturating field stands out as the only mirror axis of the image. The choice of the primitive unit cell was motivated by this symmetry.

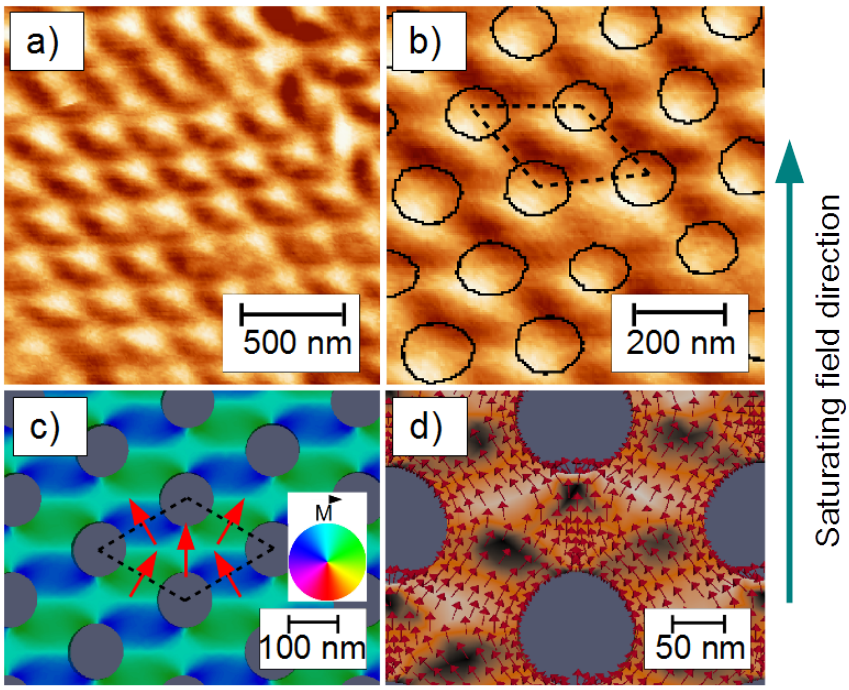

Figure 4.10: Domain pattern of hexagonal antidot arrays with lattice parameter $a = 205\,\mathrm{nm}$ and hole diameter $d = 110\,\mathrm{nm}$ in the remanent state after saturation in an external electromagnet. (a) shows an $1.5 \times 1.5\,\mu\mathrm{m}^2$ MFM image while the positions of antidots as observed by AFM topography-scans and software recognition are added to panel (b) in magnified the region of (a). The tip-sample distance was $10\,\mathrm{nm}$. (c) presents the simulated magnetization pattern for the experimental antidot geometries. Red arrows indicate the direction of magnetization in each domain of the unit cell (dashed lines). In panel (d) the color code represents magnetic charge distribution ($\mathrm{div}\,\vec{M}(\vec{r})$) derived from the magnetization vectors (red arrows). Images adopted from [139].

A more thorough interpretation of the MFM images becomes possible with help of micromagnetic simulations. Figure 4.10 c) shows the simulated remanent state for the experimentally investigated antidot geometry $a = 205\,\mathrm{nm}$, $d = 110\,\mathrm{nm}$ and $t = 20\,\mathrm{nm}$. The color coding indicates the in-plane directions of the local magnetization vector. Additionally, the

primitive unit cell of the antidot lattice is marked by dashed lines, also having the same mirror symmetry axis along its nearest neighbor direction as the one sketched in the experimental data (Figure 4.10 b)). Furthermore, the average magnetization direction of the simulated remanent state is identical with the symmetry axis, which makes it possible to deduce the in-plane magnetization from a MFM image.
The simulated unit cell consists of five magnetic domains, whose magnetization vector directions are emphasized by the five red arrows: a central domain which is magnetized along the nearest neighbor direction and four domains on the edges of the unit cell which are tilted by $\pm 30^\circ$ with respect to the central domain. These four outer domains are all situated between two neighboring holes and their magnetization direction coincides with a next nearest neighbor direction of the antidot lattice. It is worth mentioning that for almost all in-plane directions of the applied saturating field the observed magnetization pattern is the same: the magnetization of the central domain relaxes into the nearest neighbor direction which is closest to this field [139]. In other words, the average magnetization relaxes into one of the nearest neighbor directions which could thus be considered as the intrinsic easy axis of the antidot lattice below the critical d/a ratio of 0.75. Only when the field was applied with angles above 28° with respect to a nearest neighbor direction, i.e. an easy axis, the resulting remnant magnetization pattern is not periodic anymore. This in-plane anisotropy cannot be resolved by SQUID magnetometry, as the colloidal self assembly yields domains of perfect hexagonal order of typically up to $25 \times 25\,\mu\mathrm{m}^2$. On a $5 \times 5\,\mathrm{mm}^2$ large substrate, a multitude of such structural domains nucleate, which all exhibit random crystal orientation with respect to each other, similar to a polycrystalline solid. The investigation thus has to be restricted to a single crystallite of the antidot lattice in order to resolve the in-plane anisotropy. This topic will be addressed in section 4.4.

Since MFM detects the magnetic stray field which has its sources and sinks in magnetic charges (see section 3.3 “MFM”), it is appropriate to derive the magnetic charge distribution $(\mathrm{div}\,\vec{M})$ from the simulated magnetization pattern. The results of this calculation are shown in Figure 4.10 d) and can be directly compared with the MFM data. With a mostly negative magnetic charge (black) on its lower edge and mostly positive (white) charge at the upper edge, the depicted primitive unit cell reproduces the experimental data convincingly.

4.2.2 Domain pattern for large d/a ratio

For larger antidot diameters, the remaining magnetic material in between two neighboring holes forms an elongated and, due to the curvature of the holes, waisted structure. In between three neighboring holes, vertices arise, where three of these structure are connected to each other, thus exhibiting exchange coupling. According to their function of “bridging”

two neighboring vertices and due to their elongated shape, these structures were labeled "bridges" (see Figure 4.11 c) for definitions).

The MFM images for the larger antidot diameter ($d = 170\,\mathrm{nm}$) in Figure 4.11 a) and b) show alternating bright and dark spots, forming a honeycomb configuration. The largest stray fields detected by MFM are observed in the center between three antidots, i.e. at the vertices of the bridges. Similar to a nanoscaled bar magnet, the bridges' shape anisotropy aligns the magnetization towards their respective long axis. The odd number of connected bridges always yields a residual magnetic charge at the vertices which is responsible for the magnetic signal [139].

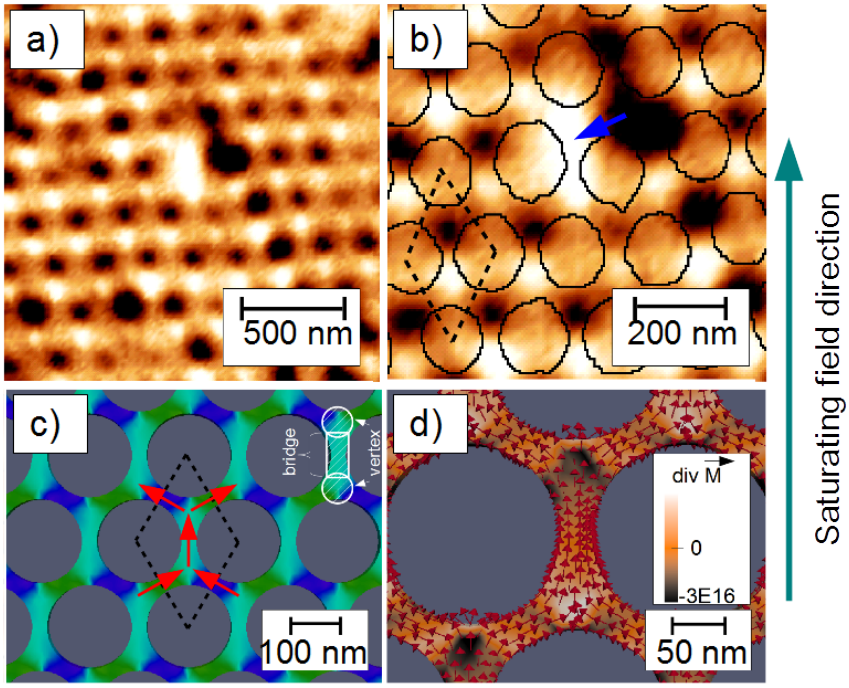

Figure 4.11: Domain pattern of hexagonal antidot arrays with lattice parameter $a = 205\,\mathrm{nm}$ and hole diameter $d = 170\,\mathrm{nm}$ in the remanent state after saturation in an external electromagnet. (a) shows an $1.5 \times 1.5\,\mu\mathrm{m}^2$ MFM image while the positions of antidots as observed by AFM topography-scans and software recognition are added to panel (b) in a magnified region of (a). The tip-sample distance was $10\,\mathrm{nm}$. In (b), the blue arrow indicates a single flipped bridge magnetization. (c) presents the simulated magnetization pattern for the experimental antidot geometries. Red arrows indicate the direction of magnetization in each domain of the unit cell (dashed lines). In panel (d) the color code represents magnetic charge distribution ($\mathrm{div}\,\vec{M}(\vec{r})$) derived from the magnetization vectors (red arrows). Images adopted from [139].

This interpretation is once more supported by micromagnetic modeling of the system: Figure 4.11 c) shows the simulated magnetization pattern while 4.11 d) shows the magnetic charge distribution $\mathrm{div}\,\vec{M}$. Similarly to the magnetization pattern for $d = unit[110]nm$ (Figure 4.10), the primitive unit cell contains a total of five domains in accordance to the five

bridges which are at least partially implied by the unit cell. However, their orientation is now different: the central domain's magnetization points towards the next nearest neighbor direction closest to the direction of the initially applied magnetic field, while the other four domains have their magnetization oriented to the next nearest neighbor directions enclosing angles of $\pm 60^\circ$ with the central bridge's magnetization. Consequently, the discussed periodic domain pattern is only generated when the field is not applied very close to one of the nearest neighbor directions of the antidot lattice, as this would result in the field pointing perpendicular to the long axis of a bridge. Upon switching off the external field, the direction into which the bridge's magnetization then relaxes would be random or determined by defects in the lattice, which makes the occurrence of a periodic state highly unlikely.
The influence of defects on the magnetization pattern can be seen in Figure 4.11. The magnetization of the bridge marked by the blue arrow switched due to mispositioned adjacent antidots, breaking the alternating pattern.

As described in Section 1.3 in the context of the discussion of spin-ice systems, it is convenient to describe the magnetization configuration in terms of magnetic charge. Thus, we assign the charges $\pm q_i = \frac{\mu}{l}$ (with μ being the magnetic moment of a bridge and l its length) to each end of the i-th bridge, respectively. With three bridges being connected to each vertex, there are a total of four possible charge states a vertex can attain:

$$q_{vertex} = \sum_{i=1}^{3} \pm q = \pm q_i \text{ or } q_{vertex} = \pm 3q \tag{4.2}$$

The $q_{vertex} = \pm 3q$ states would result in a three times higher signal than the $\pm q$ states in the MFM images and were not observed. The $\pm q$ vertex states result from two connected bridges having a magnetization direction towards the vertex, while one of the connected bridges has a magnetization pointing away from the vertex, or vice versa. These are the well known ice-rules for 2-dimensional Kagomé spin-ice structures [48, 119]. The analogy of the observed magnetization pattern and the Kagomé lattice is illustrated in Figure 4.12. In fact, the experimentally observed magnetization state in which each dark ($-q$) vertex has three neighboring bright ($+q$) vertices (and vice versa) is exactly the so-called charge ordered state of such an artificial spin-ice structure. This state is supposedly very stable, as it not only minimizes the energy of each single vertex due to confirmation with the ice-rules, but also the interaction energy between neighboring vertices due to the alternating arrangement of neighboring vertex charges. It often serves as starting point for subsequent magnetization reversal experiments to investigate frustration phenomena in such model systems [52, 140].

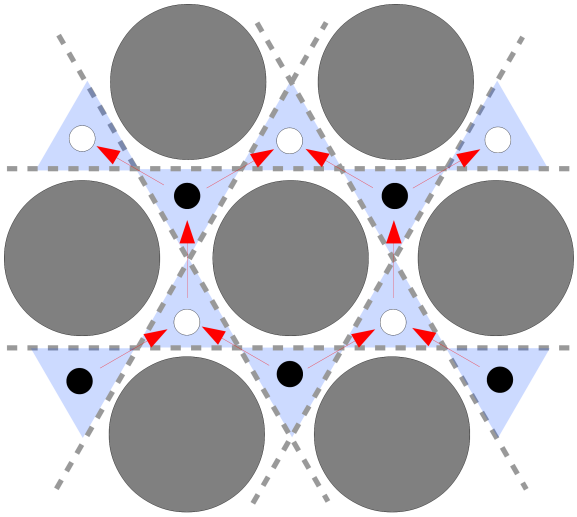

Figure 4.12: Analogy of the magnetization pattern identified by MFM and Kagomé lattice: The big gray circles represent the hexagonally ordered antidots. The crossings of the dashed gray lines form the Kagomé lattice. To each such lattice point a magnetization vector (red arrows) can be attributed. The resulting vertex-charges $\pm q$, symbolized by the small black and white circles, are situated within triangles defined by the dashed gray lines. These triangles are the equivalent of the tetrahedra in bulk spin-ice (see section 1.3).

How far the analogy of the magnetization properties of antidot arrays with established artificial spin-ice structures holds will be fathomed in Section 4.5, where the magnetization reversal of antidot arrays with large d/a ratio is investigated. Interesting magnetization reversal phenomena have so far been found in this kind of system, such as the occurrence of so called “monopole defects” [14], which essentially break down to violations of the ice-rules, as well as a magnetization reversal along one-dimensional paths [12] (see Section 1.3 for more details).

The preparation of artificial spin-ice structures by means of colloidal lithography offers additional possibilities as compared to the established e-beam lithography preparation technique. With its scalability, the technique allows to reduce the periodicity way below previous limits of $500\,\mathrm{nm}$. As the anisotropy energy, and thus the stability of the magnetization, scales with the volume of the elements assembling the spin-ice lattice, one could imagine to access dimensions in which the magnetization can be activated thermally. So far this was only possible by reducing the thickness of the magnetic material below $3\,\mathrm{nm}$ [141].

Figure 4.13 summarizes the findings of this section: The “intrinsic” domain structure of antidot arrays undergoes a transition at a d/a ratio of approximately 0.75. Independent of the antidot diameter, the primitive unit cell of the lattice contains five magnetic domains, with the four outer domains having a magnetization towards a next nearest neighbor direction. The main difference between the two patterns is the orientation of their respective central domain, which is marked in blue color in the Figure. For smaller antidot diameters

its magnetization is oriented towards the nearest neighbor direction which is closest to the saturating field, while for larger diameters this changes towards the next nearest neighbor direction closest to the saturating field.

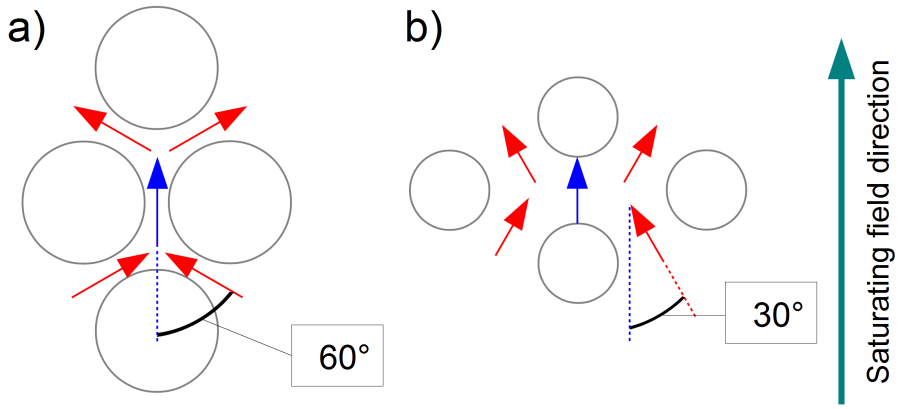

Figure 4.13: Schematics of the domain patterns in remanent state for a) d/a-ratio > 0.75 and b) d/a-ratio < 0.75.

At a first glance, the nearest neighbor orientation of the central domain's magnetization for $d/a < 0.75$ seems astonishing, as this means the magnetization points directly into a hole which is magnetostatically unfavorable. However, in terms of domain wall energy it is very well favorable, as insertion of this central domain reduces the angles between adjacent magnetic domains down to only $30°$ (see Figure 4.13 b)), as opposed to an angle of $60°$ without this central domain. As discussed in Section 1.1.5, the domains in softmagnetic thin films are separated by Neél walls. In the simulation snapshots presented in Figures 4.10 c) and 4.11 c) they can be identified as the contrast between domains changes gradually. The energy stored in such a Neél domain wall can be approximated as a function of the angle α between the magnetization directions of its adjacent domains as follows [142]:

$$E(\alpha) = E_{Neel}^{180°}(1 - \cos\frac{\alpha}{2})^2 \tag{4.3}$$

, where $E_{Neel}^{180°}$ is the domain wall energy of a $180°$ Neél wall. According to this equation, a reduction of the angle α from $60°$ to $30°$ reduces the domain wall energy by more than 93%.

An increase in antidot diameter leads to a more dominant role of the shape anisotropy, as the interface between ferromagnetic material and holes becomes larger. Thus, the cost of domain wall energy with the central domain's magnetization parallel to a nearest neighbor direction (which implies an angle of $60°$ between adjacent domains, see Figure 4.13 a)) becomes overcompensated by a gain in demagnetization field energy.

4.3 Anisotropic Magnetoresistance in Antidot Arrays

In this section, results from magneto-resistance measurements on Fe antidot arrays are presented. The focus hereby lies on the application of the anisotropic magneto-resistance (AMR) as characterization tool for the magnetization reversal process. This kind of magnetotransport measurement is often applied when the task is to characterize continuous ferromagnetic films or even nanowires [88, 143, 144]. In antidot arrays, however, the inhomogeneous current density distribution induced by the presence of the holes leads to specific features in the AMR measurements. By combining the inhomogeneous current density distribution with the characteristic domain pattern discussed in the previous section, it is possible to obtain a detailed understanding of the AMR signal formation. The sample setup used for AMR measurements is described in section 3.2.1, where also the formation of the typical AMR measurement signals is explained. In order to provide a stable temperature during the measurements, the samples were in liquid Nitrogen atmosphere at a temperature of $T = 77\,\mathrm{K}$.

4.3.1 Magnetotransport Measurements for Antidot Arrays with varied antidot diameter

Figure 4.14 presents magnetotransport measurements in longitudinal (a) and transverse (b) measurement geometry for a set of $t = 20\,\mathrm{nm}$ thick Fe antidot arrays with constant lattice parameter $a = 205\,\mathrm{nm}$ and varied hole diameter d. The resistance axis is normalized with respect to the resistance in remanence: $\Delta R/R(H_{ext} = 0)$. Curves measured in longitudinal geometry exhibit their characteristic dips, while the transverse curves show peaks. These features are very sharp and serve as precise indicators for the coercive field of the samples with antidot diameters $d = 155\,\mathrm{nm}$ and below, as comparison of the AMR curves with hysteresis loops obtained by SQUID magnetometry (Figure 4.14 c) reveals. SQUID measurements were also performed at $T = 77\,\mathrm{K}$ to allow for direct comparison. For the sample with $d = 175\,\mathrm{nm}$, the peaks as well as dips are significantly broadened, so that both features are smeared out. This is in accordance with the SQUID measurement, which shows that the corresponding $M(H)$ curve exhibits the broadest switching field distribution around the coercive field.

Principally, each AMR curve should be symmetric with respect to $H_{ext} = 0$. However, this is not the case for all the presented data. Even though the measurements were conducted with the samples placed in liquid nitrogen, for many measurements a drift in resistance was observed. This drift was assumed to be linear in time and subtracted accordingly, but

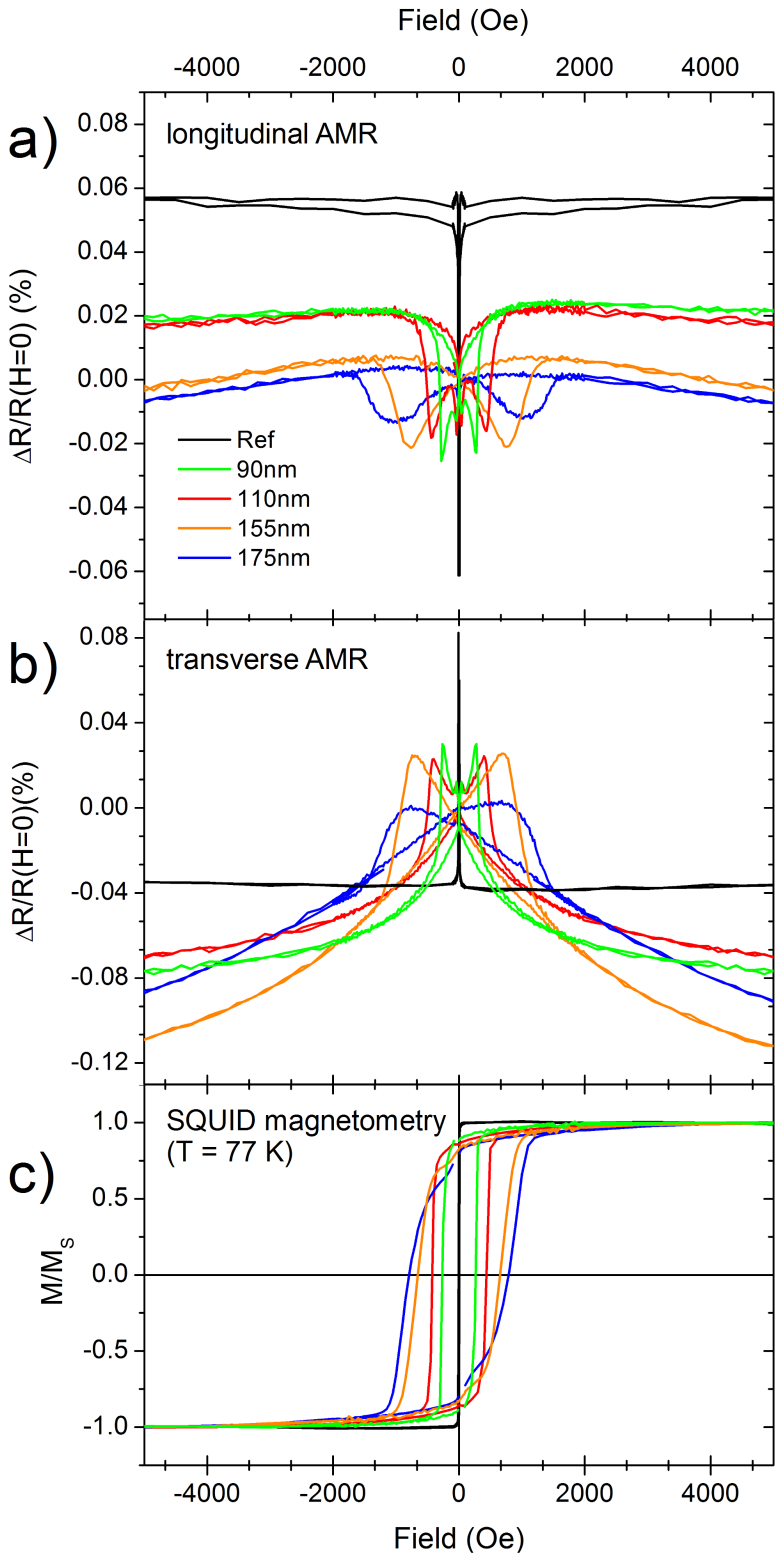

Figure 4.14: Normalized in-plane $R(H)$ curves for Fe antidot arrays with $a = 205\,\mathrm{nm}$, $t = 20\,\mathrm{nm}$ and varied d measured in longitudinal (a) and transverse (b) geometry. The magnetotransport curves are normalized on the resistance in remanence: $\Delta R/R(H_{ext} = 0)$. c) shows the results from SQUID magnetometry for the same set of samples. All measurements carried out at $T = 77\,\mathrm{K}$. The peaks/dips in the magnetotransport measurements are good indicators for the coercive fields.

for a few cases this approach did not yield the desired result with the drift corrected data not being perfectly symmetric.

Furthermore, a decrease in the dip / peak height is observed with increasing diameter: While the planar Fe reference film shows a overall change in electrical resistance of almost 0.12% over the hole field range in longitudinal measurement geometry, this reduces to merely 0.02% for the antidot array with $d = 175\,\mathrm{nm}$. As relative changes are plotted, this observation cannot be attributed to the fact that the effective sample cross section reduces with increasing hole diameter. Instead, one can consider this downward tendency in effect magnitude as further proof for the enhancement of the shape anisotropy induced by the holes. Larger holes increase this shape anisotropy, resulting in stronger constrictions on possible angles α between current density $\vec{j}$ and magnetization $\vec{M}$ and thus decrease $R = R_\perp + \Delta R \cos^2 \alpha$.

There is also a possible correlation between the peak / dip magnitude and the switching field distribution of the respective sample: As shown in Figure 4.2 in section 4.1.1, the switching field distribution for smaller d/a ratios is rather narrow, resulting in square-like hysteresis loops. For larger d/a ratios, a broadening of the switching field distribution is observed. If the broadening originates from different areas of the sample switching at different external fields, i.e. a spatial distribution of switching fields, this would decrease the AMR effect's magnitude. In that case, the magnetization would have turned by $180°$ in some areas, while in others it still points towards the original direction. For the AMR effect, both situations are equivalent. So, if the magnetization reversal within a sample is not synchronized in terms of field and space, the resulting AMR signal is not one sharp peak or dip, but one can imagine it as being the superposition of many small peaks connected to different switching fields.

4.3.2 Origin of the high-field slopes

In both longitudinal and transverse geometry, the magnetotransport curves exhibit a negative slope even in the high field regime $H_{ext} > 1000\,\mathrm{Oe}$. This slope is always larger in the transverse case. Such kind of behavior is reported in several contributions dedicated to the magnetotransport properties of square [145, 146] as well as of hexagonal antidot arrays [131, 147]. However, thus far, no explanation for its occurrence has been given.
First of all, one should exclude other magnetoresistive effects than AMR as the origin of these slopes. A decreasing resistivity with increasing field is also expected from the so-called "negative magnetoresistive effect" as described by Mott [39]. This effect appears in every ferromagnet. However, it cannot be responsible for the observed signal, as the neg-

ative magnetoresistance is isotropic, i.e. does not depend on the direction of the applied magnetic field with respect to the current. Further support for this argument is the fact that such a slope is not observed for the reference film.

With other magnetoresistive effects excluded, the signal has its origin most probably in the AMR effect and the high-field slopes can be attributed to the shape anisotropy of the holes, which works against the external field forcing the magnetization to point into the holes. Obviously, the available $5000\,\mathrm{Oe}$ are not sufficient to saturate either of the investigated antidot arrays. This approach also explains why the slope rises with larger antidot diameters - as a result of the larger shape anisotropy originating from larger holes. However, it does not explain why generally larger slopes are observed in the transverse cases.

Such kind of AMR behavior is also reported for magnetic nanowires, for example in the work of Dumpich et al. [148]. These wires have a strong uni-axial shape anisotropy. When the field is applied along their long axis, the magnetization is easily saturated and no high-field slope can be observed. The opposite is true for the field applied perpendicular to that direction: The magnetization follows the field only reluctantly due to large demagnetizing fields, and the angle between magnetization and current changes for fields larger than $10\,\mathrm{kOe}$.

In order to find the cause of the generally larger signal magnitudes in transverse geometry in the hexagonal antidot arrays, one needs to consider the inhomogeneous current density distribution $\vec{j}(\vec{r})$ as well as the intrinsic domain patterns $\vec{M}(\vec{r})$ from the previous section (4.2). $\vec{j}(\vec{r})$ can be calculated with help of the public domain software IDC2D [149] for any given 2-dimensional geometry. In Figure 4.15, the color-code represents the absolut value of current density distribution $|\vec{j}(\vec{r})|$ in a hexagonal antidot geometry with $d/a = 0.5$. Black color stands for a zero current density, bright yellow spots correspond to maximum current density. The electrodes are in gray color and extend over the whole width of the sample to mimic experimental conditions. IDC2D calculates the current density distribution for the boundary condition of a constant voltage between the electrodes. For the present example the voltage was applied parallel to a nearest neighbor direction of the antidot array - discussion of other geometries, which all occur within the characterized 2×0.5 mm^2 large segment of the antidot array (see Figure 3.1) due to the multitude of antidot lattice orientations, would follow similar arguments.

The holes periodically modulate the current density distribution: While the sample areas in between neighboring holes along the net current direction are almost completely current free ($< 5\,\%\ j_{max}$), other areas carry the majority of the current. This effect will be reflected in a transport measurement, as changes of the local resistivity at sample positions which are geometrically shadowed from current will not affect the overall resistance, at least as

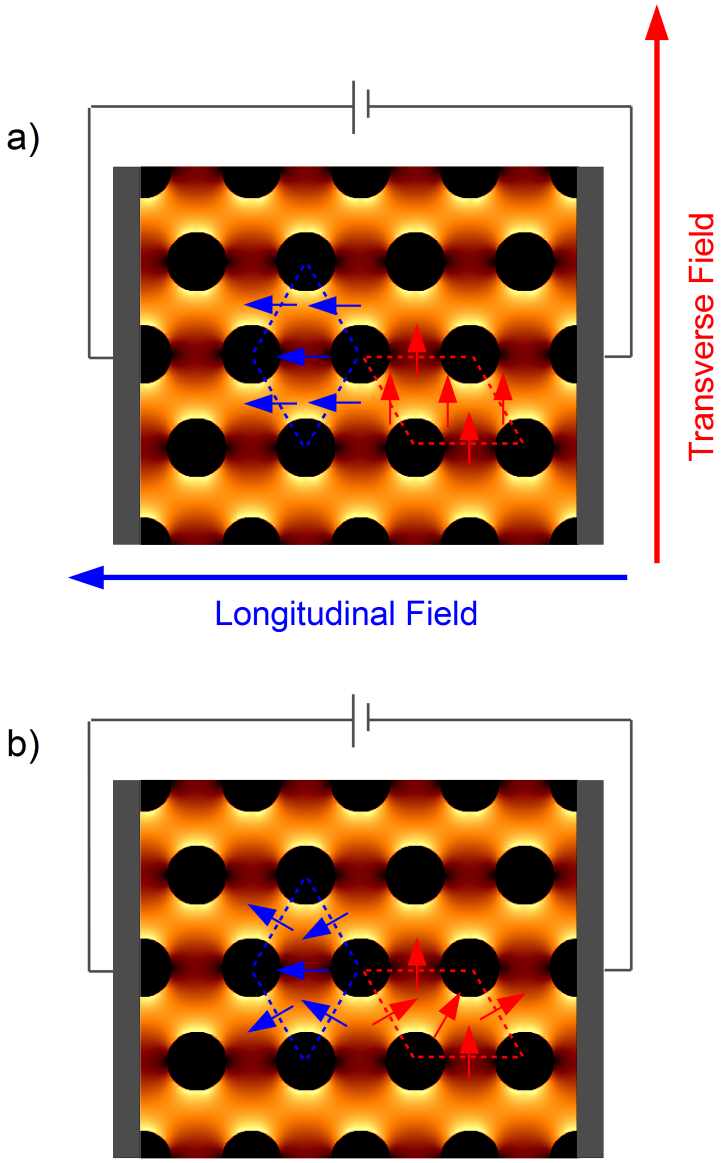

Figure 4.15: Schematics of different AMR-scenarios in an antidot array with $d/a = 0.5$. A constant voltage is applied between left and right electrode, the color code represents $|\vec{j}(\vec{r})|$ (black = no current, bright yellow = maximum current). Additionally, the magnetization directions in saturation (a) and remanence (b) are included for longitudinal (blue arrows) and transverse (red arrows) measurement geometry.

long as these changes in resistivity are relatively small. This condition is well fulfilled in the present case: the resistance of the reference film changes from $R_{\parallel} = 134.276\,\Omega$ for a magnetization parallel to the current to $R_{\perp} = 134.711\,\Omega$ for a magnetization perpendicular to that direction. As these are the extreme cases of the AMR effect, it can be deduced that the local resistivity $\rho(\vec{r})$ does not change by more than 0.324 %. Hence, in a first approximation one can restrict the discussion on the magnetization within the areas with a high current density.

In addition to the current density distribution, Figure 4.15 a) contains the magnetization configuration within a primitive unit cell of the antidot lattice for longitudinal (blue arrows) and transverse (red arrows) measurement geometries in saturation, while b) shows the resulting remanent states for the two cases. In saturation, the magnetization encloses angles of $0°$ and $90°$ with the net current direction for longitudinal and transverse case, respectively. In remanence, for both the longitudinal and the transverse case, it comes to formation of five magnetic domains within a unit cell of the antidot lattice. Their orientation is dependent on the direction of the saturating field and is discussed in section 4.2 in more detail. For longitudinal geometry, the maximum change in magnetization angle from saturation to remanence is $\pm 30°$. For the transverse case, however, one observes changes of $0°$, $30°$ and even $60°$. This larger change in magnetization angle becomes amplified in the measured AMR signal by the fact that two of the five domains of the primitive unit cell undergo this $60°$ change, both of which are located within sample areas of high current density and thus have significant weight in the magnetotransport signal, while the two domains which remain aligned with the saturating fields direction are located within sample areas which only carry a comparably low current. Under the assumption that the current still is mostly parallel to the net current direction (which is true for small antidots), a rotation by $30°$ and $60°$ leads to a change in $\cos^2 \alpha$ of 0.25 and 0.75 respectively. One can thus understand the much larger AMR signal magnitude and high-field-slope in transverse geometry. In order to quantify these statements, the exact magnetization from micromagnetic simulations has to be correlated with the calculated current density distribution. For one example geometry, this approach will be demonstrated in Section 4.4.

4.3.3 Summary

Magnetotransport measurements are suitable to characterize the magnetization reversal process of antidot arrays. Comparison with results from SQUID magnetometry shows that peaks / dips in AMR curves are good measures for the coercivity of the antidot arrays. Increasing shape anisotropy resulting from larger antidots is reflected by smaller peak / dip magnitude in magnetotransport measurements. The larger signal magnitudes in the transverse measurement geometry are a testament of the intrinsic domain structure as well as of the inhomogeneous current density distribution induced by the antidots. These features commonly appear in antidot arrays, but thus far have not been addressed [131, 145, 146, 147].

As opposed to conventional magnetometry, this makes magnetoresistance a probe for the magnetization which does not weigh all elements of a sample equally, but is sensitive in the

first place to changes in the magnetization in parts of the sample which carry the majority of the electrical current.

4.4 Easy and Hard Axis Magnetization reversal for small d/a ratio

In Section 4.2, an intrinsic domain structure in antidot arrays was found. The symmetry axis of these patterns, and thus the average magnetization direction, always stands in close relation with the crystallographic orientations within the antidot lattice: while for samples with large d/a ratio, the average magnetization relaxes into a next nearest neighbor (nnn) direction, this becomes the nearest neighbor (nn) direction for smaller d/a ratios, almost independent on the direction of the initially applied field. In other words, there should be an in-plane anisotropy in magnetic properties rising from the hexagonal arrangement of holes. This section is dedicated to characterize this anisotropy for an antidot array below the critical d/a ratio of 0.7.

As stated before, an in-plane anisotropy is not resolvable by neither SQUID magnetometry nor by the magnetotransport measurements presented in the previous section. This common problem [129, 147, 150, 151] is a result of the self-assembly approach of the preparation process, which typically yields crystallites of perfect antidot order of up to $25 \times 25\,\mu\mathrm{m}^2$ which are randomly oriented relative to each other, while the overall sample size characterized by integral magnetometry is in the range of several mm^2. As a consequence, it comes to orientational averaging.

However, it turned out that slight alterations in the sample setup which is described in section 3.2.1 allow to probe the magnetization reversal process in antidot arrays locally, i.e. within a single crystallite of the antidot lattice of defined orientation, by means of magnetotransport measurement. This is achieved by channeling the electrical current through a narrow constriction which only extends over such a single crystallite. These channels are created by focused ion beam (FIB) milling.

In the following, the results of the magnetotransport experiments are presented. Additionally, within a collaboration of project D6 of the Kompetenznetz Funktionelle Nanostrukturen of the Baden-Wuerttemberg Stiftung, Andreas Wallucks and Kristof Lebecki from the University of Konstanz (AG Nowak) conducted micromagnetic simulations of the system and, more importantly, calculated the AMR-response on the basis of these simulations. Likewise within this collaboration, Joachim Graefe from Max Planck Institute for Intelligent Systems contributed magneto optical characterization of the sample. The results presented in this section led to a publication [152] in *Nanotechnology*. With the permission of IOP publishing, parts of this article are adopted in the following.

4.4.1 Modified Sample Setup

The modifications to the original sample and measurement setup, as described in Section 3.2.1, are illustrated in Figure 4.16. On the $5 \times 10\,\mathrm{mm}^2$ large silicon oxide substrate, the actual antidot array extends over an area of $0.5 \times 6\,\mathrm{mm}^2$ (red rectangle in the Figure). The antidot array has an Fe film thickness of $t = 20\,\mathrm{nm}$, lattice parameter of $a = 200\,\mathrm{nm}$ and a hole diameter of $d = 100\,\mathrm{nm}$. Two of the outer contacts serve as electrodes. The maximum probing current for the FIB structured samples was set to $10\,\mu\mathrm{A}$ in order to prevent damage. As opposed to the previous experiment, the middle contact is now connected and separates the antidot array in halves, allowing to conduct two independent four-point resistance measurements simultaneously [152].

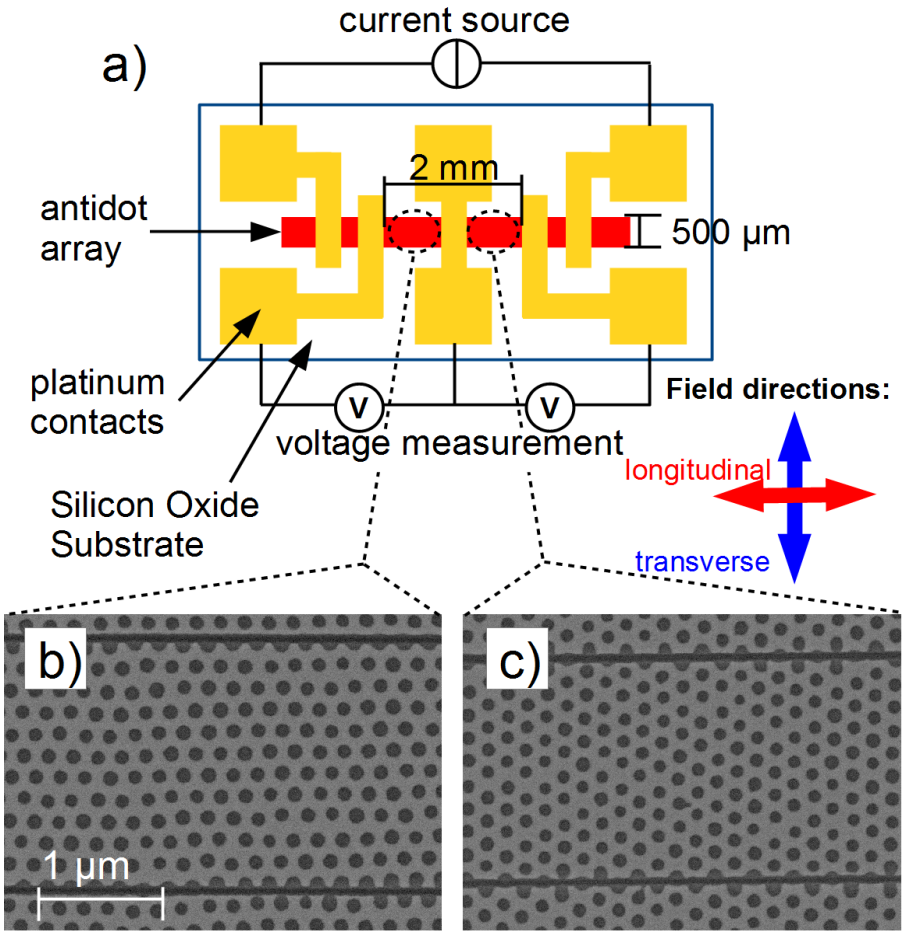

Figure 4.16: a) Schematics of the sample geometry for AMR measurements. The red and blue arrows indicate the direction of the magnetic field for longitudinal and transverse geometries, respectively. SEM images show the $20\,\mathrm{nm}$ thick Fe antidot array ($a = 200\,\mathrm{nm}$, $d = 100\,\mathrm{nm}$) with FIB-milled cuts (dark lines) along the nearest neighbor (b) and along the next nearest neighbor direction (c). Figure adopted from [152].

Within each half of the antidot array, an antidot crystallite of sufficient size and suitable orientation was searched with help of the Scanning Electron Microscope which is integrated in the FIB device (Zeiss NVision 40 SEM/FIB). The size of the chosen crystallite is critical as it directly determines the length of the FIB milled channel, and thus, the ratio between the electrical resistance originating from this channel and the one originating from the surrounding. In order to actually create a local probe for the magnetization, this ratio should be as high as possible. In order to find sufficiently large crystallites, the SEM was operated in a low magnification mode (magnification ≤ 1000), in which the antidots itself cannot be resolved. However, with this low magnification the scanning process leads to formation of Moiré patterns, which reveal the crystallites on a large scale. This is shown in Figure 4.17.

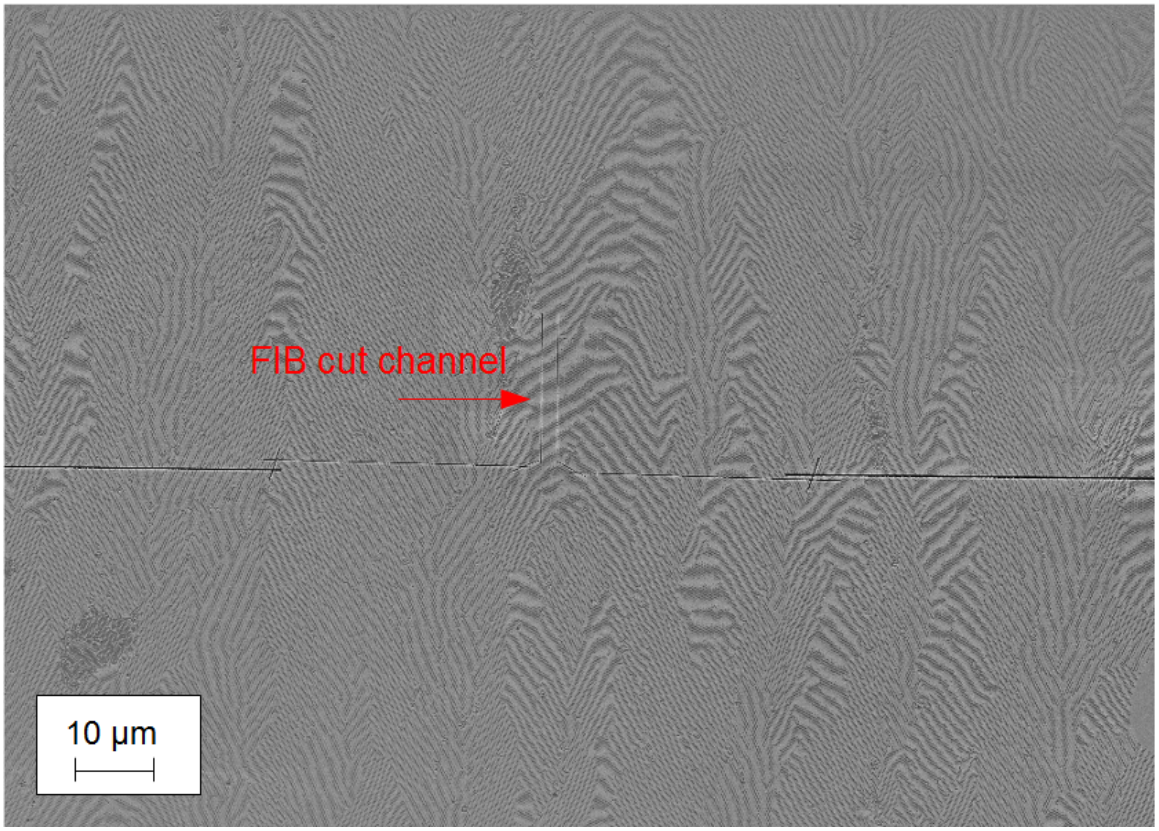

Figure 4.17: SEM Image of one of the channels and its surrounding. In this low magnification image, Moiré patterns resulting from the antidot arrays become visible. These patterns greatly facilitated the search for crystallites of suitable size for the subsequent FIB milling. The image was recorded with a acceleration voltage of $5\,\mathrm{kV}$.

The criteria for the crystallites' orientation was that one of the outstanding antidot crystal axis, i.e. either nearest neighbor (nn) or next nearest neighbor (nnn) direction, is aligned parallel to the net current direction. The approximately $60\,\mathrm{nm}$ wide and $20\,\mu\mathrm{m}$ long cuttings were performed using Ga^+ ions with a current of $10\,\mathrm{nA}$ for a exposure time of 9 minutes, each. Figure 4.16 shows the channels resulting from the FIB milling: in (b) the current is

directed along the nearest neighbor direction, in (c) along the next nearest neighbor direction. Both channels have a width of below $2.5\,\mu\mathrm{m}$ and a length of $20\,\mu\mathrm{m}$, thus enveloping more than 1000 well ordered antidots, each. The FIB-processing has the desired effect on the electrical resistance: Due to the small width and sufficient length ($2.5 \times 20\,\mu\mathrm{m}^2$ compared to pre-cut dimensions of $1 \times 0.5\,\mathrm{mm}^2$) of the FIB-cut channels, the electrical resistance of each half of the sample is increased to $420\,\Omega$ as compared to a value of $68\,\Omega$ prior to cutting. Thus, more than 80% of the magneto-transport signal originate from FIB-cut regions.

4.4.2 Setup of micromagnetic simulations

As described in [152], the group in Konstanz uses the widely spread OOMMF package for the simulations [112] of the magnetization reversal processes. The channels along nn- and nnn-directions are modeled as bars with a length of $8\,\mu\mathrm{m}$, width of $2\,\mu\mathrm{m}$ and thickness of $20\,\mathrm{nm}$. Reduction of the length is done to reduce computation time. The bulk magnetic properties of Fe were used: saturation magnetization $M_S = 1.7\,\mathrm{MA/m}$, exchange constant $A = 21\,\mathrm{pJ/m}$ and cubic anisotropy constant $K = 48\,\mathrm{kJ/m}^3$. The polycrystallinity of the Fe films is incorporated by random anisotropy axes for each anisotropy-crystallite. These crystallites were modeled as rectangular prisms having size $10 \times 10 \times 20\,\mathrm{nm}^3$. The mesh size ($2 \times 2 \times 10\,\mathrm{nm}^3$, i.e. two layers in the out-of-plane direction) is chosen to avoid large angles between magnetization vectors in neighboring cells [153]. The experimentally observed non-perfect antidot structure is mimicked by arbitrary variations of antidot diameters and positions of $\pm 5\%$. Although the experimental AMR signal originates mostly from the $2.5 \times 20\,\mu\mathrm{m}^2$ large channels, the magnetization within these regions is influenced by the surrounding magnetic material via long range dipolar interactions. This can be seen from the results in Figure 4.18, where no extra shape anisotropy resulting from the channel itself can be observed and the shifts in coercivity seem to be solely connected to the lattice orientation (this will be discussed later in more detail). However, in previous simulations, it was found that the shape anisotropy rising from the channel itself was not negligible [154]. Therefore, the surrounding magnetic material supposedly cancels this shape anisotropy. To include this observation in the simulations, an additional “artificial” uniaxial anisotropy that cancels out the $8 \times 2\,\mu\mathrm{m}^2$ shape anisotropy was added.

Domain nucleation plays an important role in the present scenario: The sample edge roughness is taken into account — simulated long edges ($8\,\mu\mathrm{m}$ long) are not perfect, the upper edge is placed roughly in the middle of the holes, while we positioned the lower one roughly between two rows of antidots as can be seen in Figure 4.19 b). Thus, all possible nucleation scenarios resulting from the different kinds of edges are considered.

Experimental results are directly affected by the nucleations on the long edges, but also indirectly by the nucleations that might appear somewhere to the left and to the right of the measured $20\,\mu\mathrm{m}$ bar. Therefore, the presented results are calculated only for the central simulated square with a size of $2 \times 2\,\mu\mathrm{m}^2$. With this arrangement we model direct influence of the nucleations at the upper and the lower edge and indirect influence of the nucleations from the left and from the right.

To calculate the AMR signal from the simulated magnetization, the following procedure which is described in more detail in Ref [154] is performed: As a result of the antidot pattern, the current density distribution is inhomogeneous (see section 4.3.2). In a first step, this two-dimensional vector field $\vec{j}_0(\vec{r})$ is calculated by using the open source software IDC2D [149]. It shall be emphasized that this is done independently from the applied field or magnetization configuration at this stage. In the second step, this current distribution as well as the magnetization vector (separately for every applied field) is considered, and the local anisotropic magnetoresistance is calculated: $\rho_{AMR}(\vec{r}) = \Delta\rho \cos^2 \alpha(\vec{r}) = \sigma_{AMR}(\vec{r})^{-1}$ with α being the angle between the current density and the magnetization. In the third step, the total current density is calculated: $\vec{j}_{tot}(\vec{r}) = \sigma_{AMR}(\vec{r})\vec{E}_0 + \vec{j}_0$, where $\vec{E}_0$ is the electrical field which is not influenced by the AMR effect. This approximation is valid since the changes in resistivity due to magnetoresistance are very small. The fourth step consists of integrating the current density $\vec{j}_{tot}$ over a cross section in order to get the total current I_{tot}. In the last step, the total resistivity together with the AMR contribution, was deduced using I_{tot}, the applied voltage and Ohms law. The whole procedure, together with its approximations is described and tested in Ref. [154]. The simulations do not incorporate any temperature effect, i.e. mimic the behavior at $T = 0\,\mathrm{K}$.

4.4.3 Resolving Anisotropy by AMR measurement in FIB-selected crystallites

The experimental longitudinal and transverse AMR measurements at $T = 77\,\mathrm{K}$ for both the channels cut along nn- and nnn-directions are shown in Figure 4.18 a) and b), respectively. All curves are normalized to the resistance $R(H = 0)$ of the remanent state. As expected, the longitudinal curves (red) exhibit characteristic dips while peaks occur in the transverse geometry (blue) in accordance with the previous Section and as observed in many experiments before [145, 146]. From Section 4.3 it is known that the peaks / dips of the AMR curves are a good measure for the coercive field.

Here, the first important result shows up: The position of the peaks / dips, and thus the coercive field strongly depends on the field's direction, indicating that the suggested approach is suitable of resolving the in-plane anisotropy introduced by the antidot lattice [152].

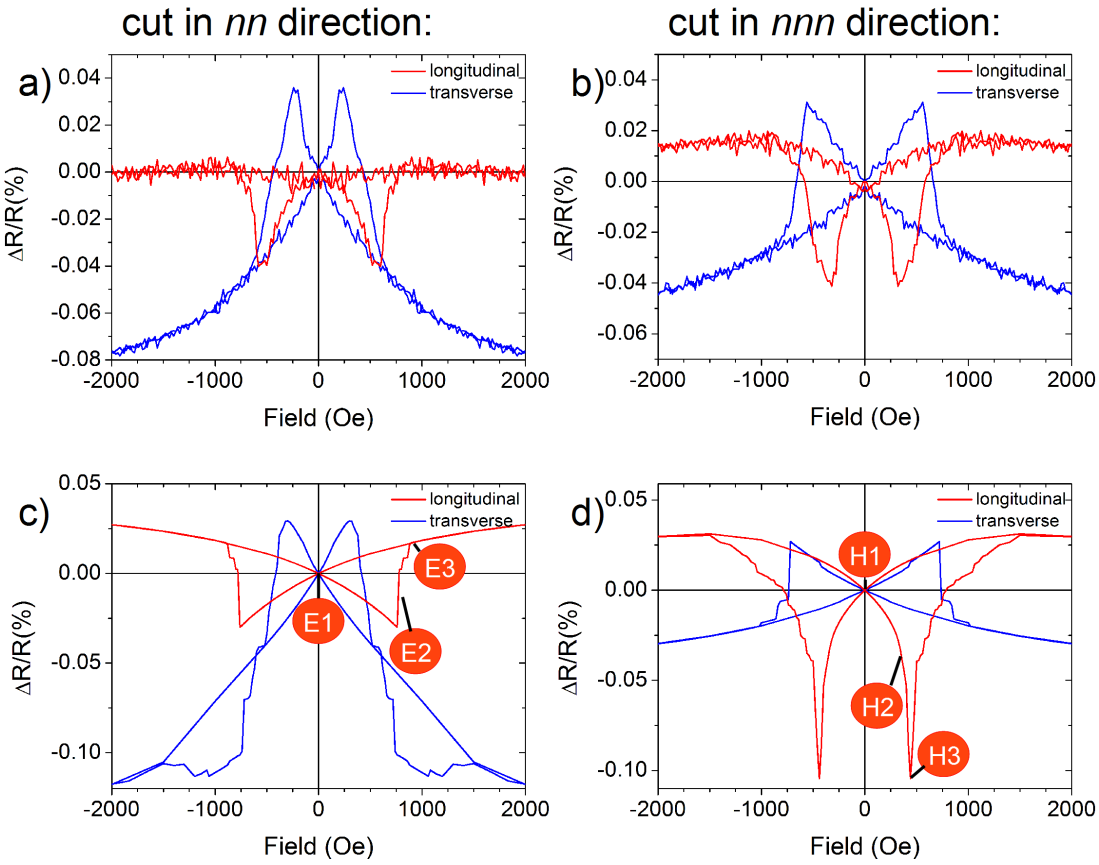

Figure 4.18: Measured AMR curves (a) for the current direction along nearest neighbors (nn) and (b) next nearest neighbor directions (nnn) in longitudinal (red) and transverse (blue) geometry of the external field at $T = 77\,\mathrm{K}$. Panels c) and d) present micromagnetic simulations of the corresponding geometries in identical color code. The red indicators in panel c) and d) mark significant points of AMR curves for easy (E) and hard axis (H) magnetic switching as shown in Figures 4.19 and 4.20. Figure adopted from [152].

For example, when FIB-cutting is applied along the nn-direction (Figure 4.18 a)), dips appear at $570\,\mathrm{Oe}$ while peaks are observed at $240\,\mathrm{Oe}$. This splitting of the coercive field can be directly linked to the relative orientation of the external magnetic field with respect to the orientation of the antidot lattice. For the channel cut in nn-direction, the longitudinal field orientation corresponds to the easy axis of the sample exhibiting the higher coercivity. On the other hand, the transverse geometry consequently means that the field is applied along the nnn-direction due to the hexagonal symmetry of antidots (cf. Figure 4.16). With its lower coercivity, this direction can be identified as the hard axis of the magnetization. Furthermore, it can be excluded that the observed shift in coercive fields is due to the channel's macroscopic shape. In that case, the easy axis always would be expected to be parallel to the long side of the bar shaped film. Contrary to this expectation, for the channel cut along the nnn-direction, the higher coercive field ($580\,\mathrm{Oe}$) is measured with the field applied perpendicular to the cut direction. This is again along a nn-direction of

the antidots (transverse AMR-curve in Figure 4.18 b)). This finding is also supported by angular-resolved MOKE measurements performed on the respective channels, where a sixfold symmetry of the coercive field is resolved (not shown).

The corresponding micromagnetic simulations of the AMR-experiments displayed in Figure 4.18 c) and d) show remarkable agreement with the experimentally observations in terms of the overall shape, the relative peak / dip positions and their magnitude for all four experimental geometries. The absolute values of the positions of the simulated peaks / dips, and thus the respective coercive fields, are approximately 20% larger than in the experimental curves. This, however, can be attributed to the experimental temperature of $T = 77\,\mathrm{K}$, while the simulations imply $T = 0\,\mathrm{K}$. The finding is also in good agreement with the temperature dependent magnetization reversal study presented in Section 4.1.4.

The detailed discussion of switching modes will be restricted to simulations and experiments in longitudinal geometry. Discussion of the transverse behavior follows similar arguments [152]. Inspection of the simulations in Figures 4.18 c) and 4.18 d) suggests that there are two distinct magnetization reversal mechanisms, dependent on whether the field is applied along the easy axis (nn-direction) or hard axis (nnn-direction). Some outstanding magnetic states in Figures 4.18 c) and 4.18 d) are indicated and will be referred to by the assigned labels ”easy” (E) and “hard” (H) in the following. Figures 4.19 a) and 4.20 a) show MFM results of the indicated states and the corresponding simulated magnetization patterns are presented in Figures 4.19 b) and 4.20b). Additionally, the angular distributions of spins were extracted from the simulations and can be found in Figures 4.19 c) and 4.20 c) for easy and hard axis reversal, respectively.

4.4.4 Easy Axis Reversal

First, the easy axis reversal mode shall be discussed, i.e. the field is applied in nn-direction. The remanent state (E1) is given by a periodic magnetization pattern in which each unit cell consists of 5 domains: one central domain with a magnetization pointing towards the nearest neighbor direction and 4 domains at an angle of $\pm 30^\circ$ with respect to the direction of the initially applied field as discussed in Section 4.2 and also in references [155, 156]. In the spin-angular distribution histograms (Figure 4.19c) this is reflected by the occurrence of 3 peaks at 180°, 150° and 210° [152]. This configuration is rather stable as implied by the high coercive field and is connected to a high resistance state in the AMR curve. This is expected considering the general AMR relation $R = R_\perp + \Delta R \cos^2 \alpha$ with α indicating the angle between current density and applied magnetization leading to $R = R_\perp + \Delta R$ for magnetizations approaching saturation. In MFM (Figure 4.19 a), a periodic arrangement

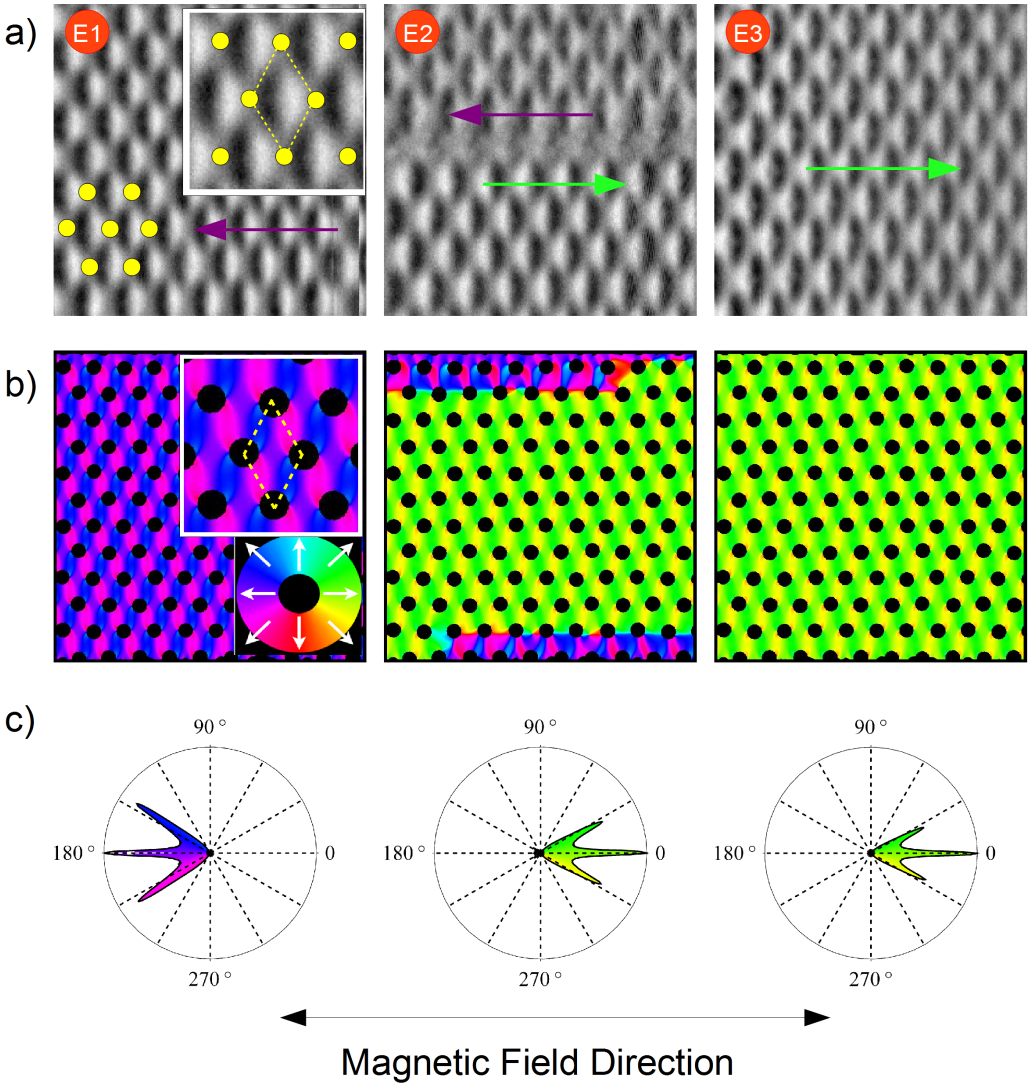

Figure 4.19: Easy Axis Magnetization Reversal. a) MFM images taken at the positions marked in Figure 4.18 c). The colored arrows indicate the local average magnetization direction. The insets give a magnified view with the dashed lines referring to the antidot lattice unit cell. b) Micromagnetic configuration obtained from the simulations. The histograms in c) show the angular orientation of magnetization for the snapshots of row b). Figure adopted from [152].

of rhombi can be seen in this state. The yellow dots give the antidot center positions and make clear that each rhombus belongs to a unit cell of the antidot lattice. The mirror axis of the rhombi (perpendicular to the black-white contrast) is a clear indication of the magnetization direction (see Section 4.2) - in the E1 state parallel to the initially negative saturating field, as illustrated by the red arrow in Figure 4.19 a).

An increasing positive reversal field applied (fields between states E1 and E2) in $0°$-direction results in a torque acting on the four tilted domains which initially enclosed an angle of $\pm 30°$ with the external field, giving rise to larger angles between magnetization

and the applied current. This is reflected in the AMR measurement as the resistance drops steadily in accordance with the above angular dependence. In this field regime, the changes in magnetization are reversible: Once the external field is turned off, the sample attains the state E1 again. Close to the coercive field, the stable domain structure breaks down (E2) in an irreversible process: in MFM (Figure 4.19 a)) as well as in the simulations (Figure 4.19 b)) reversed mesoscopic domains have nucleated and grown. Especially in MFM it is obvious that the local average magnetization points either in the original direction or is reversed by $180°$. These larger domains are separated by a mesoscopic domain wall with a width of one antidot lattice constant. For the AMR effect with its $\cos^2 \alpha$ dependence, both magnetization directions are almost equivalent (neglecting torque on the off-field domains caused by the applied magnetic field), which explains the comparatively small change of the AMR signal in this geometry [152]. The switching is complete when the original mesoscopic domain is no longer visible since completely reversed. In that case, again a strictly periodic magnetization pattern is obtained (E3), which is, however, inverse to the starting condition (E1). Finally, even larger external fields turn the four side domains in the direction of the external field and saturate the sample.

4.4.5 Hard Axis Reversal

The switching mode in nnn-direction (hard axis reversal), on the other hand, is characterized by a rotation of the magnetization via intermediate nearby easy axes [152]: As the field is reduced in the hard axis (H1), the magnetization relaxes again in a state very similar to the one obtained for the easy axis. The entire pattern, however, is rotated by $30°$ with respect to the direction of the initial field (Figures 4.20 a) and 4.20 b)), i.e. the central domain aligns to an easy direction (Figure 4.20 c)). Whether the tilt is $+30°$ or $-30°$ is determined by defects in the antidot lattice arrangement or by a slight misalignment of the external field with respect to the nn-direction. In fact, one can observe rotations in both directions in the simulations (five peaks instead of three are observed in the corresponding spin angular distribution), while the rotation in MFM experiments happens almost collectively.

Application of a counter field turns the magnetization out of the easy axis alignment (H2), as becomes clearly visible in Figure 4.20 c), where the average magnetization is found to be tilted by approximately $10°$ with respect to the remanent state (H1). In the corresponding MFM image (Figure 4.20 a)), the tilt of the magnetization can be seen as the symmetry of the rhombi is broken. This becomes clearer by comparing the higher magnified insets of the MFM images of states H1 and H2. Furthermore, the rotation is no longer collective: While the majority of the investigated sample section still exhibits a mean magnetization close to the $150°$ easy axis (blue arrow), the magnetization within a small stripe rotated into

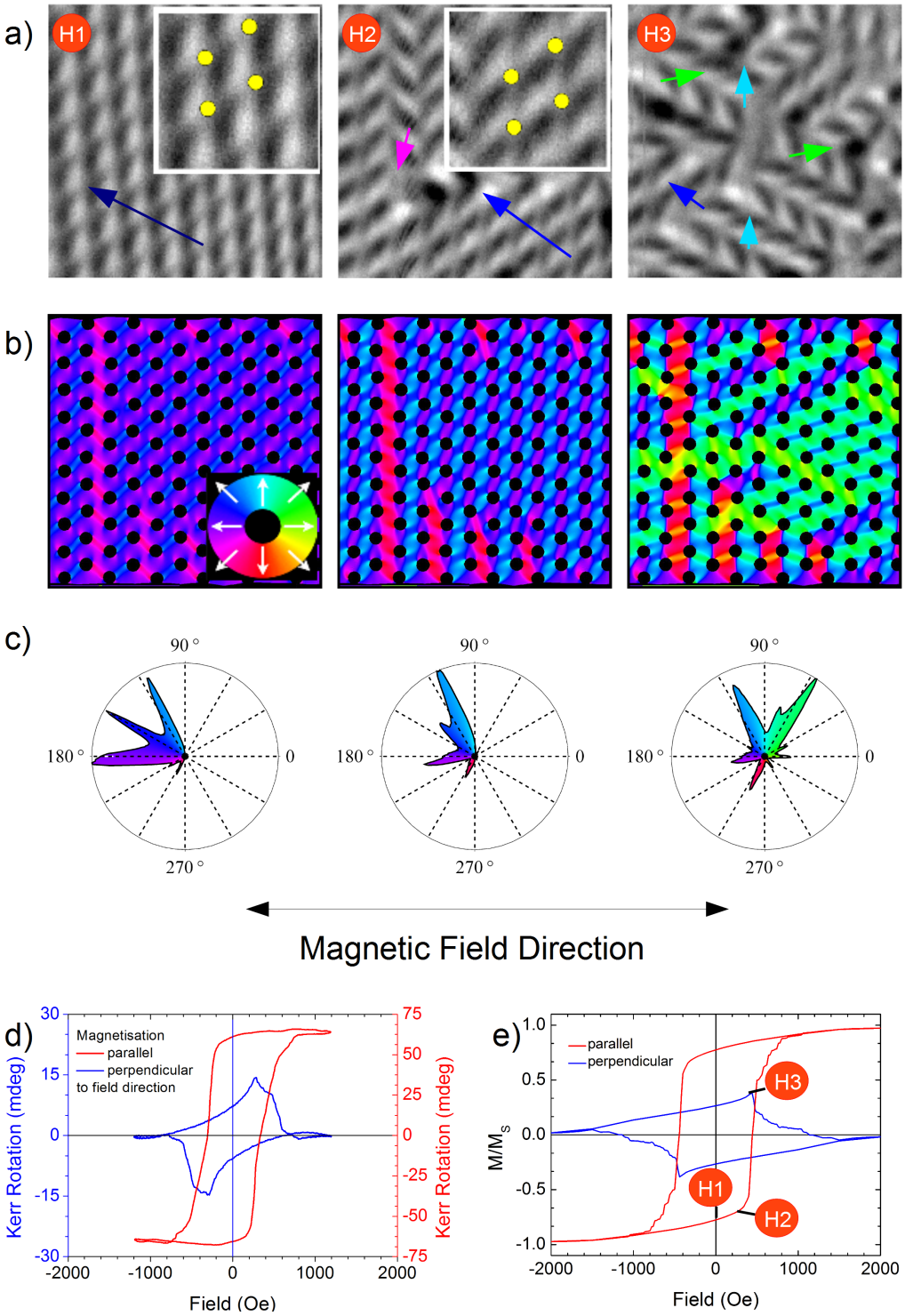

Figure 4.20: Hard Axis Magnetization Reversal. a) MFM images taken at the positions marked in Figure 4.18 d). The colored arrows indicate the local mean magnetization direction. The insets give a magnified view. b) Micromagnetic configuration obtained from the simulations. The histograms in c) show the angular orientation of magnetization for the snapshots of row b). d) Hysteresis Loops with the field applied along the next nearest neighbor (nnn) direction measured by KERR-Microscopy. The red curve shows the projection of the magnetization on the field direction, the blue curve represents the projection on the direction perpendicular to the applied field. e) shows the corresponding curves from the simulations. The occurrence of an off-field component is a clear indication for a rotation of the magnetization. Figure adopted from [152].

the $210°$ easy axis (pink arrow). The changes of the magnetization are reversible until the point where the rotation stops to be collective.

At the coercive field (state H3), both experiment (Figure 4.20 a)) and simulations (Figure4.20 b)) suggest that the magnetization splits into a multitude of mesoscopic domains, all of which showing a mean magnetization pointing close to one of the antidot lattice' easy axis. In MFM this is once again seen by means of the rhombi. Their symmetry axes, and thus their mean magnetization points towards the $150°$ (dark blue arrow), $90°$ (teal arrows) and the $30°$ (green arrows) easy axes. In the spin angular distributions which are derived from the simulations, one can observe three major peaks at $130°$, $100°$ and $65°$. These indicate that the majority of the sample's magnetization is in the $90°$ easy axis configuration which is distorted towards higher angles by the presence of the external field. In this configuration, the largest angles between the magnetization and the current flow directions are obtained, resulting in the minimum in the AMR curve [152]. Increasing the counter field further rotates the majority of the magnetization into the $30°$ easy axis configuration and eventually saturates the sample along the $0°$-direction (not shown).

Such a successive occupation of neighboring easy axis ($150°$ -> $90°$ -> $30°$) in the course of the magnetization reversal was also found in the work of Manzin et al. [5], where hexagonal Permalloy antidot arrays were studied by micromagnetic simulations under application of periodic boundary conditions. However, this kind of idealization leads to a fully collective rotation of the magnetization without the formation of mesoscopic domains, which we could find in our experiment.

Many features of the of the reversal process discussed here were also found in the investigation of epitaxial bcc Fe thin films on GaAs by Gu et al. [157, 158], where for the field swept along the [110] crystallographic direction (hard axis), the magnetization also relaxes coherently into one of the nearest easy axis (e.g. [100] direction) at first, similarly followed by nucleation of domains occupying the easy axis enclosing smaller angles with the subsequently applied reversal field. While in case of the epitaxial film, the mechanism is determined by the magnetocrystalline anisotropy, in case of the antidot array this is replaced by a periodic modulation of shape anisotropy, once again underlining the analogy between phenomena on the atomic and the mesoscopic length scale.

The rotational reversal mechanism also shows a distinct signature in MOKE-Microscopy, which was applied on the channel in nnn-direction with the field direction parallel to the channel. Figure 4.20 d)) presents the magnetic hysteresis loops projected on the field axis (red) and perpendicular to the field axis (blue), while Figure 4.20 e)) is the result from the corresponding simulation. As the external field is reduced, an off-field component is detected, indicating that the overall magnetization begins to rotate as predicted by the sim-

ulations (H1) [152]. Further increase of the counter field increases this off-field component (H2) until it reaches a peak (H3). For larger external fields the off-axis component vanishes continuously as the magnetization approaches saturation.

4.4.6 Summary

The magnetic switching modes in a self assembled hexagonal antidot array with a d/a ratio of 0.5 in nearest neighbor (nn) and next nearest neighbor (nnn) lattice directions was investigated by AMR, MFM and MOKE-Microscopy and corresponding micromagnetic simulations. By FIB cutting, the previously integral magnetotransport measurement was modified into a local probe for the magnetization in a single crystallite of the self-assembled antidot lattice. These crystallites exhibit the expected 6-fold symmetry induced by the hexagonally ordered antidots. The coercive field of the Fe antidot array with $a = 200\,\mathrm{nm}$, $d = 100\,\mathrm{nm}$ and $t = 20\,\mathrm{nm}$ is $570\,\mathrm{Oe}$ for the easy axis and $240\,\mathrm{Oe}$ for the hard axis at a temperature of $T = 77\,\mathrm{K}$. These values are not influenced by the shape anisotropy of the FIB-cut channel. Micromagnetic simulations and MFM show two distinct reversal modes: In the nn-direction (easy axis), the sample's magnetization is stable almost up to the coercive field. In this field regime, the magnetization undergoes reversible changes and the original remanent state can be re-attained by switching off the external field. Then, irreversible nucleation and growth of 180° reversed mesoscopic domains sets in. The mesoscopic domain walls are clearly pinned by the antidot lattice.
In the nnn-direction (hard axis), the switching mode differs significantly. In this case micromagnetic simulations suggest a reversal mode in which the mean magnetization jumps from one easy direction to the next until the magnetization is driven in the direction of the external field. Contrary to previous results from simulations using periodic boundary conditions [5], where this rotation happens coherently, the sample splits up into smaller domains in the experiment. In an additional MOKE microscopy investigation, such behavior is indicated by a peak in the off-axis magnetization component [152].

4.5 Magnetization reversal for large d/a ratio

This section is dedicated to the characterization of the magnetization reversal process in antidot arrays with a d/a ratio larger than 0.75. Firstly, the in-plane anisotropy of the magnetization reversal is probed by means of the FIB supported magnetotransport method described in the previous section. Afterwards, the focus is set to characterize the previously discussed (see section 4.2 “Intrinsic domain structure”) analogy of such antidot arrays to 2-dimensional honeycomb artificial spin-ice structures. Open questions are whether the magnetic bridges emerging in the antidot arrays show the Ising-spin like behavior not only in remanence, but also during the reversal. Furthermore, literature reports a reversal process which is driven by separation of magnetic charge along 1-dimensional paths [12] for honeycomb spin-ice. In analogy to the infinitesimal flux tubes connecting two magnetic monopoles of opposite sign in the theoretical work of Paul Dirac [11], these paths are commonly referred as “Dirac” strings. In this context it is also of interest whether the so called ice-rules, i.e. “2-in-1-out” or “1-in-2-out” magnetic charge configurations at the vertices of three neighboring bridges apply during the entire magnetization process. These aspects of the antidot arrays are studied by means of micromagnetic simulations and X-ray photo emission electron microscopy (X-PEEM) and MFM.

4.5.1 In-plane anisotropy investigated by magnetotransport measurements and micromagnetic simulations

The simulated hysteresis curves of a Fe antidot array with lattice parameter $a = 200\,\mathrm{nm}$, hole diameter of $d = 175\,\mathrm{nm}$ and film thickness of $t = 5\,\mathrm{nm}$ in Figure 4.21, which correspond to different orientations of the magnetic field with respect to the antidot lattice , strongly differ in their shape and, thus indicate an in-plane anisotropy of the magnetization reversal: With a coercivity of $H_C = 1055\,\mathrm{Oe}$, the square-like hysteresis for the field applied along the nnn-direction (Figure 4.21 a)) is a clear indicator for a magnetic easy axis. In that case, the field is aligned parallel to the long (and thus, easy) axis of one of the emerging bar magnets (see inset of the Figure). A reduced remanence and a drop in coercivity to $H_C = 740\,\mathrm{Oe}$ identify the nn-direction as the hard axis (Figure 4.21 b)). In this configuration, the field is perpendicular to the long axis of one third of the bridges.

In order to resolve the predicted in-plane anisotropy of the magnetization reversal process experimentally, the same approach based on magnetotransport measurements on single FIB-selected crystallites of the antidot lattice as described in section 4.4 was followed. These crystallites were again chosen in a way that either the nn- or nnn-directions coincide with the net current direction. Figures 4.22 c) and e) show the approximately $220\,\mathrm{nm}$ wide

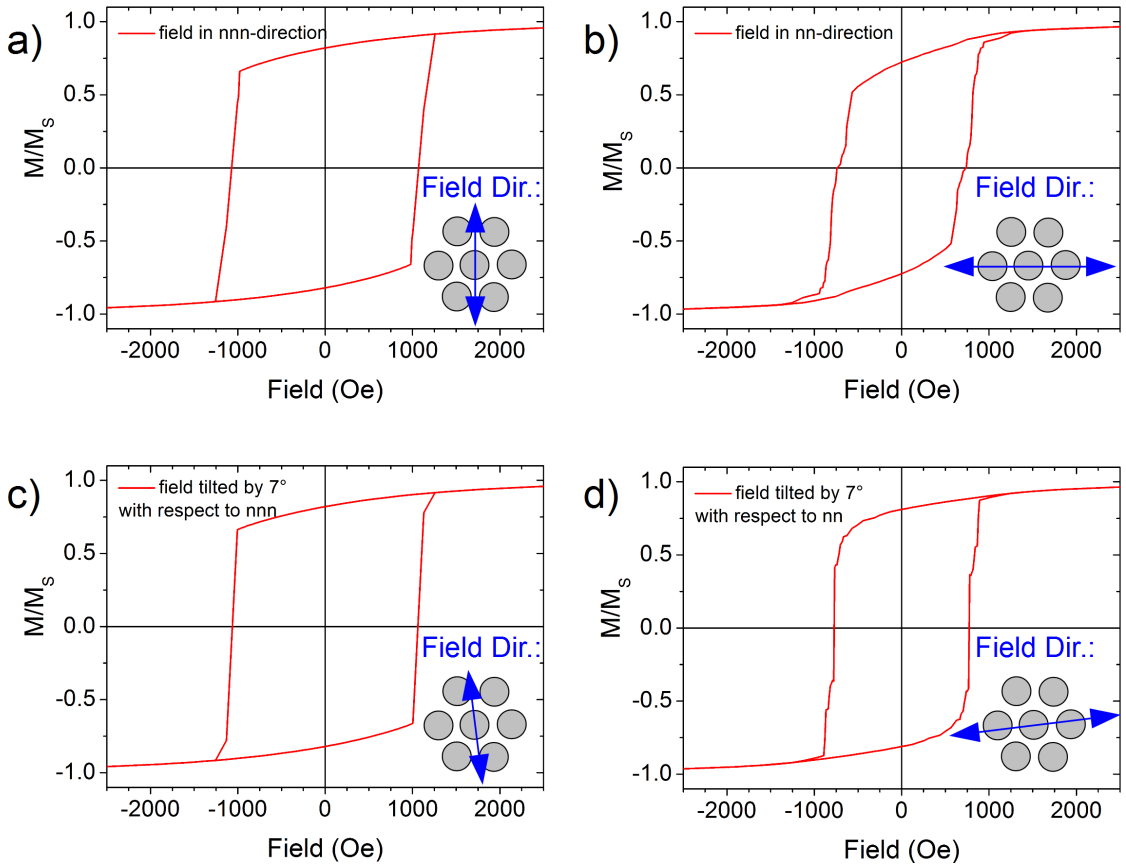

Figure 4.21: Simulated hysteresis loops for an antidot array with $a = 200\,\mathrm{nm}$, $d = 175\,\mathrm{nm}$ and $t = 5\,\mathrm{nm}$, with the magnetic field applied in different in-plane directions. In (a) the field is applied along the nnn direction, in (b) along the nn direction. In order to investigate the effect of non-perfect field alignment, in (c) and (d) there is an angle of $7°$ between field and nn- or nnn-direction, respectively (see insets of the respective graphs).

FIB cuts which channel the current through the two crystallites. The nn-channel is slightly miscut by approximately $4°$ with respect to the actual nearest neighbor direction. How this may affect the measurement will be discussed later. The Fe antidot array has a film thickness of $t = 20\,\mathrm{nm}$, lattice parameter of $200\,\mathrm{nm}$ and hole diameter of $d = 175\,\mathrm{nm}$, corresponding to a d/a-ratio of 0.875. Each of the emerging channels has a length of approximately $28\,\mu\mathrm{m}$ and a width of $2\,\mu\mathrm{m}$. The FIB processing increases the resistance of the sample side containing the cut along nn-direction from $R_{org} = 120\,\Omega$ to $R_{FIB} = 975\,\Omega$, and from $R_{org} = 97\,\Omega$ to $R_{FIB} = 818\,\Omega$ for the sample side containing the cut along nnn-direction. These values correspond to $(R_{FIB} - R_{org})/R_{FIB} > 88\%$ of the overall resistance of each half of the sample originate from the FIB-cut channels. The magnetotransport measurements were conducted with the samples in liquid nitrogen at $T = 77\,\mathrm{K}$ in order to provide constant temperature.

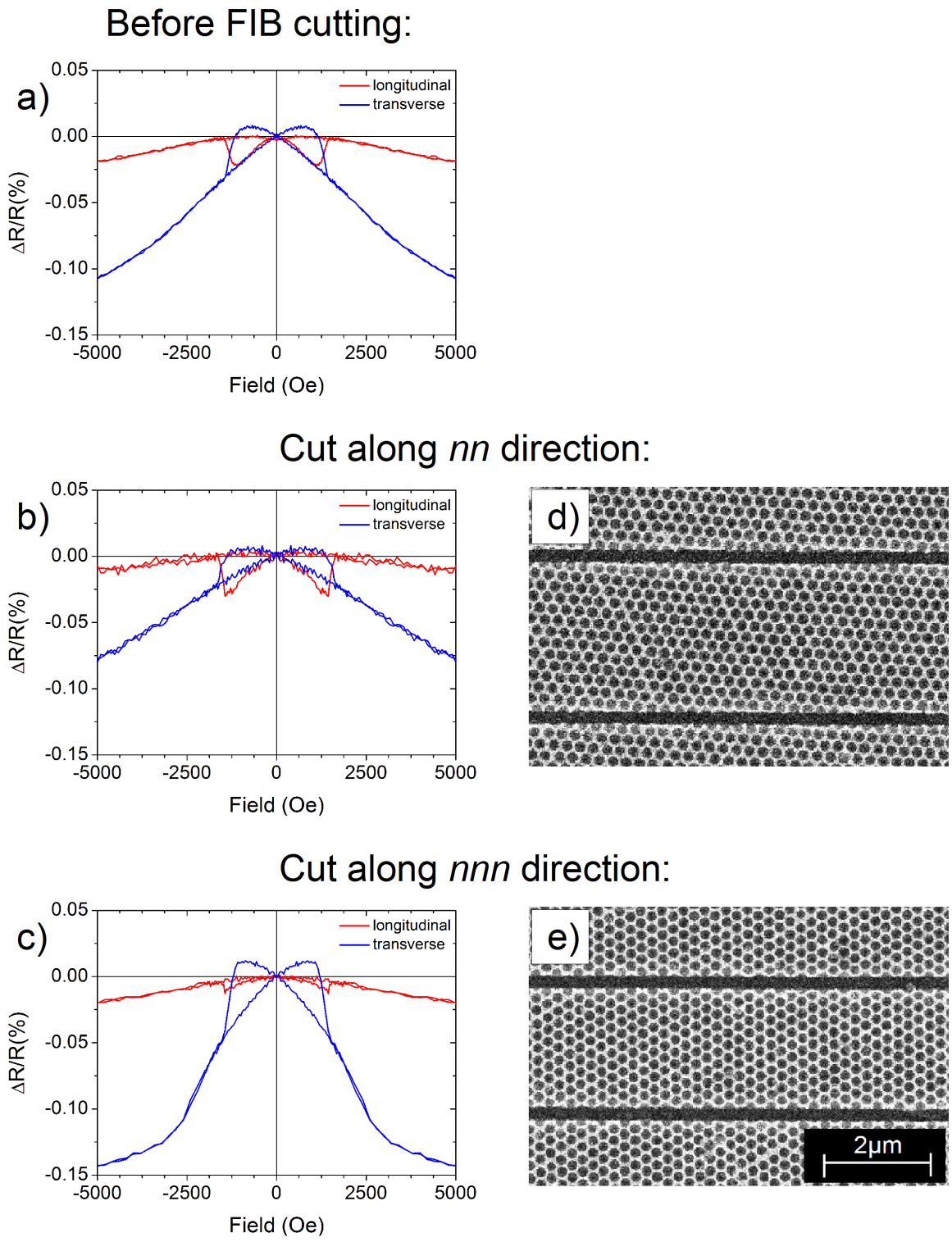

Figure 4.22: Longitudinal (red) and transverse (blue) AMR curves for a $20\,\mathrm{nm}$ thick Fe antidot array with $a = 200\,\mathrm{nm}$ and $d = 175\,\mathrm{nm}$ ($d/a = 0.875$) measured at $T = 77\,\mathrm{K}$. a) shows the results prior to the introduction of the FIB-cut channels. In b) and c) the results for channels cut along nn- and nnn-direction are presented, respectively. The SEM micrographs d) and e) show sections of the channels.

Figure 4.22 a) shows the normalized magnetotransport curves for longitudinal (red) and transverse measurement geometry with the sample in its original state (i.e. prior to FIB processing), while in b) and d) the curves for the channels cut along nn- and nnn-directions are displayed, respectively. A comparison between the three graphs shows a clear effect of the restriction of the measurement to a single crystallite. The originally broad peaks / dips are replaced by very sharp features for the FIB structured sample. In addition, the overall magnitude of the curves is strongly dependent on the respective orientation between current, field and antidot lattice now.
However, extraction of a direction dependence of the coercive fields by means of the peak / dip positions as it was presented in the previous section for antidot arrays with smaller d/a ratio is not so obvious in the present case: For both nn- and nnn-cut directions, the minimum of the longitudinal curves is observed at a field of $H = 1420\,\mathrm{Oe}$. While this poses a significant change compared to the position of the minimum prior to the FIB structuring ($H = 1120\,\mathrm{Oe}$), the finding that changing the field direction from nn- to nnn-orientation does not result in a shift in coercivity is unexpected. Especially for the present geometry with its large d/a ratio, due to the “bar magnets” emerging in between nearest neighbor holes, a very pronounced anisotropy is expected, as suggested in the simulated curves shown in Figure 4.21. Furthermore, the result cannot be explained by the miscut of the nn-channel, as the simulations suggest that even a miss-alignment of the field of 7° does not affect the coercivity in such a large degree as compared to a perfect alignment of the field in nn- or nnn-direction.

On the other hand, the peak positions of the transverse curves for nn- and nnn-cuts are clearly split: when the field is applied along the nn-direction (transverse field direction of the nnn-cut), the peak appears at $H = 1280\,\mathrm{Oe}$ as opposed to $H = 1080\,\mathrm{Oe}$ for the nnn-field direction (transverse field direction of the nn-cut). While this result indicates the nnn-direction of the antidot array as the easy axis, which is in agreement with the micromagnetic simulations, at this point no completely consistent picture of the anisotropy of the magnetization reversal can be drawn.

There is, however, more information to be extracted from the magnetotransport measurements than merely the anisotropy of the coercive field. For both cut directions, a larger signal magnitude is observed when the field is applied in the transverse direction as compared to the longitudinal case. An especially large difference emerges when the current is along the nnn-direction (Figure 4.22 c)), where the normalized resistivity changes by less than 0.025% in longitudinal and by more than 0.15% in the transverse case. For the nn-channel, this is 0.075% in transverse and 0.03% in longitudinal field direction. The principal difference between longitudinal and transverse AMR signal magnitude has been discussed

in section 4.3.2. Here, the difference between transverse AMR signal magnitude for the current in nn- and nnn-direction shall be addressed.

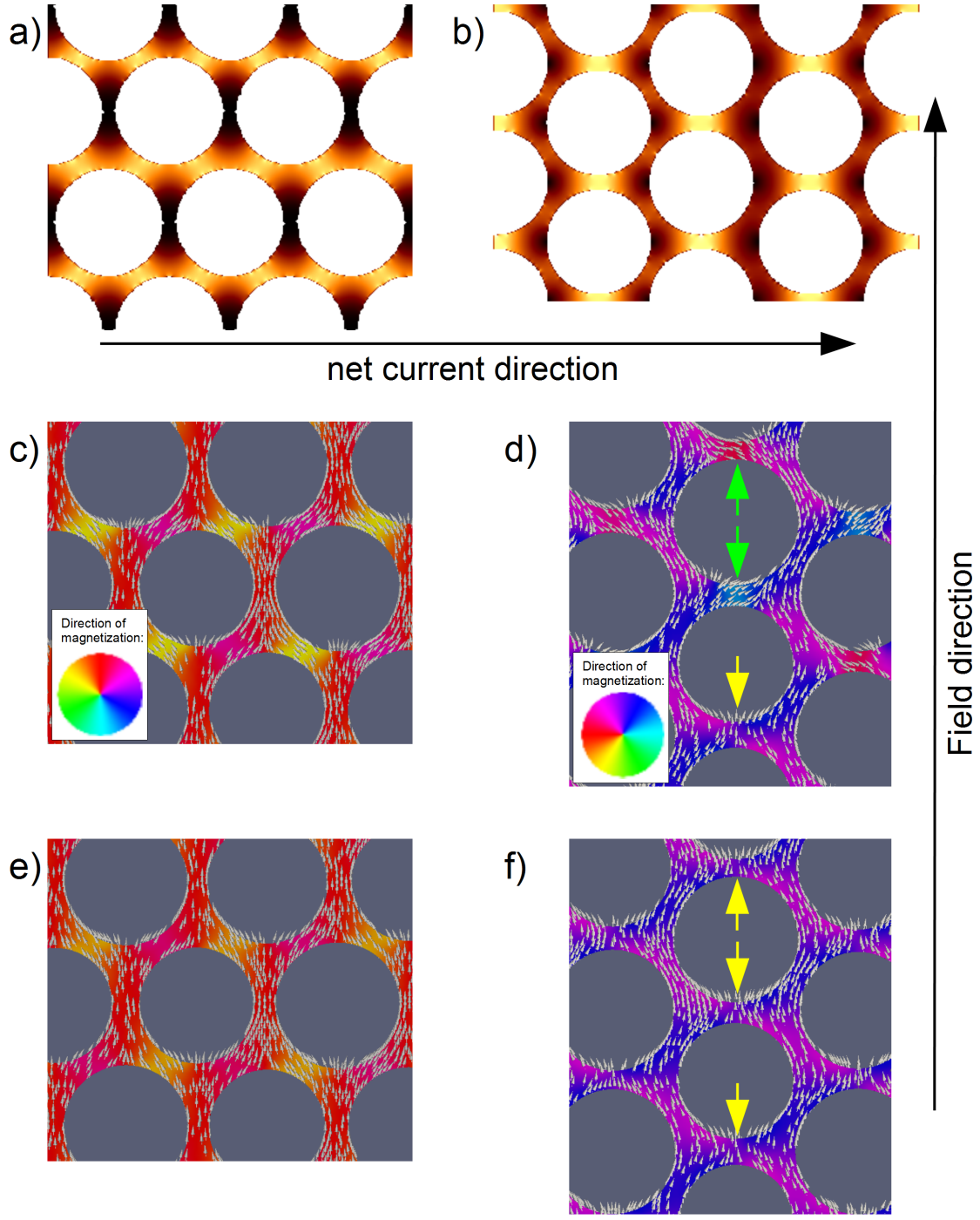

Figure 4.23: The origin of the difference in magnetotransport signal magnitude for current in nn- and nnn-directions (left vs. right column). Current density distributions as calculated by IDC2D for an antidot array with $a = 200\,\mathrm{nm}$, $d = 175\,\mathrm{nm}$ for current in (a) nn- and (b) nnn-direction. The brighter the color, the higher the current density. (c) and (d) show micromagnetic snapshots for an applied field of $H = 879\,\mathrm{Oe}$ along the indicated direction, while the field was increased to $H = 1758\,\mathrm{Oe}$ in (e) and (f) (see the simulated hysteresis loops in Figure 4.21). The green arrows mark positions which undergo a very large change in magnetization direction.

The larger transverse signal magnitude for the current in nn-direction is mainly due to a larger slope of this curve in the field range between 0 and $3000\,\mathrm{Oe}$. For higher fields, the slopes of transverse nn- and nnn-curves almost equal each other. Under incorporation of the inhomogeneous current density distribution resulting from the holes, and with the help of micromagnetic simulations, the differences of the slopes can be explained. The absolute values of the current density distributions for both current directions is shown in Figures 4.23 a) and b), respectively. The bright regions correspond to maximum current density, and a resistance measurement will be especially sensitive to changes in resistivity in these regions. Therefore, discussion will be focused on the evolution of the magnetization at these positions.

Figures 4.23 c) and e) exhibit snapshots from the micromagnetic simulation for an applied field of $H = 879\,\mathrm{Oe}$ and $H = 1758\,\mathrm{Oe}$ for the transverse case of a nn-current direction, so that the field is applied in nnn-direction. In the case of the smaller field, the magnetization vectors are mostly aligned parallel to their corresponding bar magnets, and the increase of the field simply tilts their direction towards the magnetic field. At the spots corresponding to maximum current density, the change in angle caused by the increasing field is approximately $20°$.

The situation for the transverse case of a nnn-current direction (i.e. the field is applied along the nn-direction) is more complex. At the positions carrying the majority of the current, which are indicated by arrows in the corresponding micromagnetic snapshots in Figures 4.23 d) and e), the magnetization undergoes a more fundamental change with increasing external fields. At a field of $H = 879\,\mathrm{Oe}$, the magnetization at most of the relevant positions shows a tendency to align parallel to the corresponding bar magnets, trying to minimize the stray field energy. These positions are marked by a green arrow. At the position marked by the yellow arrow, the external field has already induced a change in the domain structure. There, the domain pattern which was originally observed only for antidot arrays with small d/a ratios emerged (cf. discussion of Figure 4.13), so that there is now a domain between nearest neighbor holes with a magnetization pointing directly into the holes. The external field overcompensates the stray field which is created in this configuration.

If now the external field is increased, more and more of the relevant positions change their domain pattern, as indicated by the yellow arrows in Figure 4.23 f). These transitions are accompanied by a change of the magnetization's angle by more than $60°$. It is this large change in angle which causes the larger slope of the transverse signal in nnn-direction. Once all of the relevant positions have undergone this change, the slope reduces to almost the same value as observed in the transverse signal in nn-direction.

In terms of spin-ice, the presented magnetotransport curves give an indirect hint that the ice-rules are obeyed during the entire magnetization reversal. According to Tanaka et al., this can be deduced by the number of abrupt resistance changes during the magnetization reversal [119]: When the field is applied along the long axis of a bar magnet of a honeycomb spin-ice lattice, this implies that there are also bars which enclose angles of $\pm 60^\circ$ with the field. If each bar could switch independently, there should be two distinct switching fields: One for the bars parallel to the field and one for the $\pm 60^\circ$ bars, resulting in a total of two abrupt resistance changes. In the work of Tanaka et al., these features occur at fields of $800\,\mathrm{Oe}$ and $1100\,\mathrm{Oe}$, so that they are easily resolvable. However, in all the curves presented in Figure 4.22, only one such feature in the form of a peak or dip can be observed, indicating a strong coupling between neighboring bars which might be due to the ice-rules prohibiting the formation of $\pm 3q$ vertex charges. This interpretation is supported by micromagnetic simulations.

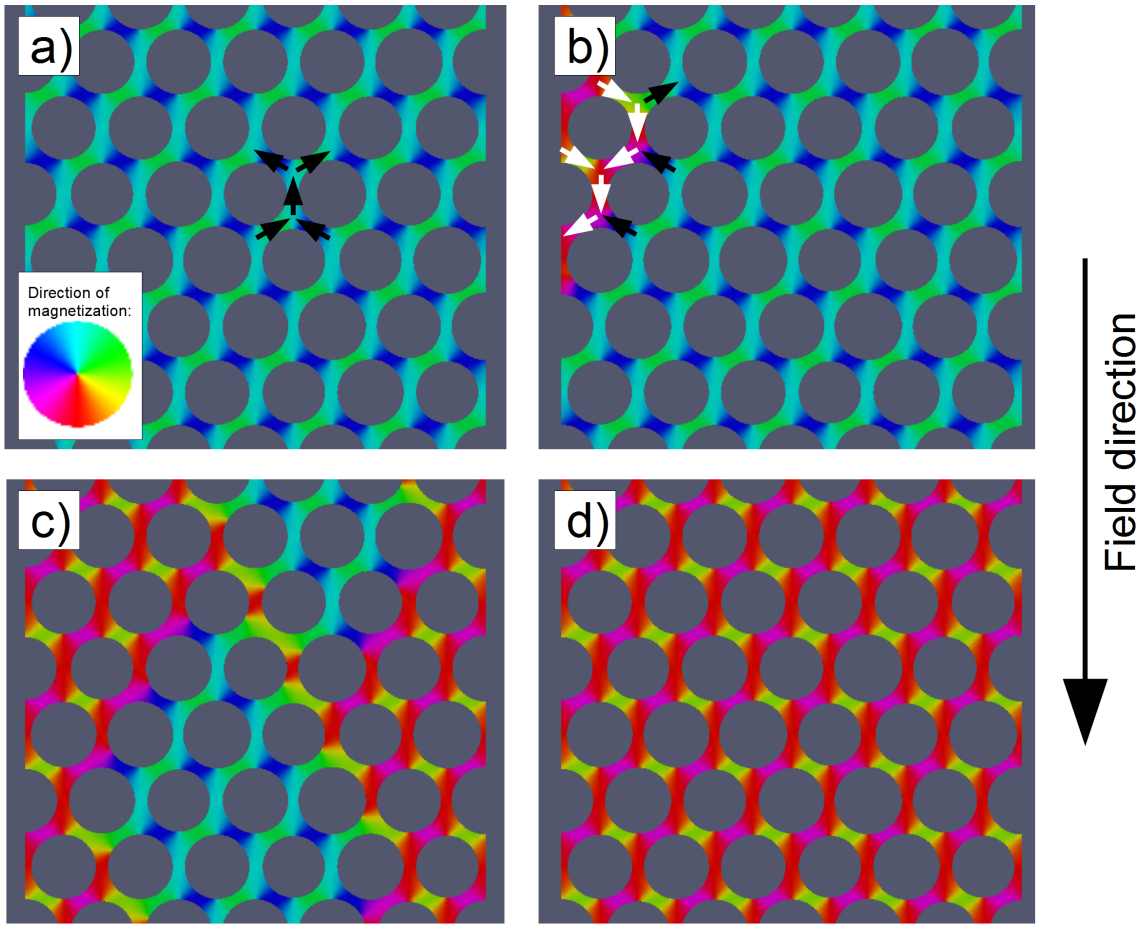

Figure 4.24: Snapshots from micromagnetic simulations of the magnetization reversal for an Fe antidot array with $a = 200\,\mathrm{nm}$ and $d = 175\,\mathrm{nm}$, with the field applied in the nnn-direction (easy axis). (a) is the remanent state, (b),(c) and (d) correspond to counter fields of $1004\,\mathrm{Oe}$, $1130\,\mathrm{Oe}$ and $1256\,\mathrm{Oe}$. Black arrows stand for the original magnetization direction of a bridge, while white arrows indicate reversed magnetization. The ice-rules apply at every vertex.

Figure 4.24 contains magnetization snapshots of the magnetization reversal for the field applied along the nnn-direction (easy axis) at different field stages. Image (a) shows the remanent state with a periodic magnetization pattern. Imaging of the vertex charges would identify this pattern as the charge ordered state, in which each vertex has a charge of $\pm q$, as discussed in section 4.2. At a counter field of $H = 1004\,\mathrm{Oe}$ (image (b)), a whole region of magnetic bars switches. Apart from border effects, this region is shaped in a way that no ice-rule violation emerges. A slight increase of the counter field to $H = 1130\,\mathrm{Oe}$ lets the region grow over the whole length of the simulated geometry. At the same time a second switched region nucleated. Again, both processes do not yield an ice-rule violation. Further increase of the external field to $H = 1256\,\mathrm{Oe}$ then completes the reversal (cf. hysteresis loop in Figure 4.21 (a)).

This simulated magnetization reversal for a field applied along the easy axis, characterized by a switching of whole regions, stands in contrast to the mechanisms observed in conventional spin-ice systems. For honeycomb spin-ice consisting of either magnetic islands [12] or connected wires [159], the magnetization reversal happens by separation of magnetic charge along 1-dimensional paths (see Figure 1.11). This difference could originate in a comparatively strong coupling between vertex sharing bars in the antidot spin-ice: Due to the curvature of the holes, the width of the bars reaches its maximum exactly at the vertex, so that - compared to the wire spin-ice - a larger portion of the magnetic material contributes to the interaction between bars. Another important result from the simulations is that the emerging magnetic bridges show the Ising spin-like behavior, i.e. they are single domain and their magnetization points along their long axis.

4.5.2 Investigation of the magnetization reversal by MFM and X-PEEM

For the experimental investigation of the magnetization reversal, X-PEEM and MFM were applied. Both systems provide in-situ magnetic fields, which are however restricted to approximately $500\,\mathrm{Oe}$ in the case of X-PEEM and $1000\,\mathrm{Oe}$ for MFM, so that above discussed Fe antidot array with a coercive field larger than $1280\,\mathrm{Oe}$ could not be investigated. Therefore, a Permalloy antidot array with a lattice constant of $a = 500\,\mathrm{nm}$ and a hole diameter of $d = 400\,\mathrm{nm}$ (d/a-ratio$= 0.8$) and a film thickness of $20\,\mathrm{nm}$ was prepared. The Pt coverlayer was restricted to approximately $1\,\mathrm{nm}$ in order not to obscure the magnetic film in the surface sensitive X-PEEM experiment. This antidot array has an average coercive field of $330\,\mathrm{Oe}$ ($T = 300\,\mathrm{K}$) and its major loop closes at $520\,\mathrm{Oe}$, so that it fits the experimental requirements.

MFM's sensitivity to magnetic charges makes it a valuable tool in the search for ice-rule violations, as these would result in a three times larger frequency shift than a vertex which obey the ice-rule. However, the information on the location of the magnetic charges does not yield a unique solution for the sample magnetization. For example, there are three possible magnetic configurations resulting in a $q_{vertex} = 1q$ vertex state (cf. Equation 4.2), and in principle it is not possible to distinguish them by MFM. As will be shown, an educated guess on the magnetization can be done as long the changes in magnetization are small compared to a well defined reference state, for example the charge ordered state (see Section 4.2). When the field is applied close to the hard axis, i.e. in nn-direction, no charge ordered state arises. In this direction, every third bridge has its long axis perpendicular to the field vector, and the magnetization then randomly relaxes either to the left or to the right so that the resulting charge pattern shows no order, but neither could any ice-rule violation be found. The magnetization reversal with the field in nn-direction was thus not investigated by MFM.

Figure 4.25 presents a series of MFM images, recorded at the indicated magnetic fields which was applied close to the easy axis (nnn-direction). Although there is an angle of 6° between field and nnn-direction, the charge ordered state arises in remanence (Figure 4.25 a)). This small misalignment of the field should not significantly affect the magnetization reversal, as a comparison of the simulated hysteresis loops for the Iron antidot lattice with a field aligned in nnn-direction and with a 7° tilt with respect to that direction as presented in Figure 4.21 suggests.
At the upper edge of image 4.25 a), the antidot lattice contains defects so that the magnetization deviates from the periodic pattern in this region. Up to a counter-field of $H = 230\,\mathrm{Oe}$ the magnetization is stable. For slightly larger fields, the observed pattern indicates that single bridges reversed. Their flipped magnetization is marked by the red arrows in Figure 4.25 b), which was recorded at a counter field of $H = 260\,\mathrm{Oe}$. At the vertices of such a reversed bridge the charge order breaks down, so that now charges of the same sign are neighboring. The long axes of the switched bridges all enclose an angle of 66° (60° resulting from the honeycomb lattice formed by the magnetic bridges, and 6° from the misalignment of the field with respect to the nnn-direction) with the field, while none of the 6° or 54° bridges are switched. This is reasonable, as the moments $\vec{\mu}$ enclosing the largest angle with the field $\vec{B} = \mu_0\vec{H}$ experience the strongest torque $\vec{\mu} \times \vec{B}$. Furthermore, as discussed at the end of Section 1.3.3, not all macrospins are equivalent in the charge ordered state. Their orientation with respect to the saturating field separates them into two categories. When a bridge which is (almost) parallel to the original saturating field switches, it comes to an ice-rule violation. Only switching of the bridges enclosing larger angles with the field is compatible with the ice-rules (see Figure 1.10).

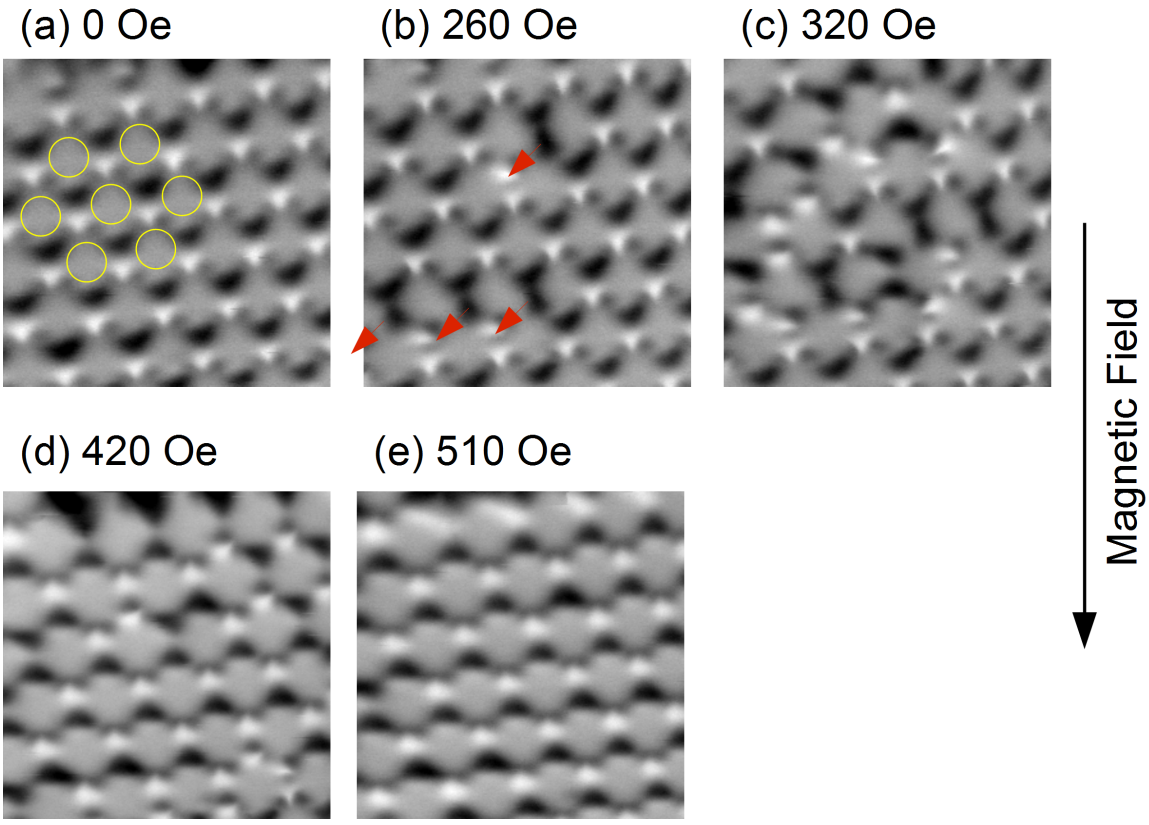

Figure 4.25: In-field MFM images, showing a $3 \times 3\,\mu\mathrm{m}^2$ large section of a $t = 20\,\mathrm{nm}$ thick Permalloy antidot array with a lattice parameter of $a = 500\,\mathrm{nm}$ and hole diameter of $d = 400\,\mathrm{nm}$ during the magnetization reversal. The yellow circles in (a) represent the antidot positions. The arrow on the right margin indicates the direction of the counter field. The field encloses an angle of $6°$ with respect to the next nearest neighbor direction of the antidot lattice. The small red arrows in (b) indicated reversed magnetic bars. For higher fields, it is not possible to deduce the magnetization of the bars from the charge pattern.

It is worth noting that this experimental finding does not completely match the behavior which was found in micromagnetic simulations as discussed above, where larger regions of the sample switch collectively. However, these simulations modeled the smaller geometry with $a = 200\,\mathrm{nm}$ and $d = 175\,\mathrm{nm}$, so that this difference can be probably attributed to the reduction of dimensions. Unfortunately, reasonable modeling of a system based on a lattice parameter of $a = 500\,\mathrm{nm}$ was not possible with the available hardware. Simulations for the $a = 200\,\mathrm{nm}$ based geometry with the material parameters of Permalloy yielded qualitatively the same results as for Iron.

Upon further increase of the counter field to $H = 320\,\mathrm{Oe}$ (Figure 4.25 c)), no obvious order in the charge pattern can be identified anymore. Many of the bridges have switched now, and there is a multitude of possible magnetization configurations which would result in the same pattern. Occurrence of this very disordered state stands in contradiction to the simulations for the smaller scaled Iron antidot array. If larger regions would switch

collectively, this would be reflected in a local charge order, which is however inverted with respect to the original charge ordered state as shown in 4.25 a).

At a field of $H = 420\,\mathrm{Oe}$ (Figure 4.25 d)), such a local inverted charge order can be observed. Large portions of the investigated sample section have completed their reversal, and only a few vertices are not reversed at this stage. These defects in the charge order are relatively stable and do not vanish up to a field of $H = 510\,\mathrm{Oe}$ (Figure 4.25 e)). In the course of many such reversal experiments, not a single ice-rule violation, which should yield three times the frequency shift of an ice-rule conform vertex, was found.

A method to directly image the magnetization instead of the resulting stray field is X-PEEM (see Section 3.4.2 for a description of the technique and setup). The same sample as discussed above in the context of the MFM measurements was investigated. Due to the scarce amount of beam time, only a single geometry could undergo a detailed investigation: As shown in Figure 4.26 g), field and the nn-direction (hard axis) of the antidot lattice enclose an angle of $7°$. The blue and red contrast in the XMCD images is explained in Figure 4.26 i): The projection of the wave vector of the X-rays on the sample plane enclosed an angle of $20°$ with respect to the vertical of the images, and the XMCD contrast is proportional to the projection of the magnetization on this axis. All images in Figure 4.26 were recorded in remanence, after the indicated fields were applied. This was necessary as with an applied field the emitted photo electrons experience a strong deflection so that the resolution suffers significantly. However, once a bridge has switched, it keeps the switched magnetization in remanence as additional MFM experiments and simulations have revealed. The chosen approach is thus suitable to investigate the magnetization reversal. The fields are given in terms of H_C, as the absolute field was unknown. H_C, in turn, is determined by the image in which 50% of the sample section has switched, which is the case for image f).

The remanent state after saturating the sample opposite to the indicated field direction is shown in Figure 4.26 a). The entire sample section appears blue, but bridges which enclose a larger angle with the beam incidence plane exhibit a weaker XMCD signal. The strictly blue contrast indicates the charge ordered state. Aforementioned $7°$ offset between magnetic field and hard axis is enough to induce a preferential magnetization direction in all bridges. This was also found in micromagnetic simulations of the same scenario, which, however, used the reduced lattice constant of $a = 200\,\mathrm{nm}$ and Fe material parameters. The corresponding snapshots from the simulations can be found in Figure 4.27 a).
Applying a counter field of $0.78H_C$ (Figure 4.26 b)) initiates the magnetization reversal, indicated by local red contrast. All bridges which have switched at this stage appear to

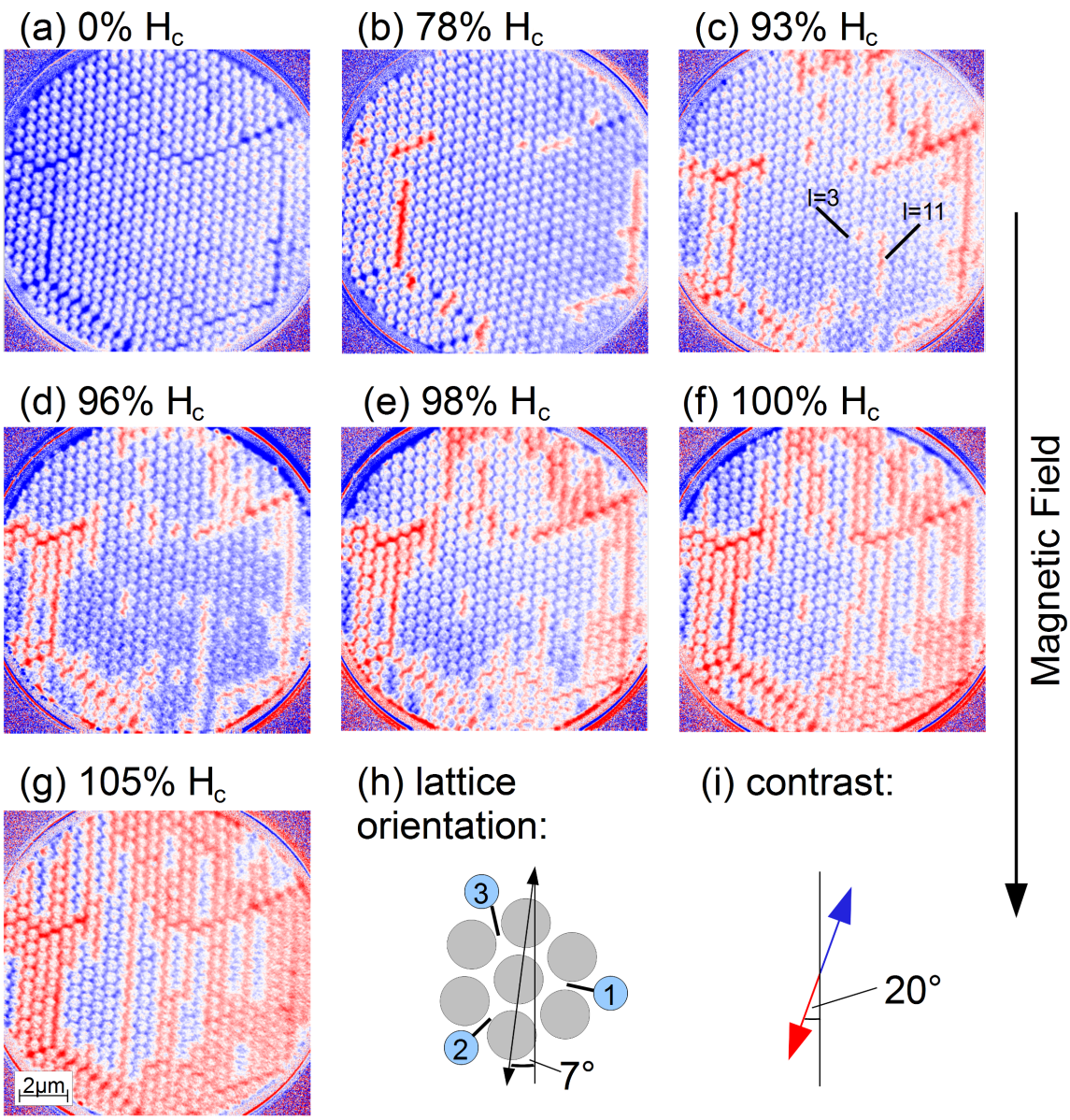

Figure 4.26: (a) - (g) XMCD images recorded by X-PEEM at the Fe L_3-edge ($h\nu \approx 708\,\mathrm{eV}$) of a Permalloy antidot array with $a = 500\,\mathrm{nm}$, $d = 400\,\mathrm{nm}$ and $t = 20\,\mathrm{nm}$. All images where recorded in remanence after the indicated fields were applied. In (h), the orientation between antidot lattice and external field is shown: The field encloses an angle of $7°$ with the nn-direction. With respect to the field direction, there are three nonequivalent sets of bridges, resulting in angles between field and the long axis of the respective bridge of $83°$ (1), $37°$ (2) and $23°$ (3). (i) The XMCD contrast is proportional to the projection of the magnetization on an axis which is tilted by $20°$ with respect to the vertical of the images.

have a larger than average width caused by defects in the antidot lattice. The increased width reduces their aspect ratio and thus, their shape anisotropy.

A field of $0.93H_C$ results in the first switching processes which cannot be related to obvious defects, for example in the center region of Figure 4.26 c). Several red chains arise, which

follow the bridges enclosing the smallest angles with respect to the magnetic field ($23°$ and $37°$ for the present geometry, see Figure 4.26 h)). The length of these chains is between 3 and 11 bridges at this stage, both are marked in the Figure. Increasing the field from this point on leads to nucleation of more such chains and to growth of the ones which were already present (Figure 4.26 d)). The chain which extended over 11 bridges in the previous state connected to another chain at the lower region of the image. Unfortunately, the XMCD contrast of the bridges which enclose the largest angle with the magnetic field ($83°$) is very weak and thus very noisy, so that statements on their switching behavior cannot be made on the basis of the measurement data. This also prevents insight into the possible occurrence of ice-rule violations.

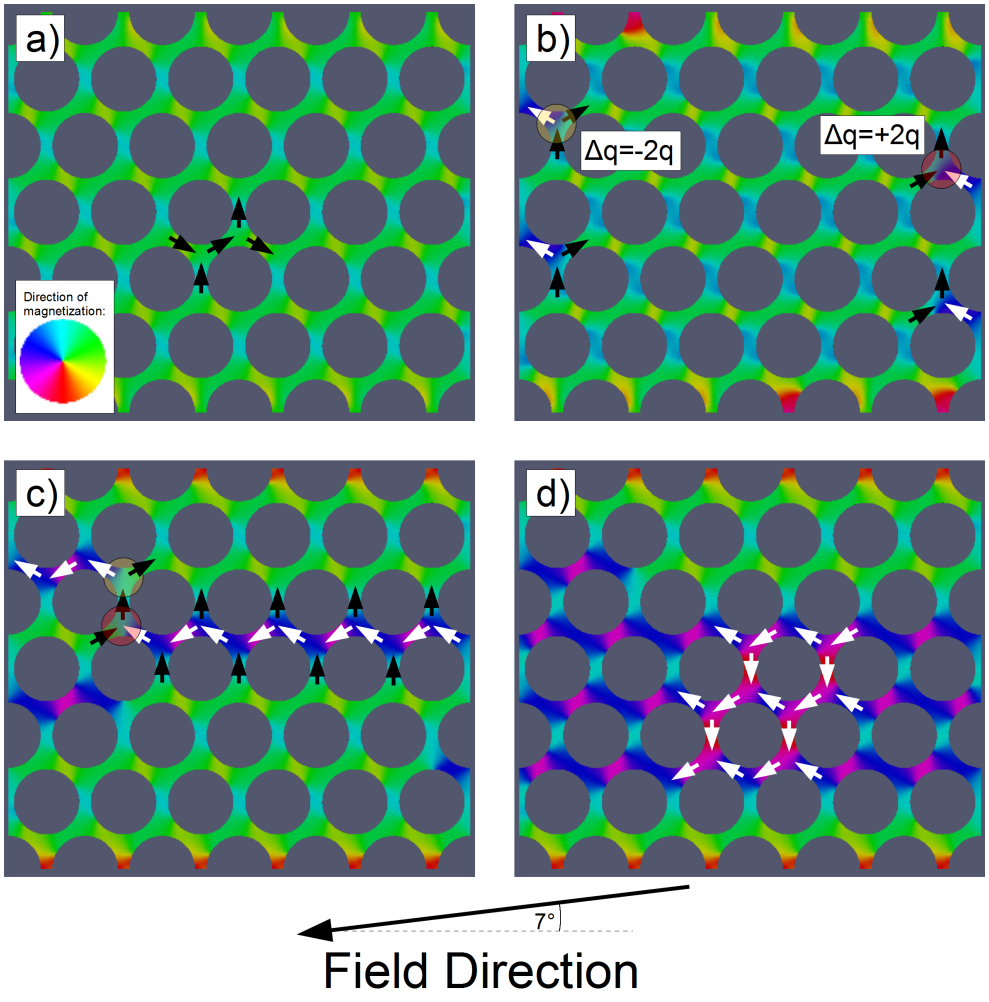

Figure 4.27: Snapshots from micromagnetic simulations of the magnetization reversal for an Fe antidot array with $a = 200\,\mathrm{nm}$ and $d = 175\,\mathrm{nm}$, with the field applied in an angle of $7°$ with respect to the nn-direction (hard axis) (a) is the remanent state, (b), (c) and (d) correspond to counter fields of $565\,\mathrm{Oe}$, $791\,\mathrm{Oe}$ and $829\,\mathrm{Oe}$. Black arrows stand for the original magnetization of a bridge, while white arrows indicate reversed magnetization. The ice-rules apply at every vertex. Charge defects $\Delta q = \pm 2q$ travel in opposite directions during the reversal.

A closer look at the simulations modeling this experimental field arrangement can give an idea about these aspects. There, starting from the charge ordered state (Figure 4.27 a)), single bridges on the boundary of the geometry switch at a field of $565\,\mathrm{Oe}$ (Figure 4.27 b)). Switching at the boundaries can be understood as strong demagnetizing fields emerge there. All of the bridges which reversed their magnetization at this stage are from the type which is tilted by $37°$ with respect to the field. In analogy to the discussion of the results from the X-PEEM investigation, these can be described as chains of length 1. The switching changes the charge of the adjacent vertices by $\Delta q = \pm 2q$, as indicated in the Figure, giving rise to so-called charge defects with respects to the charge ordered state [12]. Upon increasing the counter-field to $829\,\mathrm{Oe}$, these chains grow (Figure 4.27 c)). The growth direction is clearly determined by the external field, similar as in the X-PEEM experiment. Neither nucleation nor growth of these chains results in an ice-rule violation. As reported for lithographically defined artificial spin-ice systems [12, 14, 159], the growth of these chains is accompanied by a separation of the magnetic charge defects: the $\Delta q = +2q$ defect (marked by a red circle) travels in the direction of the external field, while the $\Delta q = -2q$ defect (marked by a yellow circle) travels in the opposite direction and therefore mimic the behavior of the monopole anti-monopole pair in bulk spin-ice (see Ref. [47] and Section 1.3). The chains hereby take the role of the “Dirac Strings”. Within these chains, the vertex charges are not changed with respect to the charge ordered state.
The magnetization reversal continues by growth and nucleation of new chains for fields below $829\,\mathrm{Oe}$ At this stage, the bridges enclosing an angle of $83°$ with respect to the field begin to switch (Figure 4.27 d)). Their switching is always in agreement with the ice-rules and eventually yields a completely inverted charge ordered state (not shown).

The magnetization reversal discussed here, with the field applied in a direction tilted by $7°$ degrees with respect to the hard axis (nn-direction) is very similar to the simulated results for the actual hard axis reversal. The main difference is that the tilt of the field yields a preferential magnetization direction in all bridges, resulting in a charge order in remanence. The formation and growth of chains along the field direction can be observed in both cases.

4.5.3 Summary

For an Fe antidot array with a d/a-ratio of 0.85 ($a = 200\,\mathrm{nm}$, $d = 175\,\mathrm{nm}$), micromagnetic simulations identify the nnn-direction, where the field is applied along the long axis of one third of the emerging bridges, as the easy axis, while the nn-direction is the hard-axis. Experimentally, this could not be confirmed unambiguously. Although the longitudinal AMR signatures, measured on FIB-selected single antidot crystallites with a net current direction

either in nn- or nnn-direction, strongly differ in magnitude and overall shape, the coercive field for both directions turned out to be equal. The reason for this inconsistency could not be determined. In transverse geometry, a directional dependence of the coercive field can be resolved which is in accordance to the simulated results.

The AMR curves contain more information on the reversal processes. The transverse AMR signal's magnitude for a net current parallel to the nnn-direction exceeds the one for a net current along the nn-direction by a factor larger than 2. In the former case, fields in the range from $880\,\mathrm{Oe}$ to approximately $3000\,\mathrm{Oe}$ induce a change from the spin-ice-like magnetization pattern, with the magnetic bridges being magnetized along their long axes, into the magnetization pattern which was discussed in Section 4.2 for antidot arrays with a small d/a ratio. This large change in magnetization angle is responsible for the comparatively large signal.

According to Tanaka et al. [119], the occurrence of a single peak or dip in the AMR signal during the magnetization reversal is an indicator that the ice-rules for the vertices apply all the time. Micromagnetic simulations support this interpretation.

The experimental conditions of X-PEEM and MFM required a magnetically softer sample, so that the microscopic study is based on a Permalloy antidot array with $a = 500\,\mathrm{nm}$ and $d = 400\,\mathrm{nm}$ (d/a-ratio $= 0.8$). The hard axis reversal (nn-direction) is complicated to investigate by MFM, as no ordered reference state is accomplished and the reconstruction of the magnetization from the magnetic charge pattern is not unambiguous. The easy axis reversal sets in by switching of single bridges. These are selected so that the ice-rules apply. For larger fields the charge order is completely lost and a reconstruction of the sample magnetization is not possible anymore. However, it can be concluded that the reversal is not driven by the switching of whole sample regions, as simulations suggest it for the $a = 200\,\mathrm{nm}$ based geometry.

In a X-PEEM investigation of the reversal with a field applied close to the hard axis (tilt-angle = $7°$), a reversal mechanism which is initially driven by nucleation and subsequent separation of charge defects $\Delta q = \pm 2q$ with respect to the charge ordered state was found. These form the analog to the "monopole anti-monopole" pair which can emerge in bulk spin-ice. This behavior is also found in the simulations for the smaller antidot geometry. Furthermore, both MFM and X-PEEM revealed that the magnetization reversal is very sensitive to defects in the antidot lattice. These are difficult to model and their effect could not be determined. With recent improvements in colloidal lithography (see Ref. [69]), this problem could be overcome for future experiments so that more idealized structures can be investigated.

5 Summary

In the present thesis, the magnetic properties of hexagonally ordered antidot arrays within magnetically soft thin films of Iron, Cobalt or Permalloy have been studied. The preparation of these samples has been realized by colloidal lithography. Based on the self-assembly of polystyrene spheres with an average diameter of $200\,\mathrm{nm}$, this optimized process is capable to cover substrates on the centimeter scale with a continuous, polycrystalline monolayer. The size of these crystallites, in which the orientation of the hexagonal lattice is preserved, is of the order of $25 \times 25\,\mu\mathrm{m}^2$. After size reduction of the spheres which is achieved by Oxygen plasma etching, the resulting structure is used as a template for pulsed laser deposition of the magnetic thin films.

Based on a sample series with a constant lattice parameter of $a = 200\,\mathrm{nm}$, SQUID magnetometry revealed a monotonous increase of the coercive field with increasing antidot diameter d for all the tested materials. For antidot diameters in the range from $45\,\mathrm{nm}$ to $140\,\mathrm{nm}$, the coercive field is a linear function of the diameter. For even larger hole diameters, the coercive field grows by a disproportionally large margin. This is accompanied by a change in the hysteresis loops' shape from square-like for diameters of $140\,\mathrm{nm}$ and below, to a more convex shape with a broader switching field distribution. These findings indicate a transition in the principal magnetization behavior in this diameter regime.
A reduction of the lattice parameter from $200\,\mathrm{nm}$ to $100\,\mathrm{nm}$ leads to a further increase of the observed coercive fields for a given diameter-to-lattice parameter (d/a) ratio. For this smaller periodicity, the disproportionally large increase in coercivity sets in at diameters between $70\,\mathrm{nm}$ and $85\,\mathrm{nm}$. In combination with the results for antidot arrays with a lattice parameter of $a = 200\,\mathrm{nm}$, one can identify the d/a ratio as the main driver for the transition in the magnetization behavior. The critical d/a-ratio can be determined to be in the range $0.7 < (d/a)_{crit} < 0.8$.

MFM investigation of antidot arrays with a d/a-ratio above and below aforementioned threshold revealed two distinct domain patterns in the remanent state. The pattern arising in antidot arrays with large d/a-ratio results from a minimization of the stray field energy: In that case, the magnetic material between two neighboring holes forms narrow, elongated bridges. Shape anisotropy forces their magnetization to align along their respective long axis. As a consequence of the lattice symmetry, vertices arise at which three such bridges

are connected. The odd number of vertex-sharing bridges always results in a residual magnetic charge at these positions. The resulting pattern resembles the charge ordered state in geometrically frustrated artificial kagomé spin-ice, minimizing the intra- and inter-vertex interaction alike.
In MFM, the pattern for small d/a-ratios appears as a hexagonal arrangement of rhombi. Each can be attributed to a primitive unit cell of the antidot lattice. Correlation of experiment and simulation reveals five domains per unit cell. The central domain is oriented in a way which decreases the angle enclosed by neighboring domains to 30° as opposed to 60° for the domain pattern for large d/a-ratios. Consequently, domain wall energy is drastically reduced in this configuration.

In both cases the magnetization shows a strong correlation with the antidot lattice, which suggests occurrence of an in-plane anisotropy of the magnetization reversal. As a consequence of the lack of long-range order of the self-assembly approach, application of integral magnetometry methods is not suitable to resolve this anisotropy. A novel method to overcome this problem is suggested in this thesis: The electrical current of a magnetotransport experiment is channeled through single crystallites of the antidot lattice. This is achieved by FIB-milling. The AMR then serves as a local probe for the magnetization reversal. The AMR-effect is strongly influenced by the presence of the holes, as these shadow the electrical current in some sample areas. However, characteristic peaks / dips in the resistance during the magnetization reversal turned out to be good measures for the coercive field. A microscopic understanding of the AMR curves was achieved by correlation with results from MFM and micromagnetic simulations.

For samples with a small d/a-ratio, local probing of the magnetization identifies the nearest neighbor (nn-)direction of the lattice as the easy axis, while the next nearest neighbor (nnn)-direction is the hard axis, which is in agreement with the results from micromagnetic simulations. An additional study of the respective reversal mechanisms by in-field MFM shows that in the nn-direction, the magnetization undergoes small reversible changes for fields almost up to the coercive field. Then, irreversible nucleation and growth of 180° reversed mesoscopic domains sets in. The domain walls are clearly pinned by the antidot lattice. For the nnn-direction, the switching mode is characterized by non-collective rotation of the magnetization over intermediate easy axis.

The field, at which the transition from reversible to irreversible magnetization reversal sets in, depends strongly on the magnetic material. The main driver hereby is the saturation magnetization, which directly influences the shape anisotropy energy, and thus stabilizes the magnetization in the reversible regime of the reversal. On the other hand, the obstacle

which the antidots pose to the domain wall movement seems to increase the larger the exchange constant, and therefore the domain wall energy of the respective material is.

For antidot arrays with large d/a-ratio, the long axes of the bridges determine the easy axes. These are identical to the nnn-direction of the antidot lattice. The nn-directions are then the hard-axes. The occurrence of a single peak / dip in the magnetotransport signal during the whole magnetization reversal suggests that the magnetic charge configuration at the vertices complies with the ice-rules $q_{vertex} = \pm q$ as a consequence of a strong coupling between the bridges. This finding is confirmed by micromagnetic simulations. Furthermore, the magnetic bridges maintain an Ising-spin-like behavior, which is an important requisite for the application as a model system for spin-ice.
Both in experiments and in simulations, a reversal mechanism which is characterized by the nucleation and subsequent separation of charge defects $\Delta q = \pm 2q$) is found when the field is applied close to one of the hard axis, further underlining the analogy to the conventional artificial spin-ice systems. A thorough characterization of the easy axis reversal stands out, as the stray field detected by MFM does not allow unambiguous reconstruction of the magnetization. Further X-PEEM experiments would provide this information.

Bibliography

[1] A. Kaidatzis and J. M. Garcia-Martin, Nanotechnology **24**, 165704 (2013).

[2] J. Raabe, R. Pulwey, R. Sattler, T. Schweinböck, J. Zweck, and D. Weiss, Journal of Applied Physics **88**, 4437 (2000).

[3] W. F. Brown, Journal of Applied Physics **39**, 993 (1968).

[4] A. Ethirajan, U. Wiedwald, H.-G. Boyen, B. Kern, L. Han, A. Klimmer, F. Weigl, G. Kästle, P. Ziemann, K. Fauth, J. Cai, R. J. Behm, A. Romanyuk, P. Oelhafen, P. Walther, J. Biskupek, and U. Kaiser, Advanced Materials **19**, 406 (2007).

[5] A. Manzin and O. Bottauscio, Journal of Physics D: Applied Physics **45**, 095001 (2012).

[6] C. C. Wang, A. O. Adeyeye, and Y. H. Wu, Journal of Applied Physics **94**, 6644 (2003).

[7] Y. Tang and J.-G. Zhu, IEEE Transactions on Magnetics **43**, 2139 (2007).

[8] L. Torres, L. Lopez-Diaz, and J. Iniguez, Applied Physics Letters **73**, 3766 (1998).

[9] B. Lenk, H. Ulrichs, F. Garbs, and M. Münzenberg, Physics Reports **507**, 107 (2011).

[10] S. Neusser and D. Grundler, Advanced Materials **21**, 2927 (2009).

[11] P. Dirac, Proceedings of the Royal Society of London. Series A **133**, 60 (1931).

[12] E. Mengotti, L. J. Heyderman, A. F. Rodríguez, F. Nolting, R. V. Hügli, and H.-B. Braun, Nature Physics **7**, 68 (2010).

[13] C. C. Wang, A. O. Adeyeye, and N. Singh, Nanotechnology **17**, 1629 (2006).

[14] S. Ladak, D. Read, T. Tyliszczak, W. R. Branford, and L. F. Cohen, New Journal of Physics **13**, 023023 (2011).

[15] A. Plettl, F. Enderle, M. Saitner, A. Manzke, C. Pfahler, S. Wiedemann, and P. Ziemann, Advanced Functional Materials **19**, 3279 (2009).

[16] J. Stöhr and H. C. Siegmann, *Magnetism - From Fundamentals to Nanoscale Dynamics* (Springer Berlin Heidelberg, 2006).

[17] S. Chikazumi, *Physics of Ferromagnetism* (Oxford Press, 1997).

[18] W. Heisenberg, Zeitschrift für Physik **38**, 456 (1926).

[19] P. Dirac, Proceedings of the Royal Society of London. Series A **112**, 661 (1926).

[20] H. Kronmüller and M. Fähnle, *Micromagnetism and the Microstructure of Ferromagnetic Solids* (Cambridge University Press, 2003).

[21] J. Stöhr and H. König, Physical review letters **75**, 3748 (1995).

[22] A. Hubert, W. Rave, and S. Tomlinson, Physica Status Solidi (B) **204**, 817 (1997).

[23] A. Hubert and R. Schäfer, *Magnetic Domains: The Analysis of Magnetic Microstructures* (Springer Berlin Heidelberg, 1998).

[24] R. Hertel and H. Kronmüller, Journal of Applied Physics **85**, 6190 (1999).

[25] G. S. Abo, Y.-K. Hong, J. Park, J. Lee, W. Lee, and B.-C. Choi, IEEE Transactions on Magnetics **49**, 4937 (2013).

[26] R. Wade, Proceedings of the Physical Society **79**, 1237 (1962).

[27] M. Barthelmess, C. Pels, A. Thieme, and G. Meier, Journal of Applied Physics **95**, 5641 (2004).

[28] R. Gross and A. Marx, "Grundlagen der Magnetoelektronik," (2000).

[29] W. Thomson, Proceedings of the Royal Society of London **8**, 546 (1857).

[30] T. R. McGuire and R. I. Potter, IEEE Transactions on Magnetics **Mag-11**, 1018 (1975).

[31] H. Nagasawa, Physics Letters A **41**, 39 (1972).

[32] J. Smit, Physica **16**, 612 (1951).

[33] H. Van Elst, Physica **25**, 708 (1959).

[34] P. Grünberg, R. Schreiber, and Y. Pang, Physical Review Letters **57**, 2442 (1986).

[35] M. Baibich, J. Broto, A. Fert, and F. V. Dau, Physical Review Letters **61**, 2472 (1988).

[36] P. Wisniewski, Applied Physics Letters **90**, 192106 (2007).

[37] N. W. Ashcroft and N. D. Mermin, *Solid State Physics* (Holt, Rinehart and Winston, 1976) p. 708.

[38] E. N. Mitchell, H. B. Haukaas, H. D. Bale, and J. B. Streeper, Journal of Applied Physics **35**, 2604 (1964).

[39] N. Mott, Advances in Physics **13**, 325 (1964).

[40] G. Toulouse, Communications on Physics **2**, 115 (1977).

[41] G. Wannier, Physical Review **79**, 357 (1950).

[42] E. Ising, Zeitschrift für Physik A Hadrons and Nuclei **31**, 253 (1925).

[43] A. Ramirez, A. Hayashi, and R. Cava, Nature **399**, 333 (1999).

[44] L. Pauling, Journal of the American Chemical Society **57**, 2680 (1935).

[45] S. T. Bramwell and M. J. Gingras, Science **294**, 1495 (2001).

[46] M. Harris, S. Bramwell, D. McMorrow, T. Zeiske, and K. W. Godfrey, Physical Review Letters **79**, 2554 (1997).

[47] C. Castelnovo, R. Moessner, and S. L. Sondhi, Nature **451**, 42 (2008).

[48] S. Ladak, D. E. Read, G. K. Perkins, L. F. Cohen, and W. R. Branford, Nature Physics **6**, 359 (2010).

[49] A. Schumann, B. Sothmann, P. Szary, and H. Zabel, Applied Physics Letters **97**, 022509 (2010).

[50] A. Remhof, A. Schumann, A. Westphalen, H. Zabel, N. Mikuszeit, E. Vedmedenko, T. Last, and U. Kunze, Physical Review B **77**, 134409 (2008).

[51] R. F. Wang, C. Nisoli, R. S. Freitas, J. Li, W. McConville, B. J. Cooley, M. S. Lund, N. Samarth, C. Leighton, V. H. Crespi, and P. Schiffer, Nature **439**, 303 (2006).

[52] S. Ladak, S. K. Walton, K. Zeissler, T. Tyliszczak, D. E. Read, W. R. Branford, and L. F. Cohen, New Journal of Physics **14**, 045010 (2012).

[53] S. Tacchi, M. Madami, G. Gubbiotti, G. Carlotti, A. O. Adeyeye, S. Neusser, B. Botters, and D. Grundler, IEEE Transactions on Magnetics **46**, 172 (2010).

[54] D. Tripathy and A. O. Adeyeye, New Journal of Physics **13**, 023035 (2011).

[55] M. Tornow, D. Weiss, K. v Klitzing, K. Eberl, D. Bergman, and Y. Strelniker, Physical review letters **77**, 147 (1996).

[56] D. Weiss, K. Richter, E. Vasiliadou, and G. Lütjering, Surface Science **305**, 408 (1994).

[57] R. Cowburn, A. Adeyeye, and J. Bland, Journal of Magnetism and Magnetic Materials **8853** (1997).

[58] A. Y. Toporov, R. M. Langford, and A. K. Petford-Long, Applied Physics Letters **77**, 3063 (2000).

[59] S. Neusser, G. Duerr, S. Tacchi, M. Madami, M. L. Sokolovskyy, G. Gubbiotti, M. Krawczyk, and D. Grundler, Physical Review B **84**, 094454 (2011).

[60] A. A. Zhukov, A. V. Goncharov, P. A. J. de Groot, P. N. Bartlett, and M. A. Ghanem, Journal of Applied Physics **93**, 7322 (2003).

[61] S. Wiedemann, *Präparation optimierter Kolloidmasken*, Diploma thesis, Ulm University (2008).

[62] P. Muralidhar, *Improvement of modified Fischer Pattern Lithography*, Master thesis, Ulm University (2010).

[63] "http://www.lifetechnologies.com/de/de/home/brands/invitrogen.html," (2013).

[64] D. Qiu, T. Cosgrove, and A. M. Howe, Macromolecular Chemistry and Physics **206**, 2233 (2005).

[65] "http://www.silson.com," (2013).

[66] T. Suni, K. Henttinen, I. Suni, and J. Mäkinen, Journal of The Electrochemical Society **149**, G348 (2002).

[67] N. Denkov, O. Velev, P. Kralchevski, I. B. Ivanov, H. Yoshimura, and K. Nagayama, Langmuir **8**, 3183 (1992).

[68] N. Denkov, O. Velev, and P. Kralchevsky, Nature **361**, 26 (1993).

[69] M. Hartmann, *Einfluss der Flüssig-Flüssig-Grenzfläche auf die Fernordnung dort deponierter Kolloid-Monolagen*, Bachelor thesis, Ulm University (2013).

[70] C.-C. Ho, P.-Y. Chen, K.-H. Lin, W.-T. Juan, and W.-L. Lee, ACS applied materials & interfaces **3**, 204 (2011).

[71] U. C. Fischer and H. P. Zingsheim, Journal of Vacuum Science and Technology **19**, 881 (1981).

[72] F. Burmeister, C. Schäfle, B. Keilhofer, C. Bechinger, J. Boneberg, and P. Leiderer, Advanced Materials **10**, 495 (1998).

[73] C. Haginoya, M. Ishibashi, and K. Koike, Applied Physics Letters **71**, 2934 (1997).

[74] C. Pfahler, *Additive und subtraktive Strukturierung mit Hilfe von selbstorganisierten Nanoteilchen Masken*, Diploma thesis, Ulm University (2006).

[75] M. Weinelt, H. Baier, S. Schwarz, and T. Fauster, Surface Science **454-456**, 746 (2000).

[76] G. Lengl, *Aufbau einer Laser-Ablations-Apparatur für Metallschichten*, Diploma thesis, Ulm University (1998).

[77] M. Trautvetter, U. Wiedwald, H. Paul, A. Minkow, and P. Ziemann, Applied Physics A **102**, 725 (2010).

[78] C. Brombacher, M. Saitner, C. Pfahler, A. Plettl, P. Ziemann, D. Makarov, D. Assmann, M. H. Siekman, L. Abelmann, and M. Albrecht, Nanotechnology **20**, 105304 (2009).

[79] S. Nau, *Herstellung und Charakterisierung perkolierter magnetischer Medien*, Diploma thesis, Ulm University (2009).

[80] Q. Yan, L. Gao, V. Sharma, Y.-M. Chiang, and C. C. Wong, Langmuir : the ACS journal of surfaces and colloids **24**, 11518 (2008).

[81] "http://rsb.info.nih.gov/ij/," (2013).

[82] I. Horcas, R. Fernández, J. M. Gómez-Rodríguez, J. Colchero, J. Gómez-Herrero, and A. M. Baro, The Review of scientific instruments **78**, 013705 (2007).

[83] QuantumDesign, "MPMS Options Manual," (1999).

[84] QuantumDesign, MPMS Applicatoin Note 1014-208 , 1 (2001).

[85] M. Sawicki, W. Stefanowicz, and A. Ney, Semiconductor Science and Technology **26**, 064006 (2011).

[86] M. Ziese, G. Heydon, R. Höhne, P. Esquinazi, and J. Dienelt, Applied Physics Letters **74**, 1481 (1999).

[87] J. Moodera, L. Kinder, T. Wong, and R. Meservey, Physical Review Letters **74**, 3273 (1995).

[88] C. Leighton, M. Song, J. Nogues, M. C. Cyrille, and I. K. Schuller, Journal of Applied Physics **88**, 344 (2000).

[89] G. Binnig, C. Quate, and C. Gerber, Physical Review Letters **56**, 930 (1986).

[90] Y. Martin and H. Wickramasinghe, Applied Physics Letters **50**, 1455 (1987).

[91] W. L. Murphy and G. Spalding, American Journal of Physics **67**, 905 (1999).

[92] U. Hartmann, Annual Review of Materials Science **29**, 53 (1999).

[93] T. R. Albrecht, P. Grütter, D. Horne, and D. Rugar, Journal of Applied Physics **69**, 668 (1991).

[94] U. Hartmann, Physics Letters A **137**, 475 (1989).

[95] L. Kong and S. Chou, Applied physics letters **70**, 2043 (1997).

[96] J. Lohau, S. Kirsch, A. Carl, G. Dumpich, and E. F. Wassermann, Journal of Applied Physics **86**, 3410 (1999).

[97] T. Häberle, F. Haering, H. Pfeifer, L. Han, B. Kuerbanjiang, U. Wiedwald, U. Herr, and B. Koslowski, New Journal of Physics **14**, 043044 (2012).

[98] R. Kümmel, *Modifikation eines Rasterkraftmikroskops für den Einsatz im Bereich Nanolithographie*, Diploma thesis, Ulm University (2008).

[99] F. Haering, *Optimierung eines Rasterkraftmikroskops zur Untersuchung magnetischer Nanoteilchen*, Diploma thesis, Ulm University (2009).

[100] H. Straub, *Charakterisierung der Eigenschaften magnetischer Nanoteilchen mittels magnetischer Kraftmikroskopie*, Diploma thesis, Ulm University (2011).

[101] S. Nothelfer, *Charakterisierung von magnetischen Loch-Raster-Strukturen mit der Magnetkraftmikroskopie*, Master thesis, Ulm University (2013).

[102] T. Eimüller, *Magnetic imaging of nanostructured systems with Transmission X-ray Microscopy*, Ph.D. thesis, Würzburg University (2002).

[103] J. Stöhr, H. Padmore, S. Anders, T. Stammler, and M. R. Scheinfein, Surface Review and Letters **5**, 1297 (1998).

[104] D. Nolle, M. Weigand, G. Schütz, and E. Goering, Microscopy and Microanalysis **17**, 834 (2011).

[105] D. Nolle, M. Weigand, P. Audehm, E. Goering, U. Wiesemann, C. Wolter, E. Nolle, and G. Schütz, The Review of scientific instruments **83**, 046112 (2012).

[106] J. Miguel, M. Bernien, D. Bayer, J. Sánchez-Barriga, F. Kronast, M. Aeschlimann, H. a. Dürr, and W. Kuch, The Review of scientific instruments **79**, 033702 (2008).

[107] S. Imada, S. Suga, W. Kuch, and J. Kirschner, Surface Review and Letters **09**, 877 (2002).

[108] L. D. Landau and E. Lifshitz, Phys. Z. Sowjetunion **8**, 101 (1935).

[109] T. L. Gilbert, IEEE Transactions on Magnetics **40**, 3443 (2004).

[110] J. Wu, J. Moore, and R. Hicken, Journal of magnetism and magnetic materials **222**, 189 (2000).

[111] H. Fangohr, T. Fischbacher, M. Franchin, G. Bordignon, J. Generowicz, A. Knittel, M. Walter, and M. Albert, "Nmag User Manual," (2012).

[112] M. Donahue and D. Porter, "OOMMF's user guide, Version 1.0," Tech. Rep. (National Institute of Standards and Technology, Gaithersburg, MD, 1999).

[113] T. Fischbacher, M. Franchin, G. Bordignon, and H. Fangohr, IEEE Transactions on Magnetics **43**, 2896 (2007).

[114] W. Scholz, J. Fidler, T. Schrefl, D. Suess, R. Dittrich, H. Forster, and V. Tsiantos, Computational Materials Science **28**, 366 (2003).

[115] K. J. Kirk, J. N. Chapman, and C. D. W. Wilkinson, Applied Physics Letters **71**, 539 (1997).

[116] J. Schöberl, Computing and visualization in science **1**, 41 (1997).

[117] A. Adeyeye, J. Bland, and C. Daboo, Applied physics letters **70**, 3164 (1997).

[118] W. Lee, H. Leung, W. Zhang, Y. Xu, a. Hirohata, C. Yao, B.-C. Choi, D. Hasko, and J. Bland, IEEE Transactions on Magnetics **35**, 3475 (1999).

[119] M. Tanaka, E. Saitoh, H. Miyajima, T. Yamaoka, and Y. Iye, Physical Review B **73**, 052411 (2006).

[120] J. D. Livingston, Journal of Applied Physics **52**, 2544 (1981).

[121] E. Paz, F. Cebollada, F. J. Palomares, J. M. Gonzalez, M.-Y. Im, and P. Fischer, Journal of Applied Physics **111**, 073908 (2012).

[122] I. Ruiz-Feal, L. Lopez-Diaz, A. Hirohata, J. Rothman, C. M. Guertler, M. Natali, D. Decanini, and Y. Chen, Journal of Magnetism and Magnetic Materials **245**, 597 (2002).

[123] J. F. Smyth, S. Schultz, D. R. Fredkin, D. P. Kern, S. a. Rishton, H. Schmid, M. Cali, and T. R. Koehler, Journal of Applied Physics **69**, 5262 (1991).

[124] L. Heyderman, F. Nolting, D. Backes, S. Czekaj, L. Lopez-Diaz, M. Kläui, U. Rüdiger, C. Vaz, J. Bland, R. Matelon, U. Volkmann, and P. Fischer, Physical Review B **73**, 214429 (2006).

[125] E. Snoeck, C. Gatel, L. M. Lacroix, T. Blon, S. Lachaize, J. Carrey, M. Respaud, and B. Chaudret, Nano Letters **8**, 4293 (2008).

[126] G. Gubbiotti, M. Madami, S. Tacchi, G. Carlotti, and T. Okuno, Journal of Applied Physics **99**, 08C701 (2006).

[127] D. I. Paul, Journal of Applied Physics **53**, 1649 (1982).

[128] M. Kläui, H. Ehrke, U. Ruediger, T. Kasama, R. E. Dunin-Borkowski, D. Backes, L. J. Heyderman, C. A. F. Vaz, J. A. C. Bland, G. Faini, E. Cambril, and W. Wernsdorfer, Applied Physics Letters **87**, 102509 (2005).

[129] A. Zhukov, M. Kiziroglou, A. Goncharov, R. Boardman, M. Ghanem, M. Abdelsalam, V. Novosad, G. Karapetrov, X. Li, H. Fangohr, C. de Groot, P. Bartlett, and P. de Groot, IEEE Transactions on Magnetics **41**, 3598 (2005).

[130] C. T. Yu, H. Jiang, L. Shen, P. J. Flanders, and G. J. Mankey, Journal of Applied Physics **87**, 6322 (2000).

[131] Z. L. Xiao, C. Y. Han, U. Welp, H. H. Wang, V. K. Vlasko-Vlasov, W. K. Kwok, D. J. Miller, J. M. Hiller, R. E. Cook, G. A. Willing, and G. W. Crabtree, Applied Physics Letters **81**, 2869 (2002).

[132] M. Jaafar, D. Navas, A. Asenjo, M. Vazquez, M. Hernandez-Velez, and J. M. Garcia-Martin, Journal of Applied Physics **101**, 09F513 (2007).

[133] C. Jiang, W. Wei, Q. Liu, D. Guo, and D. Xue, Applied Surface Science **258**, 3723 (2012).

[134] P. Vavassori, G. Gubbiotti, G. Zangari, C. T. Yu, H. Yin, H. Jiang, and G. J. Mankey, Journal of Applied Physics **91**, 7992 (2002).

[135] Q. Liu, C. Jiang, X. Fan, J. Wang, and D. Xue, Chinese Physics . . . **23**, 1592 (2006).

[136] H. Callen and E. Callen, Journal of Physics and Chemistry of Solids **27**, 1271 (1966).

[137] B. Van Waeyenberge, A. Puzic, H. Stoll, K. W. Chou, T. Tyliszczak, R. Hertel, M. Fähnle, H. Brückl, K. Rott, G. Reiss, I. Neudecker, D. Weiss, C. H. Back, and G. Schütz, Nature **444**, 461 (2006).

[138] M. Kammerer, M. Weigand, M. Curcic, M. Noske, M. Sproll, A. Vansteenkiste, B. Van Waeyenberge, H. Stoll, G. Woltersdorf, C. H. Back, and G. Schuetz, Nature communications **2**, 279 (2011).

[139] F. Haering, U. Wiedwald, T. Häberle, L. Han, A. Plettl, B. Koslowski, and P. Ziemann, Nanotechnology **24**, 055305 (2013).

[140] W. R. Branford, S. Ladak, D. E. Read, K. Zeissler, and L. F. Cohen, Science **335**, 1597 (2012).

[141] A. Farhan, P. M. Derlet, A. Kleibert, A. Balan, R. V. Chopdekar, M. Wyss, J. Perron, A. Scholl, F. Nolting, and L. J. Heyderman, Physical Review Letters **111**, 057204 (2013).

[142] L. Neél, CR Acad. Sci. Paris **241**, 533 (1955).

[143] M. Rabe, J. Pommer, K. Samm, B. Özyilmaz, C. König, M. Fraune, U. Rüdiger, G. Güntherodt, S. Senz, and D. Hesse, J. Phys.: Condens. Matter **7** (2002).

[144] Y. Rheem, B.-Y. Yoo, W. P. Beyermann, and N. V. Myung, Nanotechnology **18**, 015202 (2007).

[145] C. Wang, A. Adeyeye, N. Singh, Y. Huang, and Y. Wu, Physical Review B **72**, 1 (2005).

[146] T.-J. Meng, J.-B. Laloe, S. N. Holmes, A. Husmann, and G. A. C. Jones, Journal of Applied Physics **106**, 033901 (2009).

[147] P. Tiberto, L. Boarino, F. Celegato, G. Barrera, N. De Leo, M. Coisson, F. Vinai, and P. Allia, Applied Surface Science **259**, 44 (2012).

[148] G. Dumpich, T. Krome, and B. Hausmanns, Journal of Magnetism and Magnetic Materials **248**, 241 (2002).

[149] "http://idc2d.sourceforge.net/," (2013).

[150] J. Kim, S.-G. Cho, Y.-H. Choa, G. J. Shin, and J. Kim, Thin Solid Films **520**, 3013 (2012).

[151] C.-C. Ho, T.-W. Hsieh, H.-H. Kung, W.-T. Juan, K.-H. Lin, and W.-L. Lee, Applied Physics Letters **96**, 122504 (2010).

[152] F. Haering, U. Wiedwald, S. Nothelfer, B. Koslowski, P. Ziemann, L. Lechner, A. Wallucks, K. Lebecki, U. Nowak, J. Gräfe, E. Goering, and G. Schütz, Nanotechnology **24**, 465709 (2013).

[153] K. M. Lebecki, D. Hinzke, U. Nowak, and O. Chubykalo-Fesenko, Physical Review B **86**, 094409 (2012).

[154] A. Wallucks, *Computer Simulation on the magnetoresistance in antidot lattices*, Bachelor thesis, University of Konstanz (2012).

[155] G. Ctistis, E. Papaioannou, P. Patoka, J. Gutek, P. Fumagalli, and M. Giersig, Nano Letters **9**, 1 (2009).

[156] F. Béron, K. R. Pirota, V. Vega, V. M. Prida, A. Fernández, B. Hernando, and M. Knobel, New Journal of Physics **13**, 013035 (2011).

[157] E. Gu, J. a. C. Bland, C. Daboo, M. Gester, L. M. Brown, R. Ploessl, and J. N. Chapman, Journal of Applied Physics **76**, 6440 (1994).

[158] E. Gu, J. Bland, C. Daboo, and M. Gester, Physical review B **51**, 3596 (1995).

[159] S. Ladak, D. E. Read, G. K. Perkins, L. F. Cohen, and W. R. Branford, Nature Physics **6**, 359 (2010).

Acknowledgment

Over the past years, many people contributed to the success of this work. Here, I would like to express my gratitude towards them:

Prof. Dr. Paul Ziemann, who accepted me as a Ph.D. student in the Institute for Solid State Physics. Apart from his excellent scientific guidance, I am grateful for the trust that was put into me.

Prof. Dr. Ulrich Herr, for his kind acceptance to be my second referee.

PD Dr. Ulf Wiedwald - without his excellent advise this work would not have been possible. I learned a lot from him, even beyond the scientific aspects. Last but not least, I am very grateful for his proofreading of the thesis!

Balati Kuerbanjiang, who generously offered me a part of his beam time at BESSY II. I am also grateful for the very pleasant collaboration during the years.

Dr. Moritz Trautvetter and Dr. Luyang Han - for their invaluable support in the initial stage of this work. I learned a lot from you!

Apl. Prof. Dr. Berndt Koslowski, Steffen Nothelfer, Thomas Häberle, Hartmut Straub - For the continuous and wonderful work on the MFM.

Dr. Alfred Plettl, Dr. Stefan Wiedemann, Fabian Enderle und Pavan Muralidhar - without their experience on the field of colloidal lithography, my samples would never have reached such a quality. For his support in the sample preparation during the final months of this work, my thanks goes to Manuel Hartmann.

Matthias Stocker and Burcin Özdemir, who kindly volunteered to proofread this work.

Prof. Dr. Gisela Schütz, PD Dr. Eberhard Goering, Joachim Gräfe from Max Planck Institute for Intelligent Systems, as well as Prof. Dr. Ulrich Nowak, Dr. Kristof Lebecki and Andreas Wallucks from University of Konstanz - For the successful collaboration in the course of the project D6 of the Kompetenznetz Funktionelle Nanostrukturen (KFN).

Dr. Lorenz Lechner - For his patience during the search for the “perfect” crystallite and the subsequent FIB-structuring of my samples.

Hans-Dieter Kerpers, Volker Besserer and Sven Pernes for the quick response on all kinds of technical challenges.

Gabriele Dinger and Tanja Hager, who were of great help in all administrative questions.

My thanks goes to all employees of the Institute for Solid State Physics for the pleasant working atmosphere and also for the wonderful moments we shared outside of the University.

The financial support of the Baden-Württemberg-Stiftung, provided in the course of the Project D6 of the Kompetenznetz Funktionelle Nanostrukturen (KFN), is gratefully acknowledged.

A special thanks goes to my family, my girlfriend and my friends, who always believed in me. Especially during the final stage of this thesis their support was invaluable.

List of Publications and Conference Contributions

Publications

1. Ulf Wiedwald, Felix Haering, Stefan Nau, Carsten Schulze, Herbert Schletter, Denys Makarov, Alfred Plettl, Karsten Kuepper, Manfred Albrecht, Johannes Boneberg, Paul Ziemann. “Tuning the properties of magnetic thin films by interaction with periodic nanostructures.” *Beilstein Journal of Nanotechnology* **3**, 831 (2012).

2. Thomas Häberle, Felix Haering, Holger Peifer, Luyang Han, Balati Kuerbanjiang, Ulf Wiedwald, Ulrich Herr and Berndt Koslowski. “Towards quantitative magnetic force microscopy: theory and experiment.” *New Journal of Physics* **14**, 043044 (2012).

3. Felix Haering, Ulf Wiedwald, Thomas Häberle, Luyang Han, Alfred Plettl, Berndt Koslowski and Paul Ziemann. “Geometry-induced spin-ice structures prepared by self-organization on the nanoscale.” *Nanotechnology* **24**, 055305 (2013).

4. Balati Kuerbanjiang, Ulf Wiedwald, Felix Haering, Johannes Biskupek, Ute Kaiser, Paul Ziemann, Ulrich Herr. “Exchange bias of Ni nanoparticles embedded in an antiferromagnetic IrMn matrix.” *Nanotechnology* **24**, 455702 (2013).

5. Felix Haering, Ulf Wiedwald, Steffen Nothelfer, Berndt Koslowski, Paul Ziemann, Lorenz Lechner, Andreas Wallucks, Kristof Lebecki, Ulrich Nowak, Joachim Gräfe, Eberhard Goering and Gisela Schütz. “Switching modes in easy and hard axis magnetic reversal in a self-assembled antidot array.” *Nanotechnology* **24**, 465709 (2013).

Conference Contributions

Talk: Felix Haering. “Preparation and Characterization of magnetic antidot arrays”. Status Workshop Kompetenznetz Funktionelle Nanostruktruren in Bad Herrenalb, 2010

Talk: Felix Haering, Ulf Wiedwald, Karsten Kuepper, Berndt Koslowski, Thomas Häberle, Hartmut Straub and Paul Ziemann. “Magnetic pinning in self-assembled sub-200nm antidot arrays” DPG-Frühjahrstagung der Sektion Kondensierte Materie (SKM) in Dresden, 2011

Talk: Felix Haering, Ulf Wiedwald, Lorenz Lechner, Paul Ziemann. “Anisotropic magnetoresistance in self-assembeld antidot arrays” DPG-Frühjahrstagung der Sektion Kondensierte Materie (SKM) in Berlin, 2012

Poster: Steffen Nothelfer, Felix Haering, Ulf Wiedwald, Berndt Koslowski, Paul Ziemann. “Studying the magnetization reversal of a permalloy antidot array by magnetic force microscopy” DPG-Frühjahrstagnung der Sektion Kondensierte Materie in Regensburg, 2013

Poster: Felix Haering, Ulf Wiedwald, Paul Ziemann, Joachim Gräfe, Eberhard Goering, Gisela Schütz, Andreas Wallucks, Kristof Lebecki, Ulrich Nowak. “Magnetization reversal of self-assembled antidot arrays on the nanoscale” Trends in Nanoscience, Kloster Irsee, 2013

Poster: Balati Kuerbanjiang, Ulf Wiedwald, Felix Haering, Johannes Biskupek, Ute Kaiser, Paul Ziemann, Ulrich Herr “Enhanced anisotropy of Ni nanoparticles embedded in IrMn matrices” DPG-Frühjahrstagnung der Sektion Kondensierte Materie in Regensburg, 2013

Poster: Joachim Graefe, Felix Haering, Ulf Wiedwald, Paul Ziemann, Ulrich Nowak, Gisela Schuetz, Eberhard Goering “Investigation of Domain Pattern and Magnetisation Reversal Process in Hexagonal Nano-Scaled Antidot Lattices” DPG-Frühjahrstagnung der Sektion Kondensierte Materie in Regensburg, 2013

Lebenslauf

Persönliche Angaben

Name:	Felix Häring
Geburtstag, -ort:	23.10.1983 in Rottweil am Neckar
Anschrift:	Fichtestraße 9 89231 Neu-Ulm

Schulbildung

07/90 - 07/92	Eichendorffschule Rottweil
07/92 - 07/94	Römerschule Rottweil
08/94 - 07/03	Leibnizgymnasium Rottweil

Zivildienst

09/03 - 07/04	Zivildienst in der EDV-Abteilung des Vinzenz von Paul Hospitals, Rottweil

Akademischer Werdegang

10/04 - 10/09	Studium der Wirtschaftsphysik an der Universität Ulm Abschluss: Diplom
10/09 - 03/10	Wissenschaftliche Hilfskraft am Institut für Festkörperphysik an der Universität Ulm.
04/10 - 12/13	Wissenschaftlicher Angesteller am Institut für Festkörperphysik an der Universität Ulm. Schwerpunkt der Arbeit: Nanostrukturierte magnetische Dünnschichtsysteme

Ulm, April 7, 2014

Erklärung

Ich erkläre, dass ich die Arbeit selbständig verfasst und keine anderen als die angegebenen Quellen und Hilfsmittel verwendet habe. Wörtlich oder inhaltlich aus Quellen übernommenene Stellen habe ich als solche kenntlich gemacht. Die Satzung der Universität Ulm zur Sicherung guter wissenschaftlicher Praxis in der Fassung vom 16.10.2009 habe ich beachtet.

Ich versichere außerdem, dass ich die beigefügte Dissertation nur in diesem und keinem anderen Promotionsverfahren eingereicht habe und dass diesem Promotionsverfahren keine endgültig gescheiterten Promotionsverfahren vorausgegangen sind.

Ulm, den .....

Felix Häring